



# Displacive characteristics of $\beta$ to $\alpha$ phase transformation and its impact on hot deformation behavior in Ti-7333 metastable $\beta$ titanium alloy

Ke Hua

## ► To cite this version:

Ke Hua. Displacive characteristics of  $\beta$  to  $\alpha$  phase transformation and its impact on hot deformation behavior in Ti-7333 metastable  $\beta$  titanium alloy. Materials. Université de Lorraine; Northwestern Polytechnical University (Chine), 2019. English. NNT : 2019LORR0213 . tel-02529689

**HAL Id: tel-02529689**

**<https://hal.univ-lorraine.fr/tel-02529689>**

Submitted on 2 Apr 2020

**HAL** is a multi-disciplinary open access archive for the deposit and dissemination of scientific research documents, whether they are published or not. The documents may come from teaching and research institutions in France or abroad, or from public or private research centers.

L'archive ouverte pluridisciplinaire **HAL**, est destinée au dépôt et à la diffusion de documents scientifiques de niveau recherche, publiés ou non, émanant des établissements d'enseignement et de recherche français ou étrangers, des laboratoires publics ou privés.



## AVERTISSEMENT

Ce document est le fruit d'un long travail approuvé par le jury de soutenance et mis à disposition de l'ensemble de la communauté universitaire élargie.

Il est soumis à la propriété intellectuelle de l'auteur. Ceci implique une obligation de citation et de référencement lors de l'utilisation de ce document.

D'autre part, toute contrefaçon, plagiat, reproduction illicite encourt une poursuite pénale.

Contact : [ddoc-theses-contact@univ-lorraine.fr](mailto:ddoc-theses-contact@univ-lorraine.fr)

## LIENS

Code de la Propriété Intellectuelle. articles L 122. 4

Code de la Propriété Intellectuelle. articles L 335.2- L 335.10

[http://www.cfcopies.com/V2/leg/leg\\_droi.php](http://www.cfcopies.com/V2/leg/leg_droi.php)

<http://www.culture.gouv.fr/culture/infos-pratiques/droits/protection.htm>



UNIVERSITÉ  
DE LORRAINE



西北工业大学  
NORTHWESTERN POLYTECHNICAL UNIVERSITY

UNIVERSITÉ DE LORRAINE

NORTHWESTERN POLYTECHNICAL UNIVERSITY

## DISSERTATION

To be presented at

Université de Lorraine and Northwestern Polytechnical University

Ke HUA 花珂

To obtain the doctor's degree of

University of Lorraine and Northwestern Polytechnical University

SPECIAL FIELD: Engineering Sciences

OPTION: Materials Science

*Displacive characteristics of  $\beta$  to  $\alpha$  phase transformation and its impact on hot deformation behavior in Ti-7333 metastable  $\beta$  titanium alloy*

Defended on June 15<sup>th</sup>, 2019 in front of the jury:

Anthony ROLLETT	Professor	Carnegie Mellon University, USA	Reviewer & Jury member
Rui YANG	Professor	Institute of Metal Research, China	Reviewer & Jury member
Benoit APPOLAIRE	Professor	Université de Lorraine, France	Jury member
Yongqing ZHAO	Professor	Northwest Institute For Non-ferrous Metal Research, China	Jury member
Yudong ZHANG	Doctor HDR	Université de Lorraine, France	Supervisor
Jinshan LI	Professor	Northwestern Polytechnical University, China	Supervisor
Weimin GAN	Doctor HDR	Helmholtz-Center Geesthacht, Germany	Co-Supervisor
Hongchao KOU	Professor	Northwestern Polytechnical University, China	Co-Supervisor
Claude ESLING	Professor	Université de Lorraine, France	Invited

Laboratoire d'Étude des Microstructures et de Mécanique des Matériaux, LEM3  
7 rue Félix Savart, 57070 Metz, France



## Abstract

In the present work, a thorough investigation has been conducted on the Ti-7333 alloy in terms of the  $\alpha$  to  $\beta$  phase transformation, the variant selection and the correlation between the microstructure evolution and the hot deformation behavior.

It was revealed that the intragranular  $\alpha$  plates precipitated during the heat treatment obey the Burgers Orientation Relationship (BOR) with the  $\beta$  matrix. The structure transformation is realized by a contraction in the  $\langle 1\bar{1}\bar{2} \rangle_\beta$ , an elongation in the  $\langle \bar{1}1\bar{1} \rangle_\beta$  and  $\langle 110 \rangle_\beta$ , and a shear on the  $\{1\bar{1}\bar{2}\}_\beta \langle \bar{1}1\bar{1} \rangle_\beta$  slip system. Locally three variants interrelated by a  $60^\circ/\langle 11\bar{2}0 \rangle_\alpha$  rotation form a triangular pattern. Each  $\alpha$  precipitate is composed of two kinds of nano-sized  $\alpha$  domains. One is situated on the broad face of the major  $\alpha$  precipitate (named interface  $\alpha$ ), and the other goes through the major  $\alpha$  (termed penetrating  $\alpha$ ). The interface  $\alpha$  obeys the BOR with the  $\beta$  matrix and is related with the major  $\alpha$  by a  $60^\circ/\langle 11\bar{2}0 \rangle_\alpha$  rotation. The nucleation of such  $\alpha$  is induced by the large shear strain generated by the formation of the major  $\alpha$ . The penetrating  $\alpha$  does not obey the BOR with the  $\beta$  matrix but is related with the major  $\alpha$  by a  $60^\circ$  rotation around another  $\langle 11\bar{2}0 \rangle_\alpha$ . The nucleation of such  $\alpha$  is induced by the largest normal strain generated by the formation of the main  $\alpha$  plate.

The selection of the  $\alpha$  variants during hot deformation at  $700^\circ\text{C}$  happens with dependence on the local crystal perfection of the  $\beta$  grains. In the slightly deformed  $\beta$  grains, 2 BOR variants forming ‘cross-shaped’ clusters and interrelated by a  $90^\circ$  rotation around the  $\langle 1\ 1.38\ \bar{2}.38\ 0 \rangle_\alpha$  axis are selected and form in large quantities. The selected variants make maximum contribution to the macroscopic deformation and receive the maximum resolved shear stress from the external load resolved on their  $\{1\bar{1}\bar{2}\}_\beta \langle \bar{1}1\bar{1} \rangle_\beta$  systems for transformation. In the heavily deformed  $\beta$  grains occupied mainly by dislocation slip, 2 to 4 BOR variants are selected in smaller numbers. The selection criterion is still obeyed but with restriction from the local deformation. The  $\alpha$  variant selection also occurs in the  $600^\circ\text{C}$  compression but under the only request for the maximum strain contribution to the macroscopic deformation.

The deformation behavior during  $700^\circ\text{C}$  compression presents three characteristic stress-strain stages: a linear stage (Stage I), a discontinuous yielding (Stage II) and a

steady-state (Stage III). At the end of Stage I, more than 90% of the  $\beta$  boundaries are occupied by grain boundaries  $\alpha$  ( $\alpha_{GB}$ ). The onset of the plastic deformation happens at the late Stage I when the stress deviates from the Young's modulus. This behavior results from dislocation slip near the  $\beta$  grain boundary regions. The discontinuous yielding of Stage II originated from the fragmentation of the  $\alpha_{GB}$  and the intensive formation of mobile dislocations near the  $\beta$  grain boundary areas. The steady-state of Stage III arises from two orientation dependent deformation modes of the  $\beta$  grains. For those in favorable activation orientation for their  $\{110\}_{\beta} \langle \bar{1}\bar{1}1 \rangle_{\beta}$  systems with respect to the external compressive load, the deformation is realized by the dislocation slip and by the formation of slip bands; whereas for those with their  $\{1\bar{1}2\}_{\beta} \langle \bar{1}1\bar{1} \rangle_{\beta}$  systems - the system for  $\beta$  to  $\alpha$  transformation - in favorable orientations, the deformation is achieved by intensive formation of intragranular  $\alpha$  precipitates. The deformation at 600°C compression presents the same stress-strain characteristics for Stage I and II. After these two stages, the deformation experiences first work hardening resulting from massive  $\beta$  to  $\alpha$  transformation, and then work softening from the formation of the spheroidized  $\alpha$  and  $\beta$  bands.

This work provides comprehensive information on the displacive feature of the  $\beta$  to  $\alpha$  transformation, the underlying mechanisms of  $\alpha$  variant selection under thermal and thermomechanical processing and the transformation related hot deformation mechanisms of metastable  $\beta$  titanium alloys.

**Key words:** Titanium alloy; Phase transformation; Transformation strain; Strain accommodation; Variant selection; thermomechanical processing.

## Résumé

Dans le présent travail, une étude approfondie a été menée sur l'alliage Ti-7333 en termes de transformation de phase  $\alpha$  en  $\beta$ , de sélection de variantes et de corrélation entre l'évolution de la microstructure et le comportement à la déformation à chaud.

Il a été montré que les plaques  $\alpha$  intragranulaires précipitées pendant le traitement thermique obéissent à la relation d'orientation de Burgers (BOR) avec la matrice  $\beta$ . La transformation de la structure est réalisée par une contraction dans  $\langle 1\bar{1}\bar{2} \rangle_\beta$ , un allongement dans  $\langle \bar{1}1\bar{1} \rangle_\beta$  et  $\langle 110 \rangle_\beta$ , et un cisaillement sur le système de glissement  $\{1\bar{1}\bar{2}\}_\beta / \langle \bar{1}1\bar{1} \rangle_\beta$ . Localement, trois variantes liées entre elles par une rotation de  $60^\circ / \langle 11\bar{2}0 \rangle_\alpha$  forment un motif triangulaire. Chaque précipité  $\alpha$  est composé de deux types de domaines  $\alpha$  de taille nanométrique. L'un est situé sur la face large du précipité  $\alpha$  majeur (interface  $\alpha$ ), l'autre traverse le  $\alpha$  majeur ( $\alpha$  pénétrant). L'interface  $\alpha$  obéit au BOR avec la matrice  $\beta$  et est reliée à la majeure  $\alpha$  par une rotation de  $60^\circ / \langle 11\bar{2}0 \rangle_\alpha$ . La nucléation de cet  $\alpha$  est induite par la contrainte importante de cisaillement générée par la formation du  $\alpha$  majeur. Le  $\alpha$  pénétrant n'obéit pas au BOR avec la matrice  $\beta$  mais est relié au  $\alpha$  principal par une rotation de  $60^\circ$  autour d'un autre  $\langle 11\bar{2}0 \rangle_\alpha$ . La nucléation de cet  $\alpha$  est induite par la plus grande contrainte normale générée par la formation de la plaque  $\alpha$  principale.

La sélection des variantes  $\alpha$  lors de la déformation à chaud à  $700^\circ\text{C}$  s'effectue en fonction de la perfection cristalline locale des grains  $\beta$ . Dans les grains  $\beta$  légèrement déformés, 2 variantes de BOR liées entre elles par  $90^\circ / \langle 1\ 1.38\ \bar{2}.38\ 0 \rangle_\alpha$  rotation sont sélectionnées en grands nombres. Les variantes sélectionnées apportent une contribution maximale à la déformation macroscopique et subissent la contrainte de cisaillement résolue maximale de la charge externe résolue sur leurs systèmes de transformation  $\{1\bar{1}\bar{2}\}_\beta / \langle \bar{1}1\bar{1} \rangle_\beta$ . Dans les grains  $\beta$  fortement déformés occupés principalement par des bandes de glissement, 2 à 4 variantes de BOR sont sélectionnées. Le critère de sélection est toujours respecté mais avec une restriction de la déformation locale. La sélection de la variante  $\alpha$  se produit également lors de la compression à  $600^\circ\text{C}$  mais sous la seule condition de la contribution maximale de la déformation à la déformation macroscopique.

Le comportement en déformation lors de la compression à 700 °C présente trois stades contraintes-déformations caractéristiques: un stade linéaire (stade I), un stade d'écoulement discontinu (stade II) et un stade stable (stade III). À la fin du stade I, plus de 90% des joints de grains  $\beta$  sont occupés par des joints de grains  $\alpha$  ( $\alpha_{GB}$ ). Le rendement discontinu du stade II provient de la fragmentation de  $\alpha_{GB}$  et de la formation intensive de dislocations mobiles près des joints de grains  $\beta$ . L'état d'équilibre du stade III résulte de deux modes de déformation. Pour ceux dont l'orientation d'activation est favorable pour leurs systèmes  $\{110\}_{\beta} <1\bar{1}1>_{\beta}$  par rapport à la charge de compression, la déformation est réalisée par le glissement de dislocation et par la formation de bandes de glissement; alors que pour ceux avec leur  $\{1\bar{1}2\}_{\beta} <\bar{1}1\bar{1}>_{\beta}$  systèmes - le système de transformation de  $\beta$  à  $\alpha$  - dans des orientations favorables, la déformation est obtenue par formation intensive de précipités  $\alpha$  intragranulaires. La déformation à une compression de 600 °C présente les mêmes caractéristiques de contrainte-déformation pour les stades I et II. Après ces deux étapes, la déformation subit d'abord un durcissement résultant de la transformation massive de  $\beta$  en  $\alpha$ , puis un adoucissement résultant de la formation des bandes  $\alpha$  et  $\beta$  sphéroïdisées.

Ce travail fournit des informations détaillées sur la caractéristique de déplacement de la transformation  $\beta$  à  $\alpha$ , les mécanismes sous-jacents de la sélection des variantes  $\alpha$  sous traitement thermique et thermomécanique et les mécanismes de déformation à chaud liés à la transformation des alliages de titane  $\beta$  métastable.

**Mots-clés:** Alliage de titane; Transformation de phase; Déformation de transformation; Accommodation de déformation; Sélection de variantes; traitement thermomécanique



## Content

<b>Abstract.....</b>	<b>I</b>
<b>Résumé .....</b>	<b>III</b>
<b>Chapter 1 Literature review.....</b>	<b>1</b>
1.1 General introduction.....	1
1.2 Crystal structure and classification of titanium alloys .....	2
1.2.1 Crystal structure of pure titanium.....	2
1.2.2 Classification of titanium alloy .....	3
1.3 Phase transformation under thermal or thermomechanical processing in metastable $\beta$ titanium alloys .....	4
1.3.1 $\beta$ to $\alpha$ phase transformation .....	4
1.3.2 Variant selection during $\beta$ to $\alpha$ phase transformation.....	7
1.4 Hot deformation behavior of metastable $\beta$ titanium alloy.....	10
1.4.1 Hot deformation in single $\beta$ phase region .....	10
1.4.2 Hot deformation in $\alpha+\beta$ phase region .....	11
1.4 Organization of the thesis.....	15
<b>Chapter 2 Materials, experimental details and basic crystallographic calculations.....</b>	<b>17</b>
2.1 Materials preparation.....	17
2.2 Experimental details .....	17
2.2.1 Thermal mechanical processing .....	17
2.2.2 Determination of the lattice constants .....	18
2.2.3 Isothermal compression under <i>in-situ</i> neutron diffraction .....	19
2.2.4 Microstructural and crystallographic characterization .....	20
2.3 Basic crystallographic calculation.....	21
2.3.1 Coordinate system setting .....	21
2.3.2 Coordinate transformation.....	22
2.3.3 Stereographic projection .....	25
2.3.4 Misorientation .....	26

2.3.5 Trace analysis method .....	28
2.3.6 Deformation gradient tensor.....	30
<b>Chapter 3 Microstructure evolution and phase transformation under heat treatment ..</b>	<b>33</b>
3.1 Introduction .....	33
3.2 Experimental .....	33
3.3 Microstructure of the initial $\beta$ phase and lattice constant information.....	34
3.4 Phase transformation under heat treatment .....	35
3.4.1 Microstructure characteristics of $\alpha$ precipitates .....	35
3.4.2 Sub-structures of intragranular $\alpha$ precipitates .....	38
3.5 Formation mechanisms of sub-structures of intragranular $\alpha$ precipitates .....	45
3.5.1 Phase transformation lattice strain characters .....	45
3.5.2 Formation mechanism of interface $\alpha$ and local variant selection of major $\alpha$ ....	47
3.5.3 Formation mechanism of non BOR $\alpha$ domains .....	50
3.6 Summary .....	52
<b>Chapter 4 Phase transformation and <math>\alpha</math> variant selection mechanism during isothermal compression.....</b>	<b>55</b>
4.1 Introduction .....	55
4.2 Experimental .....	55
4.3 Microstructure of the initial $\beta$ phase .....	56
4.4 Phase transformation and $\alpha$ variant selection during 700 °C compression .....	56
4.4.1 Phase transformation and $\alpha$ variant selection in stress-free state.....	56
4.4.2 Phase transformation and $\alpha$ variant selection under 700 °C isothermal compression.....	57
4.4.3 Variant selection mechanisms .....	62
4.5 Phase transformation and $\alpha$ variant selection during 600°C compression .....	72
4.5.1 Phase transformation and $\alpha$ variant selection during heat treatment.....	72
4.5.2 Phase transformation and $\alpha$ variant selection during 600 °C isothermal compression.....	73
4.6 Summary .....	77
<b>Chapter 5 Correlation between microstructure evolution and deformation behavior</b>	

<b>during isothermal compression.....</b>	<b>79</b>
5.1 Introduction .....	79
5.2 Experimental .....	79
5.3 Microstructure of the initial $\beta$ phase .....	80
5.4 Correlation between microstructure evolution and hot deformation behavior during 700°C compression.....	81
5.4.1 Mechanical behavior .....	81
5.4.2 Correlation between microstructure and deformation behavior.....	82
5.5 Correlation between microstructure evolution and hot deformation behavior during 600°C compression.....	97
5.5.1 Mechanical behavior .....	97
5.5.2 Correlation between microstructure and deformation behavior.....	98
5.6 Summary .....	102
<b>Chapter 6 Conclusions and Perspectives .....</b>	<b>105</b>
6.1 Conclusions .....	105
6.2 Perspectives.....	108
<b>Appendix A .....</b>	<b>111</b>
Specification of 12 BOR variants.....	111
<b>Appendix B.....</b>	<b>113</b>
Experimental setup of the <i>in-situ</i> neutron diffraction measurement to detect the intragranular $\alpha$ precipitation.....	113
<b>References .....</b>	<b>117</b>
<b>Publication list .....</b>	<b>131</b>
I: Publications in international journals .....	131
II: Contributions to International Conferences.....	131
<b>Acknowledgements.....</b>	<b>133</b>



## Chapter 1 Literature review

### 1.1 General introduction

Titanium and titanium alloys are of particular interest for aerospace and biomedical applications over the past 50 years. The mechanical properties of titanium alloys, such as ductility, strength, creep resistance, crack propagation resistance and fracture toughness, depend, to a large extent, on the microstructure that is formed during either thermal or thermomechanical treatment. According to the application, a specific property or combination of properties can be obtained through microstructure tuning. Microstructure evolution and control of titanium alloys rely heavily on the allotropic transformation from a body-centered cubic (BCC) crystal structure (denoted as  $\beta$  phase) at high temperatures to a hexagonal close-packed (HCP) crystal structure (referred to as  $\alpha$  phase) found at low temperatures. Especially, metastable  $\beta$  titanium alloys show a greater sensitivity to processing parameters. Besides, variant selection of the  $\alpha$  phase during its precipitation from the  $\beta$  matrix plays a key role in determining transformation texture and the final mechanical properties of the titanium alloys [1-7]. Hence, it is necessary to thoroughly investigate the phase transformation and the hot deformation behavior of the metastable  $\beta$  titanium alloys during the thermal and thermomechanical processes.

In this chapter, the basic knowledge of titanium alloys, especially the phase transformation and hot deformation behavior during the thermomechanical processing, and the corresponding applications are overviewed. Four parts constitute this chapter, i.e., **a)** the crystal structure and classification of titanium alloys; **b)** the phase transformation in titanium alloy during thermal and thermomechanical processes; **c)** the hot deformation behavior of the metastable  $\beta$  titanium alloy and **d)** the motivation and content of the present work.

## 1.2 Crystal structure and classification of titanium alloys

### 1.2.1 Crystal structure of pure titanium

Pure titanium exhibits an allotropic phase transformation at 882°C, changing from a BCC crystal structure at higher temperatures to a HCP crystal structure at lower temperatures. The former is termed as  $\beta$ -Ti and the latter  $\alpha$ -Ti. The body centered cubic unit cell of  $\beta$ -Ti and the hexagonal closed packed unit cell of  $\alpha$ -Ti are shown in Fig. 1.1. For the  $\beta$ -Ti, the lattice parameters  $a=b=c=3.32\text{ \AA}$ , and  $\alpha=\beta=\gamma=90^\circ$ . The space group is  $\text{Im}\bar{3}\text{m}$  (No. 229). The atom occupies the (0, 0, 0) position in the cell. Whereas for the  $\alpha$ -Ti, the lattice parameters  $a=b\neq c$ ,  $a=b=2.95\text{ \AA}$ ,  $c=4.68\text{ \AA}$ ,  $\alpha=\beta=90^\circ$ , and  $\gamma=120^\circ$ . The space group is  $\text{P6}_3/\text{mmc}$  (No. 194), and the atom occupies the (1/3, 2/3, 1/4) position in the cell [8, 9]. The resultant  $c/a$  ratio is 1.587, smaller than the ideal ratio of 1.633 for the HCP crystal structure.

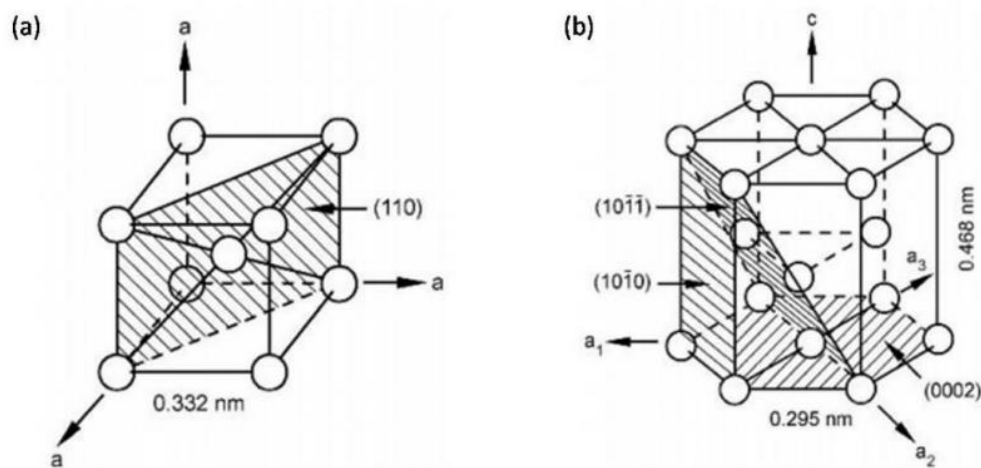


**Fig. 1.1** Two crystal structures of titanium: **(a)** body centered cubic (BCC) unit cell of  $\beta$ -Ti and **(b)** hexagonal closed packed (HCP) unit cell of  $\alpha$ -Ti [4].

## 1.2.2 Classification of titanium alloy

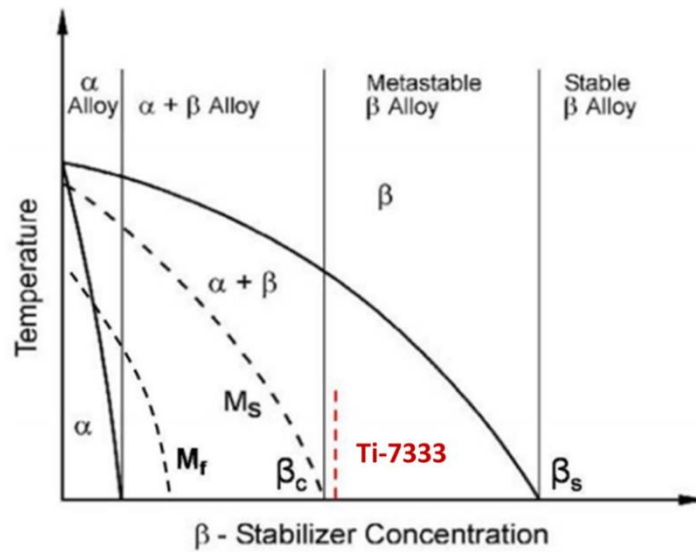


**Fig. 1.2** Pseudo-binary phase diagram of titanium alloys with the decomposition products of the  $\beta$  phase [4], where the location of Ti-7Mo-3Nb-3Cr-3Al (Ti-7333) is indicated.

As any pure metals, the strength of pure titanium is not sufficient for practical applications, element alloying has been an effective way for strengthening. The alloying elements to titanium are usually classified into  $\alpha$  or  $\beta$  stabilizing additions depending on whether they increase or decrease the  $\alpha/\beta$  transformation temperature of pure titanium. The substitutional element Al and the interstitial elements O, N, and C are all strong  $\alpha$  stabilizers and increase the  $\beta$  transus temperature ( $T_\beta$ ) with the increasing solute content. Whereas for the  $\beta$  stabilizing elements, the most frequently used elements are V, Mo, Cr and Nb. Thus, according to the phase constituents at room temperature, titanium alloys can be classified into four groups, i.e.,  $\alpha$  titanium alloys,  $\alpha+\beta$  titanium alloys, metastable  $\beta$  titanium alloys and stable  $\beta$  titanium alloys, as shown in Fig 1.2 [4]. The content of the  $\beta$  stabilizing elements in the metastable  $\beta$  titanium alloys and the stable  $\beta$  titanium alloys is more than that in the  $\alpha+\beta$  titanium alloys, leading to the stable existence of the  $\beta$  phase at room temperature. In fact, for the supersaturated  $\beta$  phase, there exist several phase transformations during thermal and thermomechanical processes in titanium alloys, for instance,  $\beta$  to  $\alpha$  phase transformation,  $\beta$  to  $\omega$  phase transformation, spinodal decomposition of  $\beta$  phase, and  $\beta$  to  $\alpha''$  (martensite) phase

transformation [10-13]. These phase transformations can be induced either by thermal treatment or thermomechanical treatment. Due to the high content of the  $\beta$  stabilizing elements,  $\beta$  to  $\alpha'$  phase transformation cannot happen in the metastable  $\beta$  titanium alloys or in the stable  $\beta$  titanium alloys, whereas it is a common phase transformation in the titanium alloys with high  $\alpha$  stabilizing elements. For the metastable  $\beta$  titanium alloys, the most important phase transformation is the  $\beta$  to  $\alpha$  phase transformation. When  $\beta$  phase transforms to  $\alpha$  phase through various thermomechanical processing, the metastable  $\beta$  titanium alloys can bring about high strength combined with reasonable reduction and toughness. Thus they are attractive materials for engineering applications. At present, the most used metastable  $\beta$  titanium alloys in aeronautical industries are the Ti-1023 (Ti-10V-2Fe-3Al) [14-16] and the Ti-5553 the (Ti-5Al-5Mo-5V-3Cr-0.5Fe) [17-21] alloy.

### **1.3 Phase transformation under thermal or thermomechanical processing in metastable $\beta$ titanium alloys**

#### **1.3.1 $\beta$ to $\alpha$ phase transformation**

It is known that the excellent mechanical properties of titanium alloys rely heavily on the phase transformation from  $\beta$  phase to  $\alpha$  phase. Hence, there are numerous investigations on the precipitation behaviors and mechanisms of formation of the  $\alpha$  phase. Generally, the transformed microstructures can be categorized into four types according to the morphology and characters of the  $\alpha$  precipitates. They are equiaxed microstructure, duplex microstructure, basket-weave microstructure and Widmanstatten microstructure. The different types of microstructures correspond to the various mechanical properties. For instance, the equiaxed microstructure exhibits good ductility and the Widmanstatten microstructure presents high fracture toughness. The basket-weave microstructure presents better fatigue properties and ductility than that of the Widmanstatten microstructure. The duplex microstructures possess a reasonable combination of the mechanical properties. Based on the solid state transformation theory in titanium alloy, the  $\beta$  to  $\alpha$  phase transformation can be designed through various thermomechanical processes.

Fig. 1.3 shows the typical microstructures of the metastable  $\beta$  titanium alloys during heat



treatment. As shown in Fig. 1.3 (a), the  $\alpha$  phase firstly forms on the site of  $\beta$  grain boundary, named grain boundary  $\alpha$  ( $\alpha_{GB}$ ). Then the Widmanstätten  $\alpha$  phase forms from the grain boundary  $\alpha$  constituents [22, 23]. The Widmanstätten  $\alpha$  constituents are always oriented in parallel laths and evidenced that in general the orientations of the parallel laths are very close [24]. When the cooling rate is high, a large amount of  $\alpha$  precipitates are formed, contributing to the basket-weave microstructure [25], as displayed in Fig. 1.3 (b). Fig. 1.3 (c) shows an equiaxed microstructure in a metastable  $\beta$  titanium alloy. This microstructure is obtained in a forged bar through the solution treatment in the  $\alpha+\beta$  phase region. When the equiaxed microstructure is continued to be aged at lower temperatures in the  $\alpha+\beta$  phase region, the secondary  $\alpha$  phase is precipitated in the  $\beta$  matrix, as a result, the duplex microstructure is formed.

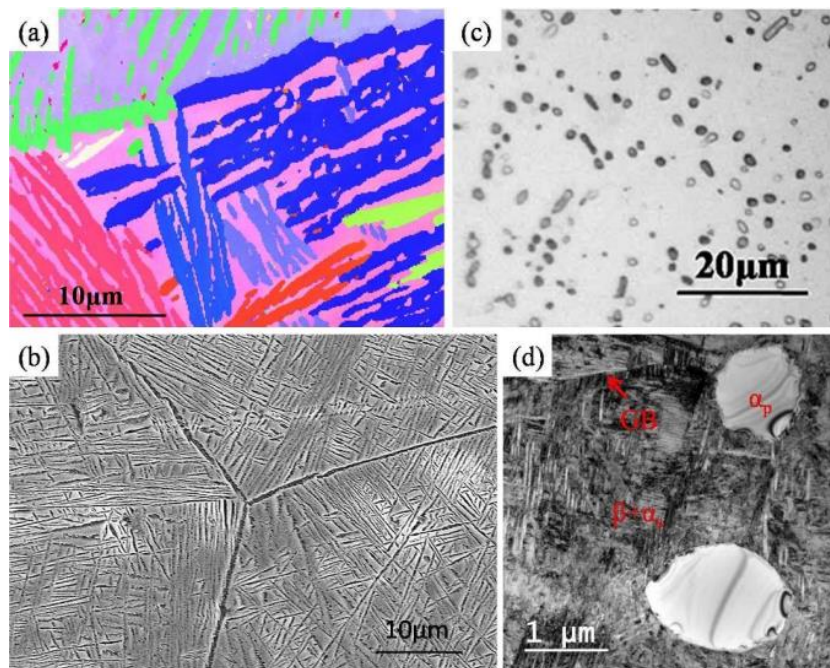


**Fig. 1.3** Micrographs of metastable  $\beta$  titanium alloy Ti-7333: **(a)** solution treated at 900°C for 30 min and cooled in furnace [24], **(b)** 880°C aged for 2 h and cooled in furnace at 2°C /min to 600°C and aged for 6 h [25], **(c)** solution treated at 800°C for 30min and water quenched [24], and **(d)** 820°C aged for 50min, cooled in air and aged at 520°C for 6h [26].

Generally, the  $\beta$  to  $\alpha$  phase transformation involves two processes: diffusion of alloying elements and structure transformation of Ti atoms. The former results in a composition

change of the product  $\alpha$  phase by depleting  $\beta$  stabilizing elements, such as Mo, Cr, Nb, and enriching  $\alpha$  stabilizing elements, such as Al, whereas the latter gives rise to the structure change from BCC to HCP [27-29]. Due to the displacive nature of the  $\beta$  to  $\alpha$  transformation, the transformation demonstrates specific crystallographic features, like the case of martensitic transformation. It is well known that  $\beta$  to  $\alpha$  phase transformation usually exhibits a specific orientation relationship (OR) between the two phases. In most cases, the Burgers Orientation relationship (BOR), i.e.,  $\{110\}_{\beta} \parallel (0001)_{\alpha}$  and  $\langle 1\bar{1}1 \rangle_{\beta} \parallel [11\bar{2}0]_{\alpha}$  [27] is obeyed.

Under the BOR, the single close-packed basal plane  $(0001)_{\alpha}$  in the HCP  $\alpha$  phase is parallel to one of the six close-packed planes  $\{110\}_{\beta}$  in the BCC  $\beta$  phase. In addition, one of the three close-packed  $[11\bar{2}0]_{\alpha}$  directions in the basal plane  $(0001)_{\alpha}$  is parallel to one of the two close-packed directions  $\langle 1\bar{1}1 \rangle_{\beta}$  lying within the specific close-packed plane  $\{110\}_{\beta}$  in the  $\beta$  phase. Thus, there are twelve ( $6 \times 2$ ) possible equivalent orientation variants of the  $\alpha$  precipitates allowed by the BOR. For the twelve orientation variants of the  $\alpha$  precipitates in one  $\beta$  grain, there are totally six distinct disorientations between each pair of two variants, as displayed in Table 1.1 [30]. The transformed  $\alpha$  phase is usually in plate shape with specific transformation habit plane  $\{3\ 3\ 4\}_{\beta}$  or  $\{11\ 11\ 13\}_{\beta}$  [31, 32].

**Table 1.1** Axis/angle pairs for all 6 possible  $\alpha/\alpha$  disorientations among the 12  $\alpha$  variants in a single  $\beta$  grain [30]

Type	Axis/angle paris	P <sub>random</sub> (%)
1	I (Identity)	/
2	60°/ $\langle 11\bar{2}0 \rangle$	18.2
3	60.832°/ $\langle \bar{1}.377\ \bar{1}\ 2.377\ 0.359 \rangle$	36.4
4	63.2618°/ $\langle \bar{1}0\ 5\ 5\ \bar{3} \rangle$	18.2
5	90°/ $\langle 1\ \bar{2}.38\ 1.38\ 0 \rangle$	18.2
6	10.5288°/ $\langle 0001 \rangle$	9.1

In addition, the displacive process of the  $\beta$  to  $\alpha$  transformation has been experimentally investigated in a Ti-5553 alloy [33]. As shown in Fig. 1.4, it was evidenced that at the very beginning of the transformation  $\alpha$  plates precipitate via a displacive process with a

composition very close to that of the  $\beta$  matrix. Then they grow through a coupled displacive-diffusional process with the partitioning of the alloying elements being transformation rate controlling [33]. The strain characters of the transformation and strain interaction between different variants have been analyzed theoretically [34-37]. It turns out that the transformation strain has strong influence on the formation of secondary  $\alpha$  particles and on local variant selection in relation to the need of minimizing the overall transformation strain energy.

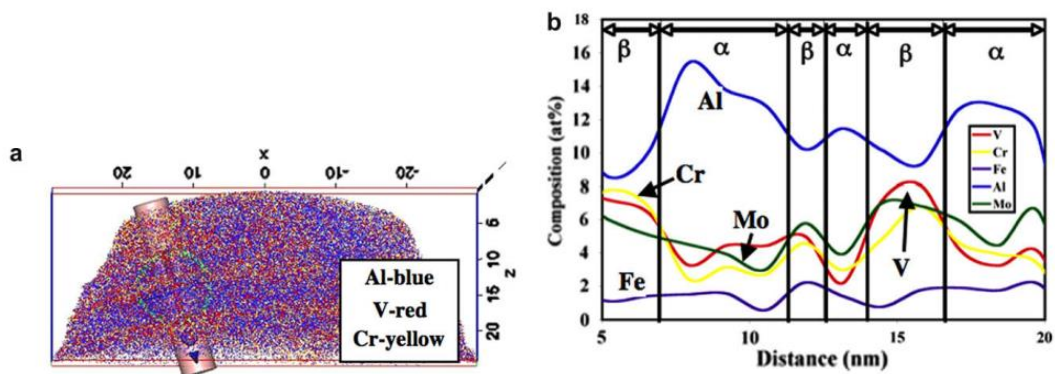


**Fig. 1.4 (a)** An example of a 3DAP reconstruction of Al (blue) V (red) and Cr (yellow) atoms in 400 °C/2 h annealed Ti-5553 sample, showing the  $\alpha$ - and  $\beta$ -rich regions. It also shows the 5nm cylinder along which the composition is measured. **(b)** The corresponding composition profiles for Al, V, Mo, Cr and Fe. The  $\alpha$  and the  $\beta$  regions are marked [33].

### 1.3.2 Variant selection during $\beta$ to $\alpha$ phase transformation

Accordingly, there are twelve possible equivalent orientation variants of  $\alpha$  precipitate allowed in one  $\beta$  grain. It is thus generally thought that all  $\alpha$  variants should appear with equal statistical probability. When only a small subset of the variants is formed preferentially within one parent crystal, variant selection occurs. Since variant selection plays an important role in determining the transformation texture and the final mechanical properties of the material [38-41] and is sensible to many external factors relating to the treatment processes [42], study on variant selection under different external conditions has been intensive.

There are many factors that could result in the variant selection during  $\alpha$  precipitation. The previous investigations have evidenced that  $\alpha$  variant selection happens in both thermal

and thermomechanical processes. The selection could be induced by both internal materials factors and external treatment factors.

For the internal factors, the crystallographic orientation of the  $\beta$  grains and the strain field of certain crystal defects (dislocations) could lead to the selection of grain boundary  $\alpha$  ( $\alpha_{GB}$ ) [43-50] and intragranular  $\alpha$  precipitates [51-60]. For example for  $\alpha_{GB}$ , if the adjacent  $\beta$  grains share a common  $\{110\}_\beta$  plane within an angular deviation of  $10^\circ$ , the variants with their  $\{0001\}_\alpha$  parallel to the common  $\{110\}_\beta$  will form preferentially [43, 46, 48], as shown in Fig. 1.5. For the intragranular  $\alpha$  precipitates, as displayed in Fig. 1.6, it was found that the  $\{1\bar{1}2\}_\beta <\bar{1}11>_\beta$  dislocations produced by cold deformation are in favor of the formation of the  $\alpha$  variants with their  $(1\bar{1}00)_\alpha$  plane parallel to the slip plane and the  $[11\bar{2}0]_\alpha$  parallel to the slip direction [51]. It was also revealed by theoretical simulations [34, 52] and experimental examinations [53-55] that the annihilation of the transformation lattice strain of certain variants by certain others leads to  $\alpha$  variant selection even during a stress-free transformation process. Such a selection mechanism well explains the formation of the specific triangular microstructure patterns formed by 3  $\alpha$  variants interrelated by a  $60^\circ$  rotation around their common  $<11\bar{2}0>_\alpha$  axis.

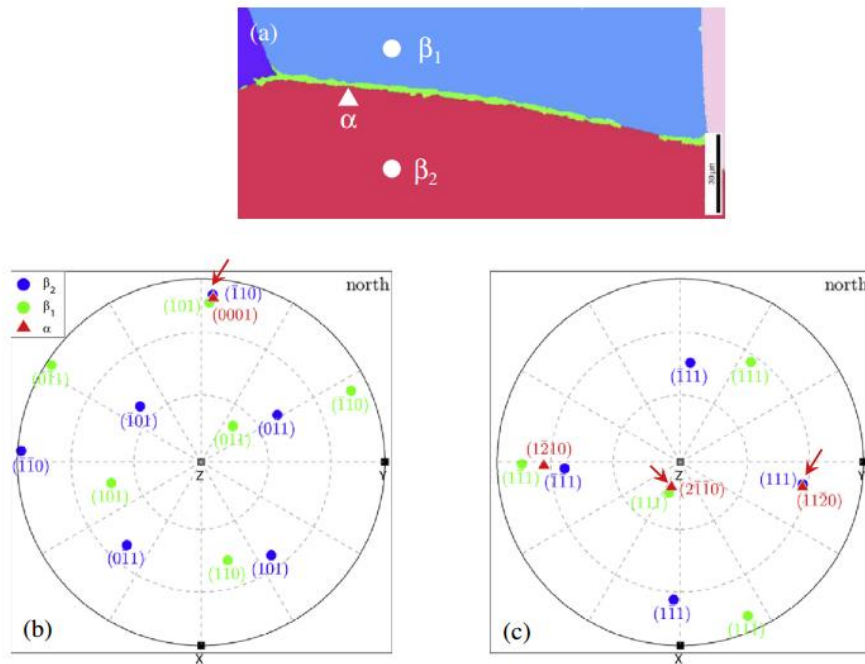


**Fig. 1.5** Experimental observations of a special grain boundary where  $\alpha_{GB}$  maintains BOR

with two adjacent  $\beta$  grains **(a)** OIM image of the Type II boundary; **(b)** superimposed pole figures of the  $\{110\}_{\beta}$  poles of the two  $\beta$  grains and the  $(0001)_{\alpha}$  pole of the  $\text{GB}\alpha$ ; **(c)** superimposed pole figures among the  $(111)_{\beta}$  poles of the two  $\beta$  grains and  $(11\bar{2}0)_{\alpha}$  pole of the  $\text{GB}\alpha$  [48].

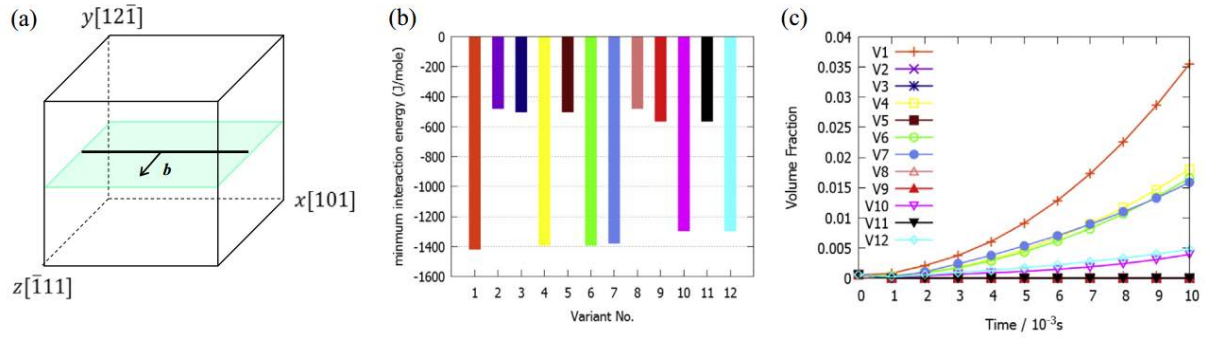


**Fig. 1.6** **(a)** Configuration of an edge dislocation in the slip plane  $(12\bar{1})_{\beta}$  as indicated by the shaded area with Burgers vector  $\mathbf{b}=[\bar{1}11]_{\beta}/2$ ; **(b)** the minimum interaction energy between the edge dislocation and each of the  $\alpha$  variants; **(c)** corresponding  $\alpha$  volume fractions as a function of time obtained from the phase-field simulations [51].

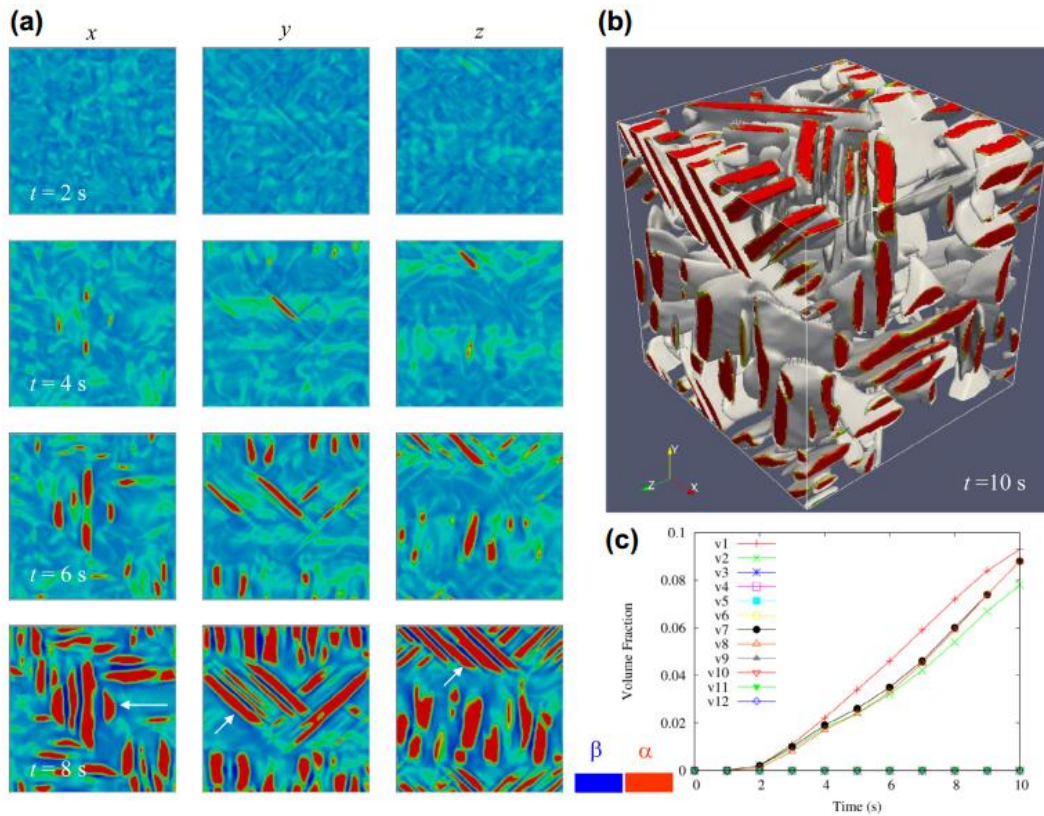


**Fig. 1.7** Variant selection and microstructure development under a pre-stain obtained via a



compressive stress (50 MPa) along  $[010]_{\beta}$ . **(a)** 2-D cross-sections showing microstructure evolution (color online, with the  $\alpha$  phase shown in red and the  $\beta$  phase shown in blue). Arrows indicate regions with a transformation texture. **(b)** 3-D microstructure obtained at  $t = 10$  s. **(c)** Volume fraction of each variant as a function of time [34].

Among the possible external factors, the imposed external deformation is an important and an effective factor to affect variant selection due to the specific lattice deformation of the  $\beta$  to  $\alpha$  phase transformation. Investigations through examining the global transformation texture features have evidenced that either under a direct external deformation or a prior deformation (deformation happened before the transformation) the number of intragranular  $\alpha$  variants is reduced depending on the slip system activated in the plastic deformation [61-63]. To reveal variant selection within individual  $\beta$  grains under an external deformation, the 3-D phase field simulation has been conducted, as shown in Fig. 1.7. Results show that under a compressive pre-strain along the  $[010]_{\beta}$  of a  $\beta$  grain, 4 variants can be selected but under tension, 8 variants can be selected [34].

## 1.4 Hot deformation behavior of metastable $\beta$ titanium alloy

Hot working is an important processing procedure for metal forming and mechanical property optimization, and thus widely used for the manufacturing of metallic materials, such as steels [64-69], Titanium alloys [70-74], Aluminum alloys [75, 76], and NiTi shape memory alloys [77, 78]. During the process, two opposite effects - hardening from crystal defect multiplication and crystal reorientation, and softening from defect rearrangement or annihilation via recovery and recrystallization - interweave, resulting in characteristic stress-strain behavior and microstructure evolution. Thus the mechanical responses of the alloys during thermomechanical processes have been a topic of intensive experimental and theoretical investigations for process optimization and microstructure and mechanical property improvement.

### 1.4.1 Hot deformation in single $\beta$ phase region

Since the hot deformation is conducted in the single  $\beta$  phase region, only the  $\beta$  phase is

concerned. The investigations were mainly focused on the effect of deformation parameters, such as deformation strain rate, on microstructure evolution by recovery and/or recrystallization and texture change of the  $\beta$  phase [79-83]. For instance, F. Warchomicka et al. conducted a systematic analysis on the hot deformation behavior of a Ti-55531 alloy by means of EBSD measurement [83]. The results show that the deformation parameters have a significant influence on the type of grain boundary, the orientation and the dynamic recrystallization (DRX). As shown in Fig. 1.8, a large amount of dynamic recrystallized grains and low angle grain boundaries were formed during the hot deformation at higher strain rates.

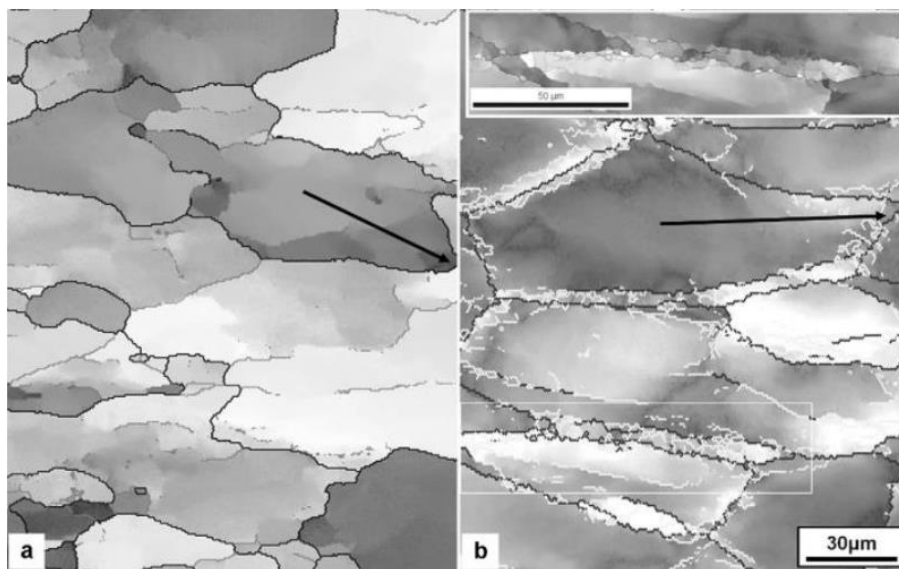


**Fig. 1.8** EBSD orientation map of samples deformed at 843°C up to 0.7: **(a)**  $0.01 \text{ s}^{-1}$  and **(b)**  $1 \text{ s}^{-1}$  (The black arrows are indicated in the recrystallized grains)[83].

For the metastable  $\beta$  titanium alloys, hot deformation induces dynamic recovery or recrystallization in  $\beta$  phase. Numerous studies revealed that the recovery and recrystallization in the metastable  $\beta$  titanium alloys are of the continuous dynamic type [84-89]. The higher deformation temperature and the lower strain rate can suppress the process of dynamic recrystallization.

### 1.4.2 Hot deformation in $\alpha+\beta$ phase region

For the hot deformation conducted in the  $\alpha+\beta$  two phase region, the initial microstructure consists of the two phases,  $\beta$  and  $\alpha$ . Since the deformation temperature is close to the

processing temperature, the topic has received much attention. Many investigations have been conducted on the deformation behavior of the alloys and the effect of deformation variables on microstructure evolution and on the underlying mechanisms. As displayed in Fig. 1.9, the hot deformation behavior, especially the hot compression behavior, is always characterized first by a linear stress-strain state, then by a drastic stress drop and finally by a steady-state.

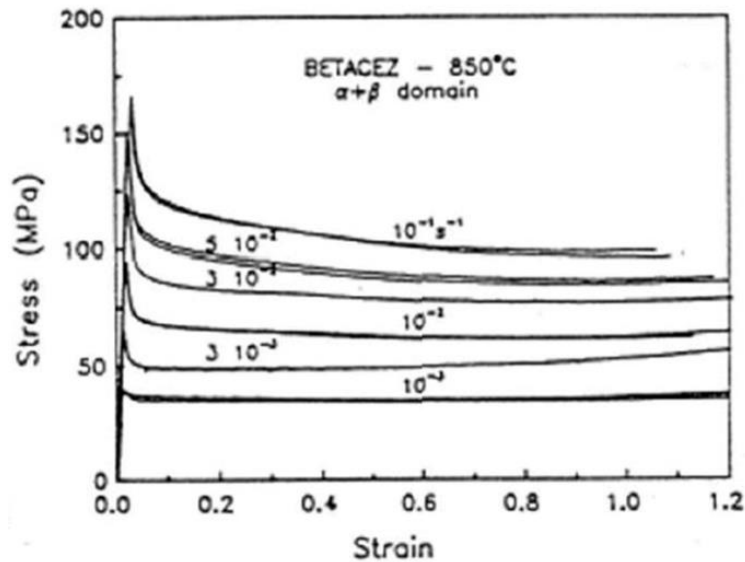


**Fig. 1.9** A typical stress-strain curve compressed at 850 °C in Ti-5Al-2Sn-4Mo-4Zr-1Fe (Beta CEZ) alloy [90].

The drastic stress drop stage normally is termed discontinuous yielding behavior. This behavior attracts much attention over the past several years. In the past, the discontinuous yielding was considered to be related to the generation of mobile dislocation at the grain boundary regions [91-92]. It was believed that the upper yield stress ( $\sigma_{UY}$ ) is proportional to the cumulative mobile dislocation densities. The reduced degree of mobile dislocations dominated the lower yield stress ( $\sigma_{LY}$ ). Moreover, the stress drop is defined as  $\Delta\sigma = \sigma_{UY} - \sigma_{LY}$ . For instance, Philippart and Rack [91] investigated the discontinuous yielding behavior of a metastable  $\beta$  titanium alloy during hot deformation. The stress drop was attributed to the dynamic recovery of the mobile dislocations that were generated from  $\beta$  grain boundaries. The subsequent stress oscillation was attributed to the dynamic recrystallization of the  $\beta$  grains. Similar stress drop and oscillation behavior were also observed in dual phase titanium alloys during hot deformation at the temperatures near  $\beta$  transus. In addition, in recent years,



it was proved that the discontinuous yielding was a result of stress induced reverse phase transformation ( $\alpha \rightarrow \beta$ ) [93-95]. This was concluded based on the evidence that the stress concentration at the  $\alpha$  grain boundaries could induce the  $\alpha \rightarrow \beta$  phase transformation during superplastic deformation in a two-phase Ti-Al-Fe alloy [95]. As displayed in Fig. 1.10, Jonas et al. [94] observed that the harder  $\alpha$  phase transforms dynamically into the softer  $\beta$  phase when the deformation was carried out below the  $\beta$  transus temperature. The similar results were also obtained by Jing et al. [93]. Moreover, they proved that the magnitude of the stress drop increased with the increasing of the fraction of stress induced phase transformation. Nevertheless, the specific softening mechanism related to the discontinuous yielding phenomenon is still unclear for the lack of the experimental observations.

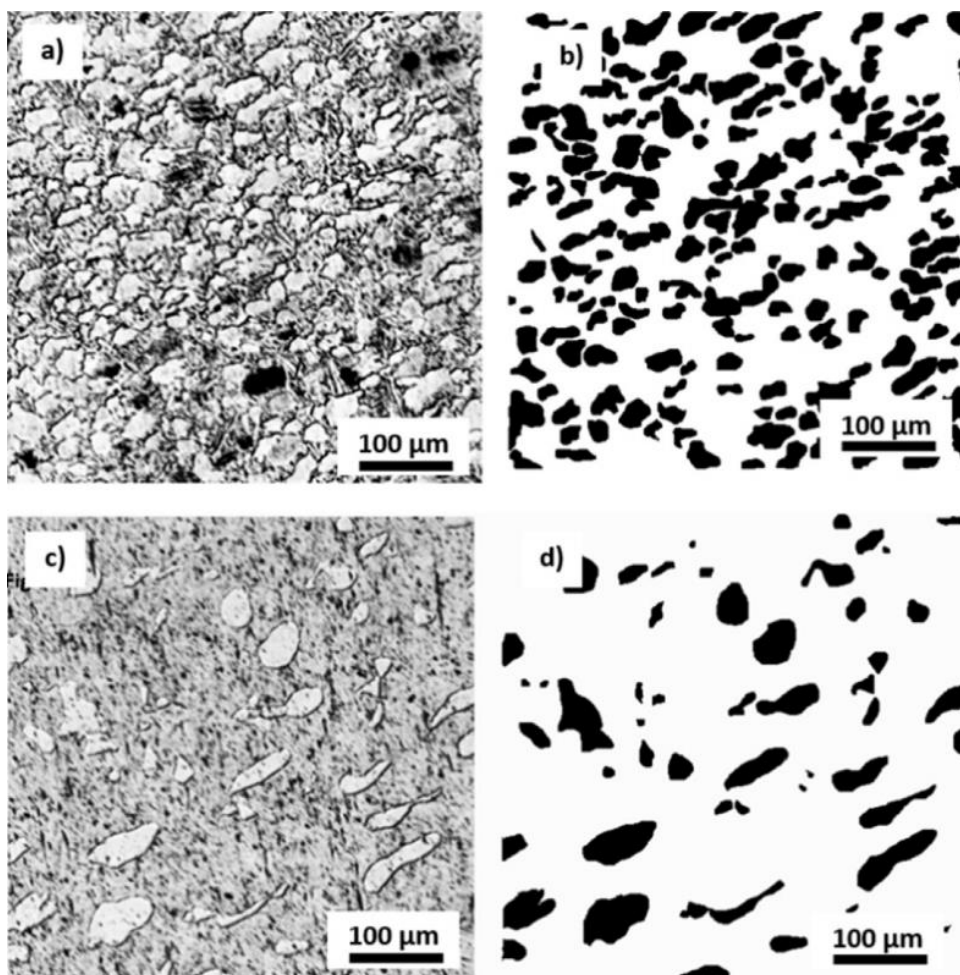


**Fig. 1.10** Optical microstructures of the IMI-834 alloy a), b) undeformed and c), d) deformed to  $\epsilon = 1$  at  $0.01 \text{ s}^{-1}$  and quenched from  $1000^\circ\text{C}$ . The volume fraction of  $\beta$  increases by about 20% on straining [94].

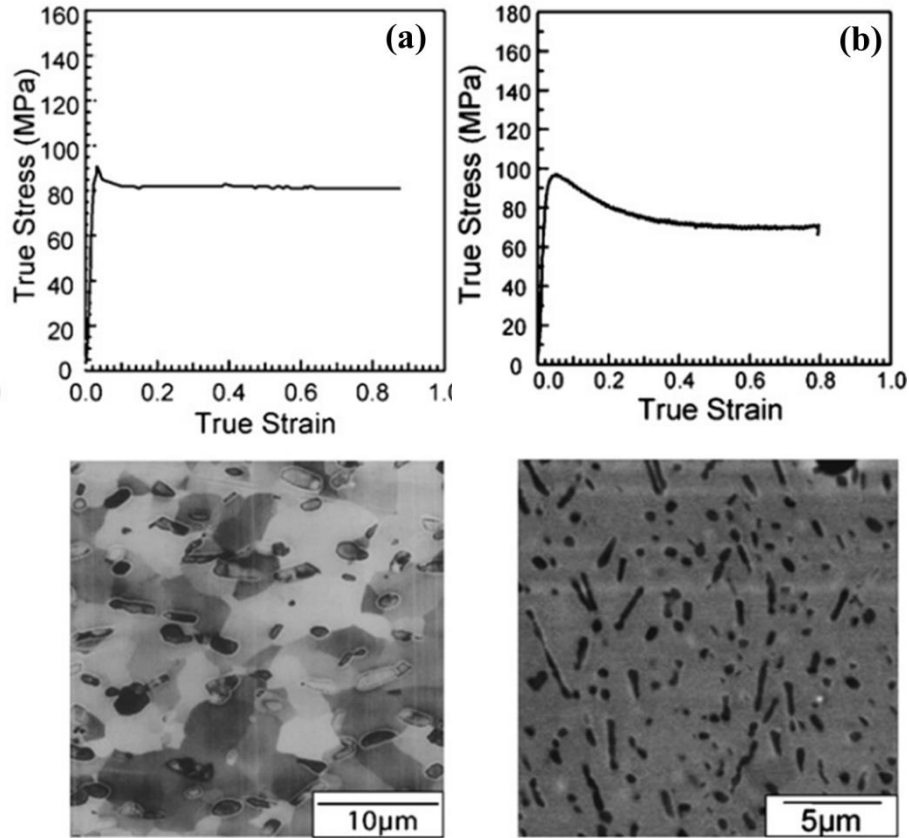


**Fig. 1.11** The BSE images of two different initial microstructures of Ti-1023 alloy compressed at 760 °C at a strain rate of  $10^{-2}\text{s}^{-1}$ . Corresponding flow curves are directly above images [96].

Followed by the discontinuous yielding, the steady-state in the stress-strain curve is presented in general. It is found that this steady state is a result of a counterbalance between work hardening and work softening. Dislocation slip has been considered as the main deformation mechanism and the dynamic recovery is the dominant mechanism for the restoration of the  $\beta$  phase [96-100]. Moreover, the effects of the secondary phase ( $\alpha$  phase), especially its distribution, size and morphology, on deformation behavior have also been studied [83, 99-106]. For instance, Jones et al. [99] found that the flow softening observed in a Ti-5553 alloy is thought to be caused by high aspect ratio of  $\alpha$  laths, acting as barriers to dislocation movement, resulting in dislocation pileup at the  $\alpha/\beta$  interface. Jackson et al. [96] investigated the effect of initial microstructure on plastic flow behavior of Ti-1023 and revealed that the flow behavior was highly depended on the original morphology of the  $\alpha$  phase, as displayed in Fig. 1.11. It is suggested that the breakup of the Widmanstätten  $\alpha$

platelets leads to the intense flow softening. Despite the large amount of experimental investigations and theoretical simulations, the hot deformation of metastable  $\beta$  titanium alloys with an initial single  $\beta$  phase in the  $\alpha+\beta$  two phase region has seldom been addressed. The deformation process should be more complicated as the  $\beta$  to  $\alpha$  phase transformation happens naturally in this temperature region.

## **1.4 Organization of the thesis**

As shown above, although the studies on the displacive characters of the  $\beta$  to  $\alpha$  transformation have greatly advanced our knowledge on the formation of specific microstructural features of the  $\alpha$  phase in titanium alloys, investigations on the constituents of individual  $\alpha$  precipitates and their correlation with the transformation strain are still limited. In addition, despite the numerous theoretical and experimental investigations, when the  $\alpha$  variant selection happened during thermomechanical processing, the possible interplay between the imposed external deformation and the internal transformation lattice deformation is still not clearly addressed. The reported selection mechanisms stay applicable for individual situations. Moreover, the hot deformation of the metastable  $\beta$  titanium alloys with an initial single  $\beta$  phase in the  $\alpha+\beta$  two phase region has seldom been reported, and the influence of the transformation, especially the transformation associated lattice deformation, on the mechanical response of the alloy has not yet been addressed.

In order to control the microstructure, to understand processing microstructure-property relationships, and thus to tailor manufacturing conditions to obtain specific mechanical properties through thermomechanical processing, it is of significant importance to investigate phase transformation behavior and variant selection mechanisms for its occurrence at different scales. Thus, the objective of the current work is to investigate phase transformation behavior and the  $\alpha$  variant selection during the thermomechanical processing. The scale of studies on variant selection is varied from the individual parent grain to the whole polycrystalline  $\beta$  sample. Meanwhile, the correlation between the hot deformation behavior and the microstructure evolution was made. In the present work, a metastable  $\beta$  titanium alloy, Ti-7Mo-3Nb-3Cr-3Al (wt. %, Ti-7333), was chose to be the subject material.

In Chapter 3, a thorough crystallographic study on  $\alpha$  precipitates, especially their

sub-structures, was conducted in the Ti-7333 alloy under heat treatment condition. To obtain the  $\alpha$  precipitates produced by the displacive process of the transformation that happens at the very beginning of the formation of  $\alpha$  phase, the specimens were aged very shortly after the over  $\beta$  transus solution treatment.

In Chapter 4, a thorough investigation with statistical significance on phase transformation and variant selection in the Ti-7333 alloy under uniaxial isothermal compression was conducted at two temperatures (700 °C and 600 °C). Special attention was paid to the interplay between the transformation strain and the imposed strain and the applied load.

In Chapter 5, a study on the correlation between the microstructure evolution and the hot compression stress-strain behavior was conducted. The effort was made to resolve the underlying mechanisms of the hot deformation behavior of the alloy. Special attention was paid to the contribution of the  $\beta$  to  $\alpha$  phase transformation at different deformation stages.

The final conclusions and perspective on some future directions that would extend the current work are presented in Chapter 6.

## Chapter 2 Materials, experimental details and basic crystallographic calculations

### 2.1 Materials preparation

The material used in the present work is a metastable  $\beta$ -Ti alloy, Ti-7Mo-3Nb-3Cr-3Al (wt. %, Ti-7333). This alloy was prepared first by multiple vacuum arc-melting and then by forging in the  $\beta$  and the  $\alpha+\beta$  phase region. The composition was analyzed by capacity chemical analysis method and is given in Table 2.1. The  $\beta$  transus temperature of this alloy measured by the metallographic method is approximately 850 °C.

**Table 2.1** The chemical composition of Ti-7333 (wt. %)

Mo	Nb	Cr	Al	Fe	C	O	H	Ti
7.18	2.99	2.94	3.00	0.038	< 0.1	0.11	< 0.1	Bal.

Cylindrical specimens with 15 mm in height and 10 mm in diameter were cut out of the center part of the forged Ti-7333 bar (150 mm in diameter). All the specimens in the present studies were first solution-treated at 900 °C in the  $\beta$  phase region for 30 min followed by water quenching to obtain a homogeneous single  $\beta$  microstructure. All the specimens in the work in Chapter 3, 4 and 5 were further treated with this initial microstructure.

### 2.2 Experimental details

#### 2.2.1 Thermal mechanical processing

In the present work, the thermal mechanical processing constituted two parts, the one being the heat treatment and the other the isothermal hot compression. For the heat treatment, the as-solution-treated specimens were aged at 700 °C for 5 minutes and quenched in ice water to allow one part of the  $\beta$  phase transforming to  $\alpha$  phase. This experiment provided the specimens for the analysis constituting the work in Chapter 3. For the hot compression

process, the as-solution-treated specimens were compressed using a Gleeble-3500 thermo-mechanical simulator under vacuum. The specimen was first heated to the compression temperature at a rate of  $25^{\circ}\text{C}/\text{s}$  and held for 5 seconds to homogenize the temperature. Then they were compressed at a strain rate of  $10^{-3}\text{ s}^{-1}$  to a defined reduction and quenched in ice water to preserve the deformed microstructure. The compression temperatures were  $700^{\circ}\text{C}$  and  $600^{\circ}\text{C}$ , respectively, in the present work (for Chapter 4 and 5). The deformation (in reduction) was designed from a true strain of 0.015 to 0.35 (0.015, 0.025, 0.03, 0.04, 0.10 and 0.35). During the hot compression, a thermocouple was welded at the mid span of the specimens to measure the temperature. Two pieces of thin tantalum sheets were placed between the specimen and the compressive die to reduce the friction and to maintain a uniform deformation. A schematic chart of the isothermal treatment and the isothermal compression processes is shown in Fig. 2.1.

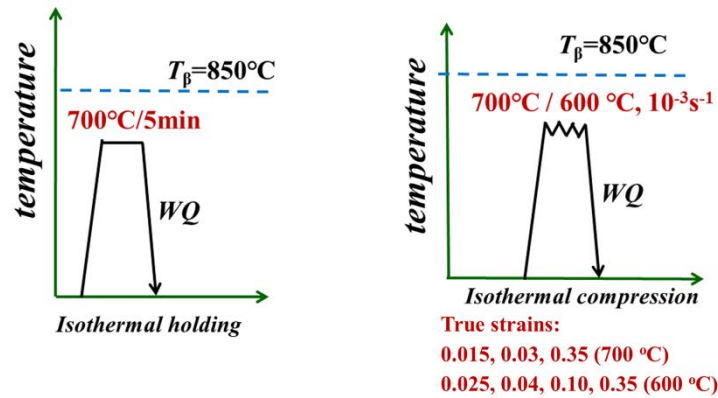


**Fig. 2.1** Schematic charts of isothermal treatment and the isothermal compression used in the present work.  $T_{\beta}$  stands for the  $\beta$  transus temperature.

### 2.2.2 Determination of the lattice constants

The lattice constants of the constituent phases at  $700^{\circ}\text{C}$  were measured in-situ by neutron diffraction. The through-volume measurements were performed with the neutron diffractometer STRESS-SPEC located at a thermal beam port of FRM-II in Garching, Germany. The Ge (311) monochromator was selected to produce neutrons with a wavelength of  $1.618\text{ \AA}$ . The bulk specimen with dimensions of  $\Phi 5 \times 15\text{ mm}$  was inserted into a vanadium crucible and immersed in the neutron beam with a size of  $5 \times 10 \times 10\text{ mm}^3$  under vacuum to

prevent oxidation of the specimens at elevated temperatures. The specimen was heated to 700 °C and isothermally held for 50 min, and then cooled at a rate of 12 °C/min. A thermocouple was inserted from the top of the crucible to record the temperature of the specimen. Neutron diffraction patterns were collected *in-situ* during the isothermal holding and the cooling at each 30 seconds. The  $(110)_\beta$  and  $(100)_\alpha$ ;  $(002)_\alpha$ ;  $(101)_\alpha$  diffraction peaks were captured at the detector position  $2\theta=41^\circ$  with a detector window of  $15^\circ$ . The instrument parameters were fitted by the measurement of Si powder. The software StressTextureCalculator (STeCa) [107] was used to extract diffraction patterns. The measured lattice constants of the constituent phases will be used for analyses in Chapter 3, 4 and 5.

### 2.2.3 Isothermal compression under *in-situ* neutron diffraction

The isothermal compression was also performed *in-situ* under neutron diffraction measurements at 700 °C to the as-solution-treated specimens with the dimensions of  $\Phi 5\text{mm} \times 10\text{mm}$ , using the rotatable multifunctional (tension/compression/torsion) loading frame incorporated in the STRESS-SPEC instrument. The loading frame was also integrated with a clip-on extensometer and a home-made inductive heating system. The specimens were heated in air to 700 °C at a rate of 50 °C /s, then isothermally compressed to a true strain of 0.35 (30% in reduction) and finally cooled with compressed air. The neutron diffraction measurements were performed using the neutron diffractometer STRESS-SPEC located at a thermal beam port of FRM-II (Garching, Germany). The Ge (311) monochromator was selected to reflect neutrons with a wavelength of 1.7076 Å. The  $\{110\}_\beta$  diffraction peak (corresponding to  $\beta$  phase) and the  $\{0002\}_\alpha$  and  $\{10\bar{1}1\}_\alpha$  diffraction peaks (corresponding to  $\alpha$  phase) were recorded at the detector position of  $2\theta=42^\circ$  with a window of  $15^\circ$ . The diffraction patterns were collected *in-situ* during the heating, isothermal compression and cooling processes each at every 20 seconds. The  $\{110\}_\beta$  pole figure of the un-deformed specimen (as-solution treated) and the  $\{110\}_\beta$  and  $\{0002\}_\alpha$  pole figures of the same specimen after the deformation were measured *ex-situ* to find out the orientation evolution.. The gauge volume of the specimens for the pole figure measurements was  $\Phi 5 \times 10 \text{ mm}$ . The software StressTextureCalculator (STeCa) [107] was used to extract the diffraction patterns. This experiment is corresponding to the work in Chapter 5.

## **2.2.4 Microstructural and crystallographic characterization**

The microstructural and crystallographic features of the specimens were examined by post mortem characterization techniques from the macroscopic scale to the microscopic scale to ensure a statistical relevance of the results. For the phase constituents and the morphological features, the specimens were examined using a Jeol JMF6500-F SEM and Supra 40 Zeiss SEM. For the crystallographic features, the specimens were examined using a JEOL 6500F SEM equipped with an EBSD acquisition camera and the Aztech online acquisition software package (Oxford Instruments). The data were processed using Channel 5 (Oxford Instruments) and ATEX software [108]. For the deformed specimens, the examined total area covers the whole homogeneous deformation region in the cross section. To achieve the surface quality for SEM observations and the EBSD measurements, the specimens were first mechanically polished and then electrolytically polished with a solution of 10% per-chloric acid in methanol at 35 V for 5 seconds at a temperature lower than 5°C. The EBSD measurements were conducted both automatically and manually. The automatic measurements were performed under the beam controlled mode with a step size of 2µm for the global measurements and with a step size of 70 nm for the local fine measurements. The manual measurements were conducted for the determination of the crystallographic features of fine  $\alpha$  constituents.

The nano scaled microstructural and crystallographic features of the constituent phases were analyzed using a Philips CM 200 transmission electron microscope (TEM) operated at 200 kV. The TEM is equipped with a LaB6 cathode, a Gatan Orius 833 CCD camera, and homemade automatic orientation analysis software – Euclid’s Phantasies (EP) [109]. The TEM thin films were prepared first by mechanical thinning and then by electrolytic polishing to perforation in a solution of 5% perchloric acid in ethanol at a voltage of 35V and at temperatures lower than -35°C, using a Struers Tenupol-5 twin-jet electropolisher. The microstructural and crystallographic characterization were used for the analysis work in Chapter 3, 4 and 5.



## 2.3 Basic crystallographic calculation

### 2.3.1 Coordinate system setting

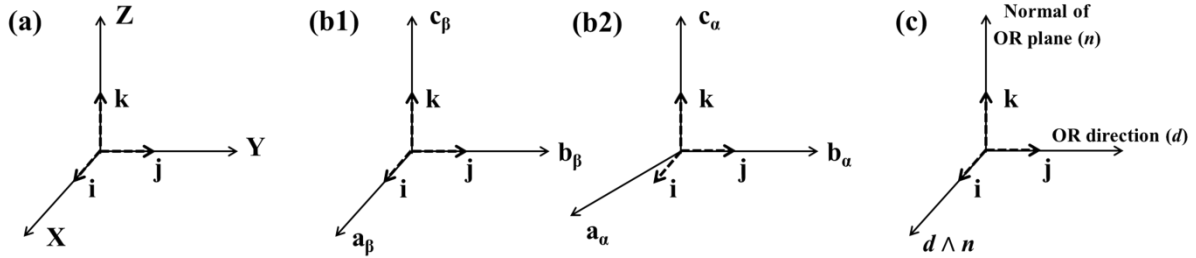


**Fig. 2.2** (a) Relationship between the Cartesian coordinate system ‘i-j-k’ and macroscopic sample coordinate system; (b) Relationship between the Cartesian crystal coordinate system ‘i-j-k’ and the Bravais lattice basis of the  $\beta$  phase (BCC) ‘ $a_\beta$ - $b_\beta$ - $c_\beta$ ’ (b1) and the Bravais lattice basis of the  $\alpha$  phase (HCP) ‘ $a_\alpha$ - $b_\alpha$ - $c_\alpha$ ’ (b2); (c) Relationship between the Cartesian OR coordinate system ‘i-j-k’ and the OR plane and OR direction of the crystal.

There are two phases in the present PhD work, *i.e.*  $\beta$  phase (cubic: BCC) and  $\alpha$  phase (hexagonal: HCP). Three Cartesian coordinate systems were used in the crystallographic calculations in the present PhD work in addition to the Bravais lattice basis of the  $\beta$  phase and the  $\alpha$  phase. The first Cartesian coordinate system is set to the specimen, termed as macroscopic sample coordinate system ‘X-Y-Z’, as shown in Fig. 2.2 (a). The second Cartesian coordinate system is related to the Bravais lattice of the corresponding phase ( $\beta$  and  $\alpha$ ), termed as Cartesian crystal coordinate system. The relation between the Cartesian crystal coordinate system and the Bravais lattice basis conforms to the convention described in the Channel 5 software package, as illustrated in Fig. 2.2 (b1) and (b2). Since the phase transformation in solid state is always accompanied with a specific transformation orientation relationship (OR) between the parent phase and the product phase in many metals and alloys, the OR can be used to relate the parent and product phases. The OR usually is defined by a pair of parallel crystallographic planes and a pair of parallel crystallographic directions in the OR plane from the corresponding parent and product phase. It can be demonstrated as:  $\{h_1 \ k_1 \ l_1\} \parallel (h_2 \ k_2 \ l_2)$  and  $\langle u_1 \ v_1 \ w_1 \rangle \parallel [u_2 \ v_2 \ w_2]$ . The phases used in the present work are  $\beta$  phase

(BCC structure) and  $\alpha$  phase (HCP structures). In most case, the OR between these two phases is the Burgers Orientation Relationship (BOR). The detailed Miller indices of the BOR can be described as:  $\{110\}_\beta // (0001)_\alpha$  and  $\langle 1\bar{1}1 \rangle_\beta // [11\bar{2}0]_\alpha$ . Hence, the third one, the Cartesian coordinate system is set to relate the  $\beta$  phase and  $\alpha$  phase through the BOR, termed as Cartesian OR coordinate system. In this coordinate system, the basis vector  $j$  is parallel to the OR direction,  $k$  is parallel to the normal of the OR plane and  $i$  is parallel to the vector cross product of the OR direction and the normal of the OR plane, as illustrated in Fig. 2.2(c).

## 2.3.2 Coordinate transformation

### 2.3.2.1 Transformation between macroscopic sample coordinate system and Cartesian crystal coordinate system

As is known, in a polycrystalline material there exist large amounts of differently oriented crystals. In order to describe the orientation of the crystals, the concept of a triplet rotations represented in Euler angles is usually used. In the present work, the Euler angles ( $\varphi_1$   $\Phi$   $\varphi_2$ ) under Bunge notation [110, 111] are adopted. The definition of the three rotations  $\varphi_1$ ,  $\Phi$  and  $\varphi_2$  are illustrated in Fig. 2.3, where the ‘X-Y-Z’ represents the macroscopic sample coordinate system. Thus, the Cartesian crystal coordinate system is associated with the specimen coordinate system with the Euler angles. The coordinate transformation matrix  $M_E$  from the macroscopic sample coordinate system to the Cartesian crystal coordinate system can be described in Eq. (2.1). The coordinate transformation matrix from the Cartesian crystal coordinate system to the macroscopic sample coordinate system is the inverse of  $M_E$ .

$$M_E = \begin{pmatrix} \cos \varphi_1 \cos \varphi_2 - \sin \varphi_1 \sin \varphi_2 \cos \Phi & -\cos \varphi_1 \sin \varphi_2 - \sin \varphi_1 \cos \varphi_2 \cos \Phi & \sin \varphi_1 \sin \Phi \\ \sin \varphi_1 \cos \varphi_2 + \cos \varphi_1 \sin \varphi_2 \cos \Phi & -\sin \varphi_1 \sin \varphi_2 + \cos \varphi_1 \cos \varphi_2 \cos \Phi & -\cos \varphi_1 \sin \Phi \\ \sin \varphi_2 \sin \Phi & \cos \varphi_2 \sin \Phi & -\cos \Phi \end{pmatrix} \quad (2.1)$$

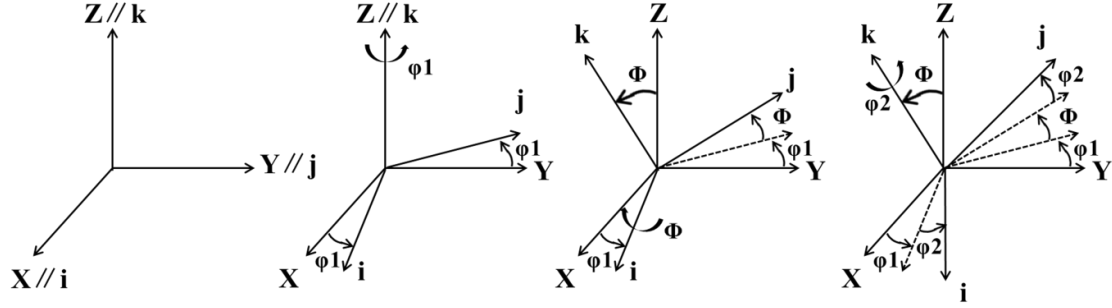


**Fig. 2.3** Illustration of the three rotations in Bunge notation. ‘X-Y-Z’: macroscopic sample coordinate system; ‘i-j-k’: Cartesian crystal coordinate system.

### 2.3.2.2 Transformation between Cartesian crystal coordinate system and Bravais lattice coordinate system

In addition to the coordinate transformation between the Cartesian crystal coordinate system and the macroscopic sample coordinate system, there exists another coordinate transformation from the Cartesian crystal coordinate system to the Bravais lattice coordinate system in the present work. In the present PhD work, for  $\beta$  phase crystal,  $a=b=c$  and  $\alpha=\beta=\gamma=90^\circ$ , thus the coordinate transformation matrix  $M_C^\beta$  from the  $\beta$  phase Cartesian crystal coordinate system to the Bravais lattice coordinate system can be expressed as:

$$M_C^\beta = \begin{pmatrix} a & 0 & 0 \\ 0 & a & 0 \\ 0 & 0 & a \end{pmatrix} \quad (2.2)$$

For the  $\alpha$  phase crystal,  $a=b \neq c$ ,  $\alpha=\beta=90^\circ$ , and  $\gamma=90^\circ$ , thus the coordinate transformation matrix  $M_C^\alpha$  from the  $\alpha$  phase Cartesian crystal coordinate system to the Bravais lattice coordinate system can be expressed as:

$$M_C^\alpha = \begin{pmatrix} \sqrt{3} a/2 & 0 & 0 \\ -a/2 & a & 0 \\ 0 & 0 & c \end{pmatrix} \quad (2.3)$$

### 2.3.2.3 Transformation between $\beta$ phase Cartesian crystal coordinate system and $\alpha$ phase Cartesian crystal coordinate system under BOR

Since there is the BOR between the  $\beta$  phase and the  $\alpha$  phase in the present work, the transformation matrix can be established through the OR. According to the geometrical relations between the OR plane normal and OR direction, three basis vectors of the Cartesian

OR coordinate system can be obtained. Thus, the transformation matrix from Cartesian crystal coordinate system to the Cartesian OR coordinate system can be obtained. The transformation matrix from the  $\beta$  phase Cartesian crystal coordinate system to the Cartesian OR coordinate system is denoted  $M_{\beta 1}$ , and the transformation matrix from the  $\alpha$  phase Cartesian crystal coordinate system to the Cartesian OR coordinate system  $M_{\alpha 1}$ .

Thus, the coordinate transformation matrix from the  $\beta$  phase Cartesian crystal coordinate system to the  $\alpha$  phase Cartesian crystal coordinate system —  $M_{OR}$  can be expressed with the equation below and the schematic of coordinate transformation is shown in Fig. 2.4. It should be mentioned that all the matrix calculations used in the present dissertation are performed in matrix notation.

$$M_{OR} = M_{\beta 1} \times (M_{\alpha 1})^{-1}. \quad (2.4)$$

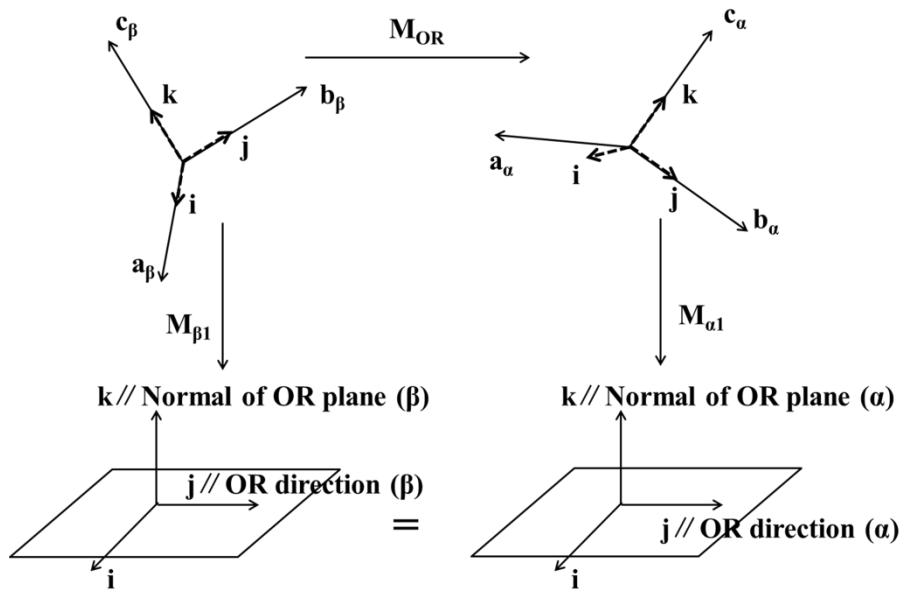


**Fig. 2.4** Schematic of coordinate transformation between the  $\beta$  phase Cartesian crystal coordinate system and  $\alpha$  phase Cartesian crystal coordinate system.

With this coordinate transformation matrix between the Cartesian crystal coordinate system of the  $\beta$  phase and that of the  $\alpha$  phase, whether the BOR is obeyed by the  $\beta$  phase and the  $\alpha$  phase can be verified with the measured orientations of the two phases. Moreover, with the detected Euler angles of the parent phase ( $\beta$  phase), the orientation of the product phase ( $\alpha$  phase) can be obtained by using the following equation:

$$M_E^\alpha = M_E^\beta \times S_i \times M_{OR} \quad (2.5)$$

Where  $M_E^\alpha$  is the coordinate transformation matrix from the macroscopic sample coordinate system to the Cartesian crystal coordinate system of the  $\alpha$  phase,  $M_E^\beta$  is the coordinate transformation matrix from the macroscopic sample coordinate system to the Cartesian crystal coordinate system of the  $\beta$  phase,  $S_i$  is the rotational symmetry matrices of the cubic crystal system. Hence, the orientation of  $\alpha$  phase can be calculated.

### 2.3.3 Stereographic projection

The stereographic projection is a two-dimensional (2D) map to represent the projection of a vector (or a plane normal) to the equatorial plane of the sphere, as illustrated in Fig. 2.5.

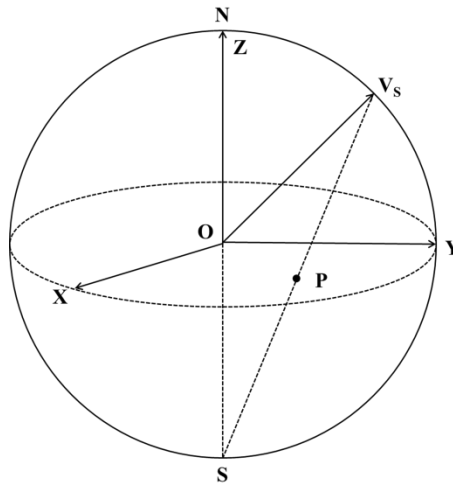


**Fig. 2.5** Illustration of stereographic projection on the equatorial plane XOY of vector  $OV_S$ . Point  $P$  is the projection pole of vector  $OV_S$  on the equatorial plane and point  $S$  is the south pole of the projection sphere.

To calculate the projection of a crystalline direction, this direction should be expressed under the coordinate system of the projection, for example the macroscopic sample coordinate frame, with the following equation:

$$V_S = M_E \times S_k \times M_c \times \begin{pmatrix} u \\ v \\ w \end{pmatrix}. \quad (2.6)$$

Here,  $M_E$  is the coordinate transformation matrix from the macroscopic sample coordinate system to the Cartesian crystal coordinate system,  $S_k$  is the rotational symmetry matrices of the crystal system,  $M_C$  is the coordinate transformation matrix from the Cartesian crystal coordinate system to the Bravais lattice basis and  $[u \ v \ w]$  is the Miller indices of the crystalline direction.

Suppose that the coordinates of vector  $V_S$  in the macroscopic sample coordinate system are  $[xV_S \ yV_S \ zV_S]$ , the radius of the projection sphere  $R$  should be:

$$R = (xV_S^2 + yV_S^2 + zV_S^2)^{1/2}. \quad (2.7)$$

If  $zV_S \geq 0$ , the equation of line  $V_S S$  can be expressed as:

$$\frac{x}{xV_S} = \frac{y}{yV_S} = \frac{z+R}{zV_S+R}. \quad (2.8)$$

Let  $z=0$ , the abscissa  $x$  and ordinate  $y$  of point  $P$  can be obtained. Suppose  $R=1$ , the abscissa and ordinate values of the stereographic projection of the vector are:

$$\begin{aligned} x &= \frac{xV_S}{zV_S+1} \\ y &= \frac{yV_S}{zV_S+1} \end{aligned} \quad (2.9)$$

To plot the projection of a crystalline plane  $(h \ k \ l)$ , the normal vector  $\mathbf{n}$  should be calculated first with the following equation:

$$\mathbf{n} = G^* \times \begin{pmatrix} h \\ k \\ l \end{pmatrix} \quad (2.10)$$

where  $G^*$  is the reciprocal metric tensor [112] of the corresponding crystal system:

$$G^* = \begin{pmatrix} a^* \cdot a^* & a^* \cdot b^* & a^* \cdot c^* \\ b^* \cdot a^* & b^* \cdot b^* & b^* \cdot c^* \\ c^* \cdot a^* & c^* \cdot b^* & c^* \cdot c^* \end{pmatrix} \quad (2.11)$$

Here,  $a^*$ ,  $b^*$ ,  $c^*$  are the three basis vectors of the reciprocal space of the crystal. Then repeat the procedures using Eqs. (2.6) ~ (2.9), the stereographic projection of a given plane can be obtained.

### 2.3.4 Misorientation

In general, the misorientation between two crystals can be expressed in angle/axis pair —  $(\omega, d)$ , which describes a rotation from one symmetrically equivalent Cartesian crystal

coordinate system of one crystal to one symmetrically equivalent Cartesian crystal coordinate system of the other crystal. Normally, we use the Euler angles detected by experiment of the two crystals with respect to the macroscopic sample coordinate system to calculate the misorientation between these two crystals. In order to determine the  $(\omega, d)$ , the misorientation matrix  $\Delta M$  between the two crystals should be calculated first, as illustrated in Fig. 2.6.

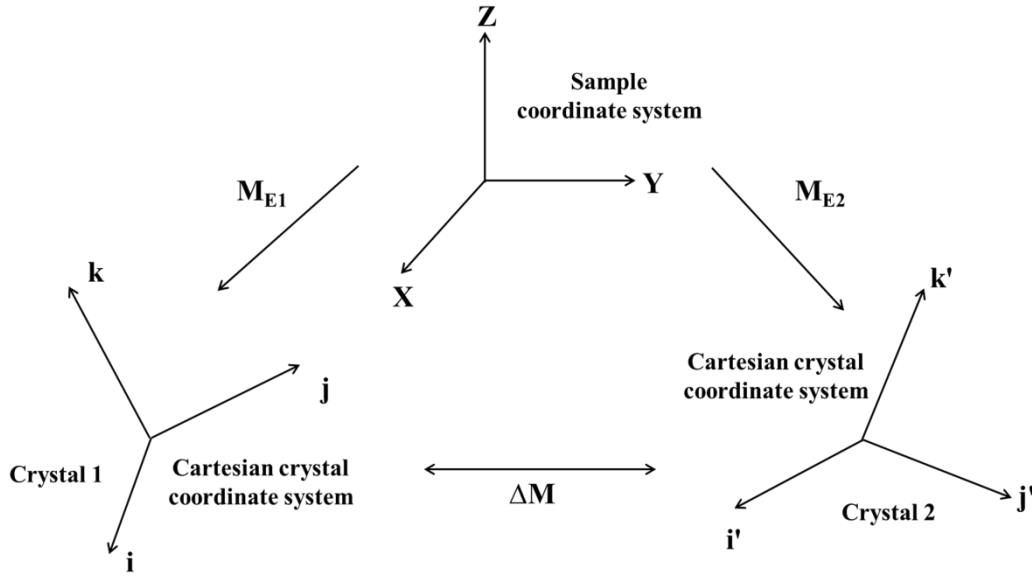


**Fig. 2.6** Schematic of misorientation between two crystals: ‘X-Y-Z’ is the macroscopic sample coordinate system. ‘i-j-k’ and ‘i'-j'-k'’ are the Cartesian crystal coordinate systems.  $M_{E1}$  and  $M_{E2}$  are coordinate transformation matrices from the macroscopic sample coordinate system to the Cartesian coordinate systems of the two crystals.  $\Delta M$  is the misorientation matrix between the two crystals.

The calculation of the misorientation matrix  $\Delta M$  between the two crystals can be described as follows:

$$\Delta M = (S_i)^{-1} \times (M_{E1})^{-1} \times M_{E2} \times S_j \quad (2.12)$$

where  $S_i$  and  $S_j$  represent the rotational symmetry matrices of these two crystals, i.e. crystal 1 and crystal 2. And  $M_{E1}$  and  $M_{E2}$  represent the coordinate transformation matrices from the macroscopic sample coordinate system to the Cartesian crystal coordinate system of these two crystals that are detected by experiments (normally the data are Euler angles). The misorientation matrix  $\Delta M$  can be described as below:

$$\Delta M = \begin{pmatrix} g_{11} & g_{12} & g_{13} \\ g_{21} & g_{22} & g_{23} \\ g_{31} & g_{32} & g_{33} \end{pmatrix}. \quad (2.13)$$

Then the misorientation angle  $\omega$  and its corresponding rotation axis  $d$   $[r_1 \ r_2 \ r_3]$  can be calculated and expressed in the same Cartesian crystal coordinate system of the crystal. The calculated method is described as follows:

$$\omega = \arccos \left( \frac{g_{11} + g_{22} + g_{33} - 1}{2} \right), \quad (2.14)$$

The corresponding rotation axis  $d$  can be calculated according to the value of the misorientation angle  $\omega$ :

when  $\omega = 0^\circ$ ,

$$d = [r_1 \ r_2 \ r_3] = [1 \ 0 \ 0]; \quad (2.15)$$

when  $0^\circ < \omega < 180^\circ$ ,

$$r_1 = \frac{g_{23} - g_{32}}{2 \sin \omega}; \quad r_2 = \frac{g_{31} - g_{13}}{2 \sin \omega}; \quad r_3 = \frac{g_{12} - g_{21}}{2 \sin \omega}; \quad (2.16)$$

When  $\omega = 180^\circ$ ,

$$r_1 = \pm \sqrt{\frac{g_{11} + 1}{2}}; \quad r_2 = \pm \sqrt{\frac{g_{22} + 1}{2}}; \quad r_3 = \pm \sqrt{\frac{g_{33} + 1}{2}}; \quad (2.17)$$

with  $\begin{pmatrix} |r_m| = \max(|r_i|, i = 1, 2, 3) \\ r_m > 0 \\ \forall i \neq m, r_i = \text{sign}(g_{im}) \cdot |r_i| \end{pmatrix}.$

Due to the crystallographic symmetry of each crystal system, the misorientation matrix between the two crystals is not unique. There will be several misorientation matrices. However, all these matrices are crystallographically equivalent and thus the calculated misorientation angle  $\omega$  and its corresponding rotation axis  $d$  are also crystallographically equivalent.

### 2.3.5 Trace analysis method

Trace analysis method is an efficient crystallographic characterization method to determine the interfaces and slip planes. Fig. 2.7 is the schematic illustration of the trace analysis method. As the figure shows, there is a macroscopic sample coordinate system 'X-Y-Z', and this frame will be used in this method. In this frame, as the figure displayed, the



upper plane ( $XOY$  plane) is the measured and observed plane or the specimen surface. There is a crystallographic plane ( $ABCD$  plane) marked with the red line in this frame. The blue line is the intersection line of the specimen surface  $XOY$  plane and the  $ABCD$  plane, *i.e.* the trace of the  $ABCD$  plane on the surface. Considering the  $XOY$  plane as the projection plane, the stereographic projection of the  $ABCD$  plane normal  $n$  should be in the plane that consists of  $n$  and  $Z$  axis. It means that the pole of the  $ABCD$  plane should be in the green line and the  $XOY$  plane displayed in the figure. As the trace line of the  $ABCD$  plane on the surface (the blue line) is perpendicular to  $n$  and the  $Z$  axis, the green line must be perpendicular to the trace line. Hence, for a measured crystallographic plane and the orientation information of the crystal, the trace of this crystallographic plane can be calculated and the plane can be identified. The calculated trace can be compared with the measured one by using pole figures, and then the Miller indices of this crystallographic plane can be determined.

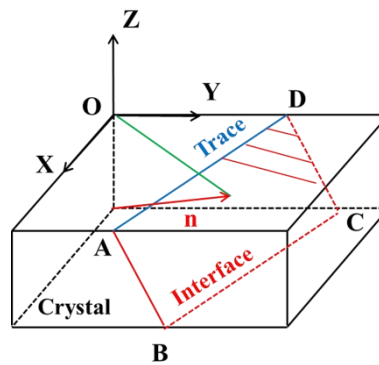


**Fig. 2.7** Schematic illustration of trace analysis method

### 2.3.6 Deformation gradient tensor

Generally, the  $\beta$  to  $\alpha$  phase transformation involves two processes: diffusion of the alloying elements and the structure transformation of the Ti atoms. The former results in a composition change of the product  $\alpha$  phase by depleting  $\beta$  stabilizing elements, such as Mo, Cr, Nb, and enriching the  $\alpha$  stabilizing elements, such as Al, whereas the latter gives rise to the structure change from BCC to HCP. The structure change from the  $\beta$  (BCC) to the  $\alpha$  (HCP) phase is accompanied by the movements of the Ti atoms, as shown in Fig. 2.8. The phase transformation can be realized by the structure change from the lattice cell of the  $\beta$  phase to the lattice cell of the  $\alpha$  phase. Hence, the deformation gradient tensor can be used to analyze the phase transformation lattice strain.

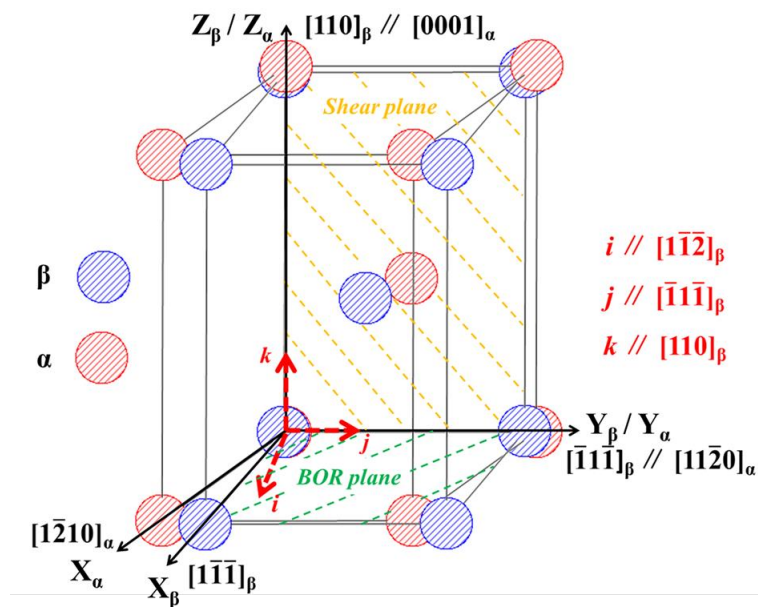


**Fig. 2.8** Schematics of  $\beta$  to  $\alpha$  transformation through lattice distortion

Since there exists the BOR between the  $\beta$  and the  $\alpha$  phase, two basic lattice cells of the two phases can be worked out firstly, as illustrated in Fig. 2.8. In addition, the Cartesian OR coordinate system ‘i-j-k’ can be set the two lattice cells through the OR. By analyzing the lattice correspondences, the structure change can be described quantitatively by using the deformation gradient tensor. Mathematically, the gradient tensor can be derived as follows. The basis vectors of the lattice cell of the  $\beta$  phase can be expressed in the Cartesian OR

coordinate system, as shown in Eq (2.18). Similarly, the basis vectors of the lattice cell of the  $\alpha$  phase can also be expressed in the Cartesian OR coordinate system, as shown in Eq (2.19).

$$\begin{cases} x_{\beta}=x_{\beta x}\mathbf{i} + x_{\beta y}\mathbf{j} + x_{\beta z}\mathbf{k} \\ y_{\beta}=y_{\beta x}\mathbf{i} + y_{\beta y}\mathbf{j} + y_{\beta z}\mathbf{k} \\ z_{\beta}=z_{\beta x}\mathbf{i} + z_{\beta y}\mathbf{j} + z_{\beta z}\mathbf{k} \end{cases} \quad (2.18)$$

$$\begin{cases} x_{\alpha}=x_{\alpha x}\mathbf{i} + x_{\alpha y}\mathbf{j} + x_{\alpha z}\mathbf{k} \\ y_{\alpha}=y_{\alpha x}\mathbf{i} + y_{\alpha y}\mathbf{j} + y_{\alpha z}\mathbf{k} \\ z_{\alpha}=z_{\alpha x}\mathbf{i} + z_{\alpha y}\mathbf{j} + z_{\alpha z}\mathbf{k} \end{cases} \quad (2.19)$$

Thus, the coordinate transformation matrix of the lattice cell of the  $\beta$  phase ( $G_{\beta d}$ ) and that of the  $\alpha$  phase ( $G_{\alpha d}$ ) expressed in the Cartesian OR coordinate system ' $\mathbf{i-j-k}$ ' can be obtained, as displayed in Eq (2.20) and Eq (2.21), respectively.

$$G_{\beta d} = \begin{pmatrix} x_{\beta x} & y_{\beta x} & z_{\beta x} \\ y_{\beta y} & y_{\beta y} & z_{\beta y} \\ z_{\beta z} & y_{\beta z} & z_{\beta z} \end{pmatrix}. \quad (2.20)$$

$$G_{\alpha d} = \begin{pmatrix} x_{\alpha x} & y_{\alpha x} & z_{\alpha x} \\ y_{\alpha y} & y_{\alpha y} & z_{\alpha y} \\ z_{\alpha z} & y_{\alpha z} & z_{\alpha z} \end{pmatrix}. \quad (2.21)$$

Then the deformation gradient tensor  $A_{ijk}$  from the  $\beta$  phase to the  $\alpha$  phase expressed in the Cartesian OR coordinate system ' $\mathbf{i-j-k}$ ' can be calculated by using Eq (2.22),

$$A_{ijk} = G_{\alpha d} \times (G_{\beta d})^{-1}. \quad (2.22)$$

The format of the deformation gradient tensor  $A_{ijk}$  can be established as follow:

$$A_{ijk} = \begin{pmatrix} \varepsilon_{11} & \varepsilon_{12} & \varepsilon_{13} \\ \varepsilon_{21} & \varepsilon_{22} & \varepsilon_{23} \\ \varepsilon_{31} & \varepsilon_{32} & \varepsilon_{33} \end{pmatrix} \quad (2.23)$$

$\varepsilon_{ii}$  ( $i=1, 2$  and  $3$ ), the diagonal elements, means elongation ( $\varepsilon_{ii}>1$ ) or contraction ( $\varepsilon_{ii}<1$ ) in the direction of  $i$ , whereas  $\varepsilon_{ij}$  ( $i$  and  $j=1, 2$  and  $3$ ), the off diagonal elements, means a shear in the direction of  $i$  and on the plane normal to  $j$ . The normal strain is accumulative in  $i$ , whereas the shear amount is proportional to the dimension in the direction normal to the shear plane, i.e. in  $j$ .

In order to analyze the interaction between the phase transformation lattice strain and the imposed strain during the macroscopic deformation, the deformation gradient tensor is needed to be expressed in the macroscopic deformation frame, i.e. the macroscopic sample coordinate

system ‘X-Y-Z’. The coordinate transformation of the tensor can be described as follows:

$$A_{xyz} = M_E^\beta \times S_i \times M_{\beta 1} \times A_{ijk} \times (M_{\beta 1})^{-1} \times (S_i)^{-1} \times (M_E^\beta)^{-1} \quad (2.24)$$

In Eq. (2.24), the matrix  $A_{ijk}$  represents the deformation gradient tensor expressed in the Cartesian OR coordinate system ‘*i-j-k*’. The  $M_E^\beta$  is the coordinate transformation matrix from the macroscopic sample coordinate system to the Cartesian crystal coordinate system of the  $\beta$  phase and the Euler angles to construct this matrix can be measured by EBSD measurements. The  $S_i$  is the rotational symmetry matrices of the cubic crystal system. The  $M_{\beta 1}$  is the coordinate transformation matrix from the  $\beta$  phase Cartesian crystal coordinate system to the Cartesian OR coordinate system ‘*i-j-k*’ in Fig. 2.8. By this, the deformation gradient tensor can be expressed in the macroscopic sample coordinate system based on the measured Euler angles. Hence, the interplay between the phase transformation lattice strain and the macroscopic deformation can be analyzed.

## **Chapter 3 Microstructure evolution and phase transformation under heat treatment**

### **3.1 Introduction**

For the Al containing metastable  $\beta$  titanium alloys, the high temperature  $\beta$  phase with body-centered cubic (BCC) structure transforms to the lower-temperature equilibrium  $\alpha$  phase with hexagonal close-packed (HCP) structure when the alloy is slowly cooled across the  $\beta$  transus temperature ( $T_\beta$ ), or isothermally held at a temperature below  $T_\beta$ . Generally, the  $\beta$  to  $\alpha$  phase transformation involves two processes: diffusion of alloying elements and structure transformation of Ti atoms. The former results in a composition change of the product  $\alpha$  phase by depleting  $\beta$  stabilizing elements, such as Mo, Cr, Nb, and enriching  $\alpha$  stabilizing elements, such as Al, whereas the latter gives rise to the structure change from BCC to HCP. For the structure change, the transformation strain can be self-accommodated by locally forming specific variants, giving rise to the appearance of characteristic microstructure patterns depending on the internal stress and the external stress conditions. In this chapter, a thorough crystallographic study on  $\alpha$  precipitates, especially their sub-structures, was conducted in Ti-7333 in view of the displacive characters of the transformation. This work will provide new information concerning the phase transformation for the metastable  $\beta$  Ti alloys.

### **3.2 Experimental**

In this chapter, the as-solution-treated Ti-7333 specimen was heated treated (aged) at 700°C for 5 mins and water quenched. The detailed information on sample preparation is given in 2.1 (Page 18) Chapter 2. The lattice constants of the constituent phase were measured by neutron diffraction at treatment temperature. The microstructural and crystallographic features were investigated by SEM-EBSD and TEM.

### 3.3 Microstructure of the initial $\beta$ phase and lattice constant information

Fig. 3.1 (a) shows the microstructure of the solution-treated Ti-7333 alloy that consists of equiaxed  $\beta$  grains with an average size of about 200  $\mu\text{m}$ . The disorientation angle distribution of the  $\beta$  grains is shown in Fig.1 (b). It is seen that the  $\beta$  grains do not display any preferred crystallographic orientations or texture. Moreover, the amount of low angle disorientation ( $<5^\circ$ ) is very low, indicating that the  $\beta$  grains possess high crystalline perfection.

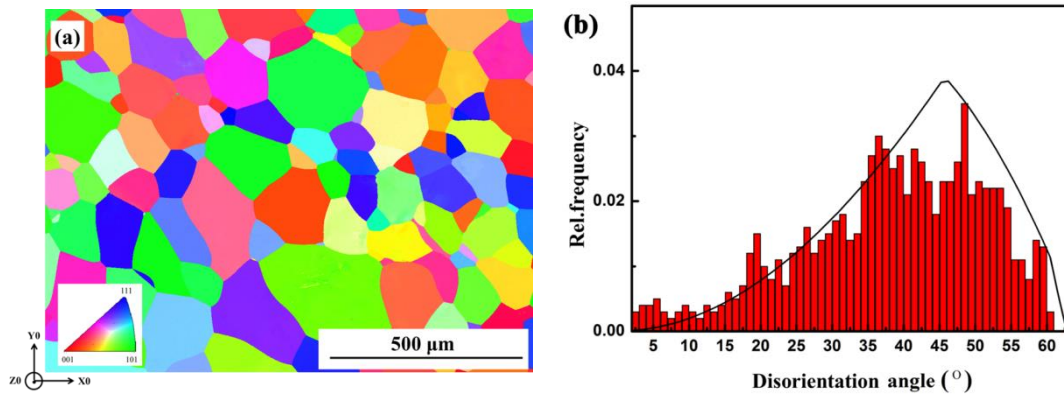


**Fig. 3.1** (a) SEM-EBSD expressed with Y0 direction inverse pole figure (IPF) micrograph of the solution-treated Ti-7333 alloy and (b) Disorientation angle distribution of  $\beta$  phase, where the disorientation angle distribution of theoretical randomly oriented cubic polycrystal is represented with line profile. The insert in (a) is the color code of the IPF.

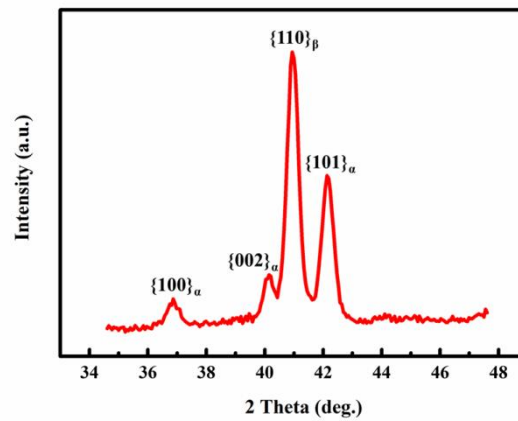


**Fig. 3.2** Neutron diffraction pattern in the  $2\theta$  =range  $34^\circ$  to  $49^\circ$  of the Ti-7333 alloy acquired at  $700^\circ\text{C}$

Fig. 3.2 shows the diffraction pattern of the  $\beta$  phase and  $\alpha$  phase acquired at 700°C (the aging temperature). Analysis of the diffraction data confirmed that the  $\beta$  phase has a BCC structure with lattice parameters  $a=3.2471\text{\AA}$ ; whereas the  $\alpha$  phase possesses a HCP structure with lattice parameters  $a=2.9340\text{\AA}$  and  $c=4.6795\text{\AA}$ . The lattice constants of the two phases are slightly different from the data reported in Pearson's handbook [113]. This is due to the influence of the temperature and the alloying elements. The lattice constants will directly affect the lattice strain during the  $\beta$  to  $\alpha$  transformation. This part will be developed latter.

### 3.4 Phase transformation under heat treatment

#### 3.4.1 Microstructure characteristics of $\alpha$ precipitates

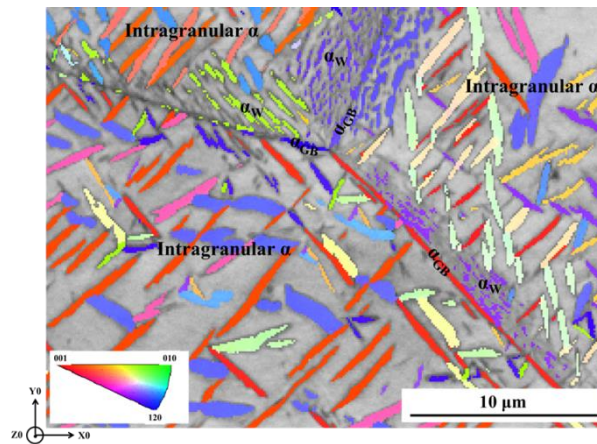


**Fig. 3.3** SEM-EBSD micrograph of Ti-7333 alloy after solution treatment at 900°C for 30 min and aged at 700°C for 5 min demonstrating grain boundaries  $\alpha$  ( $\alpha_{GB}$ ), Widmanstätten  $\alpha$  ( $\alpha_W$ ) at the vicinities of  $\beta$  grain boundaries and intragranular  $\alpha$ . The  $\beta$  matrix is represented with its EBSD band quality contrast and the  $\alpha$  precipitates with their crystallographic orientation (expressed with the Z0 direction inverse pole figure (IPF)). The insert is the color code of the IPF.

Fig. 3.3 shows the microstructure of the alloy after 5 minute aging in  $\alpha + \beta$  phase region (700°C). It is seen that  $\alpha$  with lamellar shape was precipitated in the  $\beta$  matrix. Three types of  $\alpha$  precipitates in terms of precipitation sites appear in the microstructure, namely, grain boundaries  $\alpha$  ( $\alpha_{GB}$ ), Widmanstätten  $\alpha$  ( $\alpha_W$ ) at the vicinities of  $\beta$  grain boundaries and

intragranular  $\alpha$ . Further crystallographic analyses using EBSD orientation data demonstrate that the three types of  $\alpha$  precipitates possess the BOR with the surrounding  $\beta$  phase. These characters of  $\alpha$  in the present alloy are typical in the metastable  $\beta$  Ti alloys, such as Ti-5553 [114, 115].

As in the present work the  $\beta$  to  $\alpha$  transformation in a stress free environment is mainly explored, only the intragranular  $\alpha$  precipitates were investigated. Fig. 3.4 (a) displays the intragranular  $\alpha$  precipitates in one  $\beta$  grain. In this case, the  $\langle 1\bar{1}1 \rangle_\beta$  of the  $\beta$  grain is perpendicular to the sample surface, thus 3  $\{110\}_\beta$  planes (the BOR planes) belonging to this axis zone are on edge, as shown by the  $\{110\}_\beta$  and  $\langle 1\bar{1}1 \rangle_\beta$  pole figures in Fig. 3.4 (b). 12 BOR variants can be found in the  $\beta$  grain, as shown by the corresponding BOR plane and direction pole figures in Fig. 3.4 (b). The disorientation between any two variants from the 12 variants belongs to the classic disorientations of BOR variants, ie.  $10^\circ/\langle 0001 \rangle_\alpha$ ,  $60^\circ/\langle 11\bar{2}0 \rangle_\alpha$ ,  $60.8^\circ/\langle \bar{1}.377 \ \bar{1} \ 2.377 \ 0.359 \rangle_\alpha$ ,  $63.3^\circ/\langle \bar{1}0 \ 5 \ 5 \ \bar{3} \rangle_\alpha$  and  $90^\circ/\langle 1 \ \bar{2}.38 \ 1.38 \ 0 \rangle_\alpha$ . The habit plane of the intragranular  $\alpha$  was identified by matching the habit plane trace in the present alloy with the published habit planes and were found to be close to  $\{11 \ 11 \ 13\}_\beta$ , as shown with the  $\{11 \ \bar{1}\bar{1} \ \bar{1}3\}_\beta$  pole figure in Fig. 3.4 (c). Under such a specific  $\beta$  orientation, there are 3 variants oriented with their broad faces (the habit planes) almost parallel to the sample surface and the other variants oriented with their broad faces roughly perpendicular to the sample surface, as illustrated with the EBSD micrographs of two example  $\alpha$  plates in Fig. 3.4 (c). With the two 2D sections of the  $\alpha$  precipitates, the 3D morphology can be obtained, as illustrated in Fig. 3.4 (c). They are in plate shape, as reported in the literature, but the shape of the plate is not regular, as shown in Fig. 3.4 (a). The thickness direction of the plate is  $\langle 11 \ \bar{1}\bar{1} \ \bar{1}3 \rangle_\beta$  close to  $\langle 1\bar{1}\bar{1} \rangle_\beta$ , as shown in Fig. 3.4 (c).

Global orientation analysis of intragranular  $\alpha$  precipitates demonstrated that no variant is privileged. Every potential BOR variant has a chance to form during the transformation. However, locally the  $\alpha$  plates are organized into a triangular structure with 3 variants each forming one edge of a triangle, as outlined with the black rectangle in Fig. 3.4 (a). Such a characteristic pattern of intragranular  $\alpha$  is also typical for metastable  $\beta$  Ti alloys [116]. The 3 variants possess specific orientation relationships. They share one common  $\langle 11\bar{2}0 \rangle_\alpha$  axis that is also the BOR direction of the surrounding  $\beta$  phase and are interrelated by a  $60^\circ$  rotation



around the common  $\langle 11\bar{2}0 \rangle_\alpha$  axis, as shown in Fig. 3.4 (d). This demonstrates that locally variant selection does occur during the transformation. It has been revealed that such an organization results from the accommodation of transformation strain of one variant by the others [117, 118].

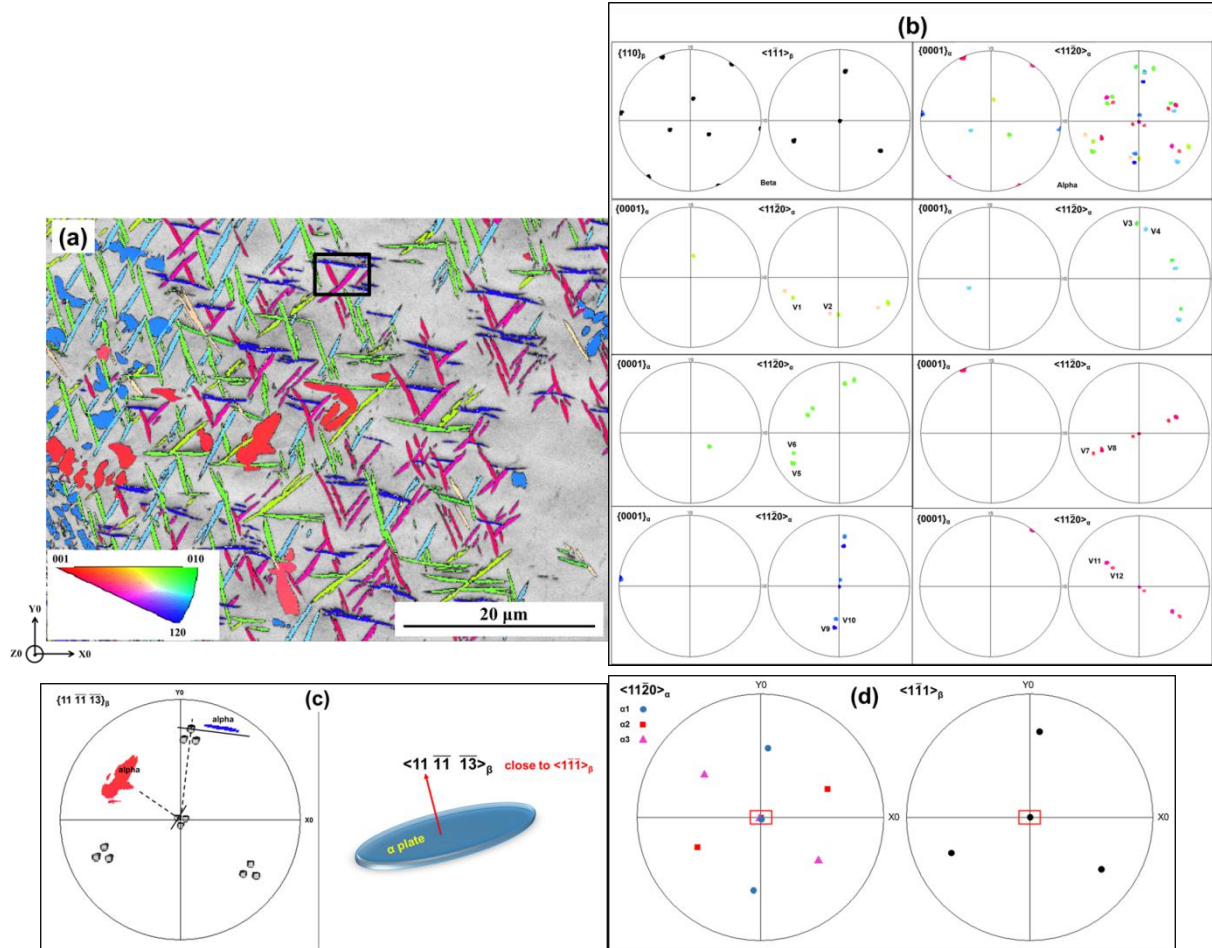


**Fig. 3.4 (a)** SEM-EBSD micrograph of intragranular  $\alpha$  precipitates of Ti-7333 alloy after solution treatment at 900°C for 30 min and aged at 700°C for 5 min. The  $\beta$  matrix is represented with its EBSD band quality contrast and the  $\alpha$  precipitates with their crystallographic orientation (expressed with the Y0 direction inverse pole figure (IPF)). The IPF color code is inserted in the figure. **(b)** Corresponding BOR direction and plane pole figures of the  $\beta$  matrix and the 12  $\alpha$  variants. The poles of the  $\alpha$  variants are represented with the consistent colors in (a). **(c)**  $\{11 \ 11 \ 13\}_\beta$  (habit plane) pole figures with two specifically oriented  $\alpha$  plates for obtaining 3D morphology of the  $\alpha$  precipitates, and their 3D illustration. **(d)** BOR direction pole figures of the 3  $\alpha$  variants forming the triangular structure and BOR direction pole figure of the parent  $\beta$ .

### 3.4.2 Sub-structures of intragranular $\alpha$ precipitates

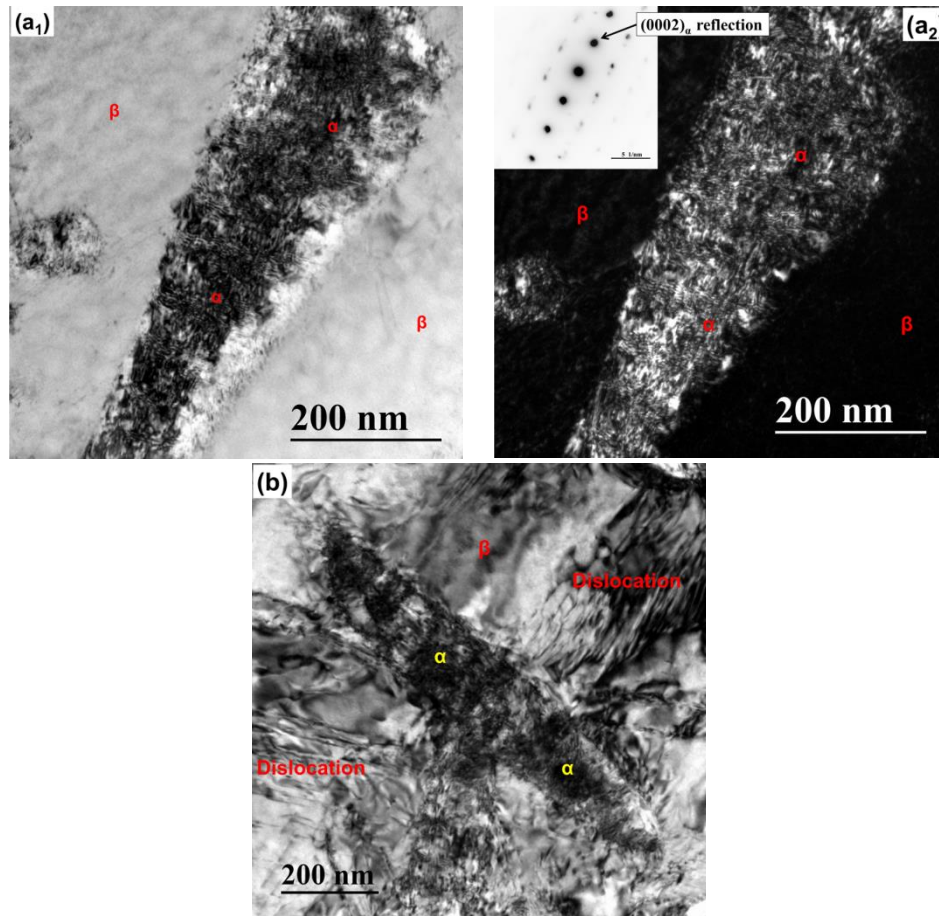


**Fig. 3.5** (a<sub>1</sub>) and (a<sub>2</sub>) TEM bright field and dark field images of  $\alpha$  plate showing differently oriented Moiré fringes arising from lattice misfits. The dark field image is obtained using the  $\alpha$  (0002) <sub>$\alpha$</sub>  reflection indicated in (a<sub>2</sub>). (b) TEM bright field image showing dislocation arrays stretching from  $\alpha/\beta$  interfaces.

To investigate the structure details within intragranular  $\alpha$  plates and their crystallographic characteristics, TEM examinations were carried out. In general, the diffraction contrast of  $\alpha$  plates is not constant with large variations, indicating that the lattice of the  $\alpha$  plates is not perfect but highly defected. However, no dislocation lines can be clearly seen within the  $\alpha$  plates by tilting the sample. In contrast, large amount of Moiré fringes can be revealed by the TEM diffraction contrast at certain sample tilts, as shown by the bright and dark field images in Fig. 3.5 (a). These fringes arise from lattice misfits in the thickness direction of the foil. The fringes are oriented in several directions. This indicates that they are either from angular

lattice misfits in a monocrystalline or from domains with different crystallographic orientations and infers that the  $\alpha$  lattice is highly strained. Furthermore, large amount of dislocation arrays are observed in the surrounding  $\beta$  matrix, as shown in Fig. 3.5 (b), indicating the existence of lattice mismatch between the two phases.

Close examinations revealed that the  $\alpha$  plates are not monocrystalline. Each plate contains two different kinds of  $\alpha$  domains with different morphologies, different crystallographic orientations and at different sites with respect to the host  $\alpha$  plate. Hereafter we refer the host  $\alpha$  plate as major  $\alpha$ .

The first kind of  $\alpha$  domains are in particle shape with sizes of about 20 nm and situated at the surface of the major  $\alpha$  plate, as shown in Fig. 3.6 (a) and (b) where the  $\alpha$  plates are presented with their broad faces oriented in two specific orientations, one being parallel to the TEM screen and the other perpendicular to the screen. These two specific orientations of the major  $\alpha$  plate allow resolving the 3D morphology of the  $\alpha$  domains and their sites and sizes. We denote such  $\alpha$  domains interface  $\alpha$ . Further crystallographic orientation analyses using Selected Area Electron Diffraction (SAED) pattern of all the  $\alpha$  domains attached to one major  $\alpha$  plate, as shown in Fig. 3.7 (a), revealed that these  $\alpha$  domains possess one crystallographic orientation, as shown by the SAED pattern in Fig. 3.7 (a). The orientation relationships between the interface  $\alpha$  and the  $\beta$  matrix and the major  $\alpha$  are further calculated using their orientations determined by indexing the acquired Kikuchi line patterns, as shown in Fig. 3.7 (b). Results show that these domains possess the BOR with the adjacent  $\beta$  matrix and are related with the major  $\alpha$  plate by a  $60^\circ$  rotation around the  $\langle 11\bar{2}0 \rangle_\alpha$  axis, as shown by the pole figures in Fig. 3.7 (c). The interface  $\alpha$  has the same orientation as that of one neighboring major  $\alpha$  plate that forms the triangular structure. Such kind of  $\alpha$  domains has been theoretically predicted by the 3D phase field simulations, using Ti-6Al-4V [34]. According to [34], their formation is induced by the stress field of the major  $\alpha$  plate. The present results offer an experimental evidence for the simulated result. It should be noted that the materials used in [34] and in the present work are different in composition, however, the characteristics concerning the interface  $\alpha$  domains are the same. This infers that the formation of such  $\alpha$  domains is a common feature of Al containing metastable  $\beta$  Ti alloys.

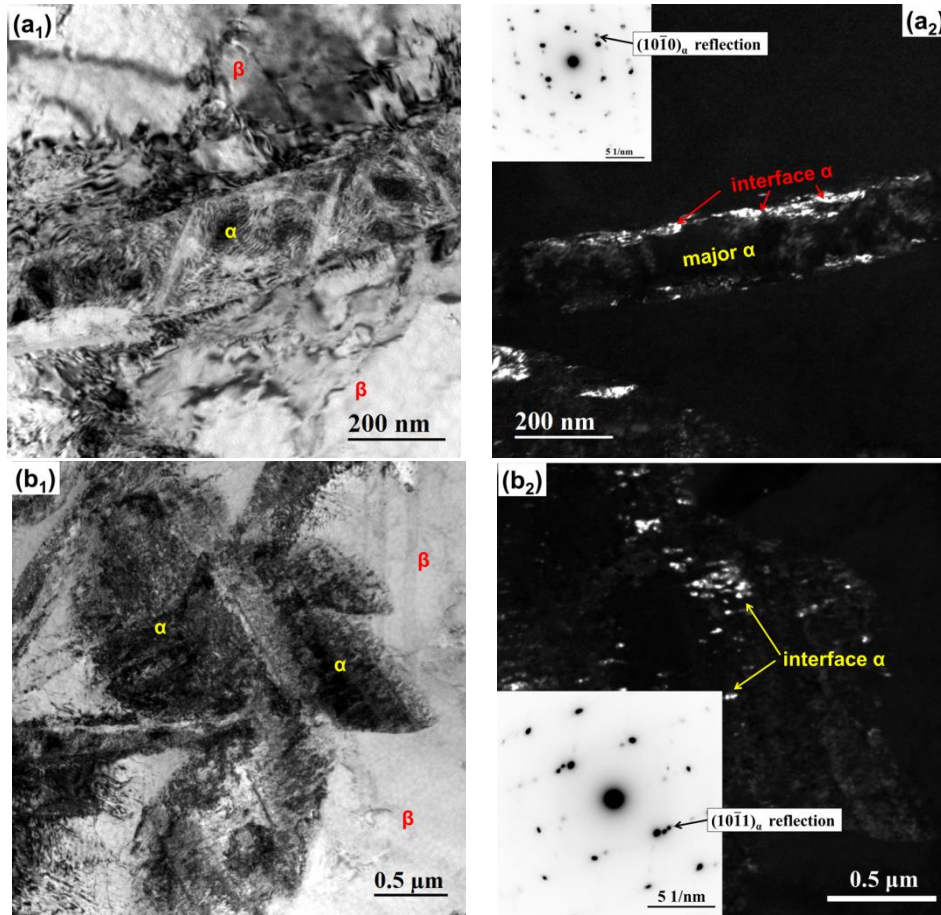


**Fig.3.6** TEM bright and dark field images of two differently oriented major  $\alpha$  plates showing the  $\alpha$  domains situated on the surface of these plates. (a<sub>1</sub>) and (a<sub>2</sub>) the major  $\alpha$  plate is with its habit plane perpendicular to the TEM screen. The dark field image is obtained using the  $(10\bar{1}0)_\alpha$  reflection indicated in (a<sub>2</sub>). (b<sub>1</sub>) and (b<sub>2</sub>) the major  $\alpha$  plate is with its habit plane parallel to the TEM screen. The dark field image is obtained using the  $(10\bar{1}1)_\alpha$  reflection indicated in (b<sub>2</sub>).



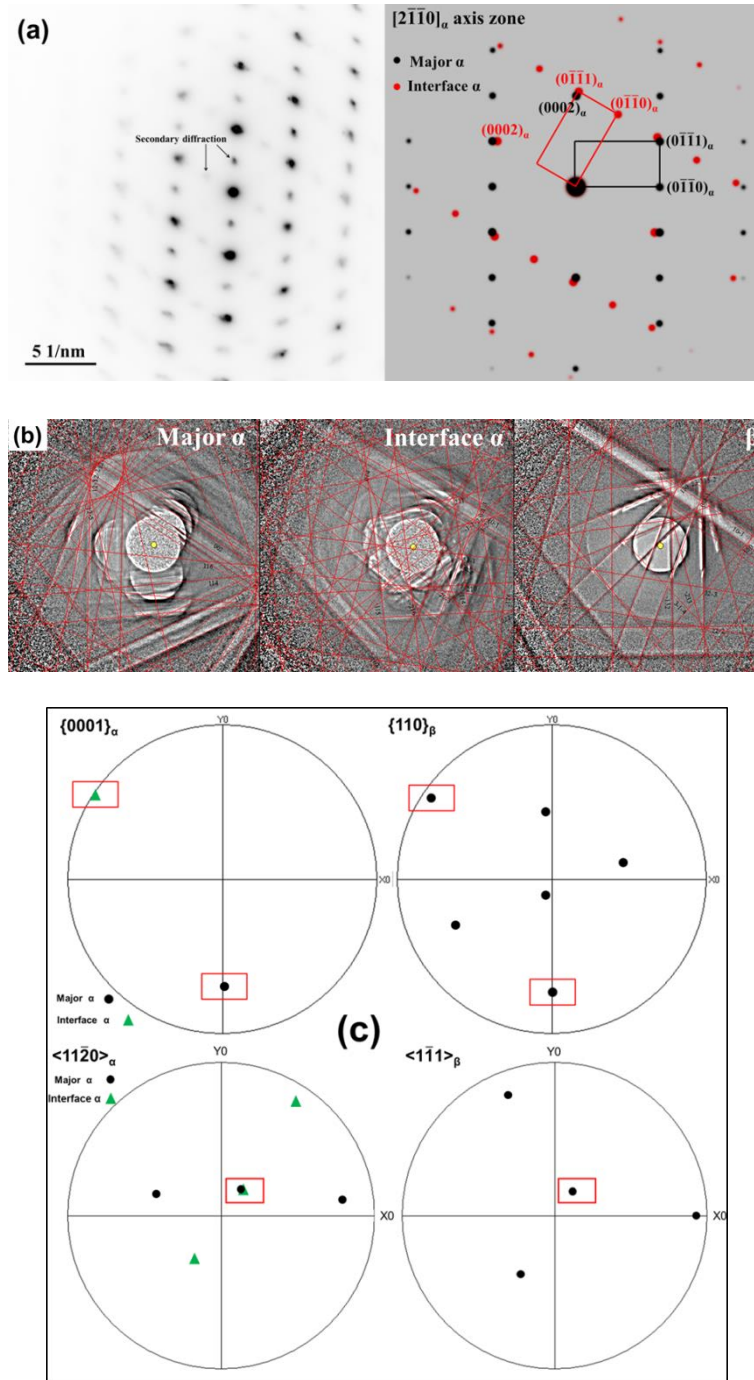


**Fig. 3.7** (a) Selected Area Electron Diffraction (SAED) pattern of the interface  $\alpha$  domains attached to one major  $\alpha$  plate and the corresponding SAED pattern simulated using the Crystal Maker software. (b) TEM Kikuchi line patterns from the major  $\alpha$  plate, its interface  $\alpha$  domains and the surrounding  $\beta$  matrix. The red lines are the simulated Kikuchi lines using EP. (c) BOR plane and direction pole figures of the major  $\alpha$  plate, the interface  $\alpha$  domains and the surrounding  $\beta$  matrix. The common directions shared by the major  $\alpha$ , the interface  $\alpha$  and  $\beta$  matrix are outlined with the red rectangles

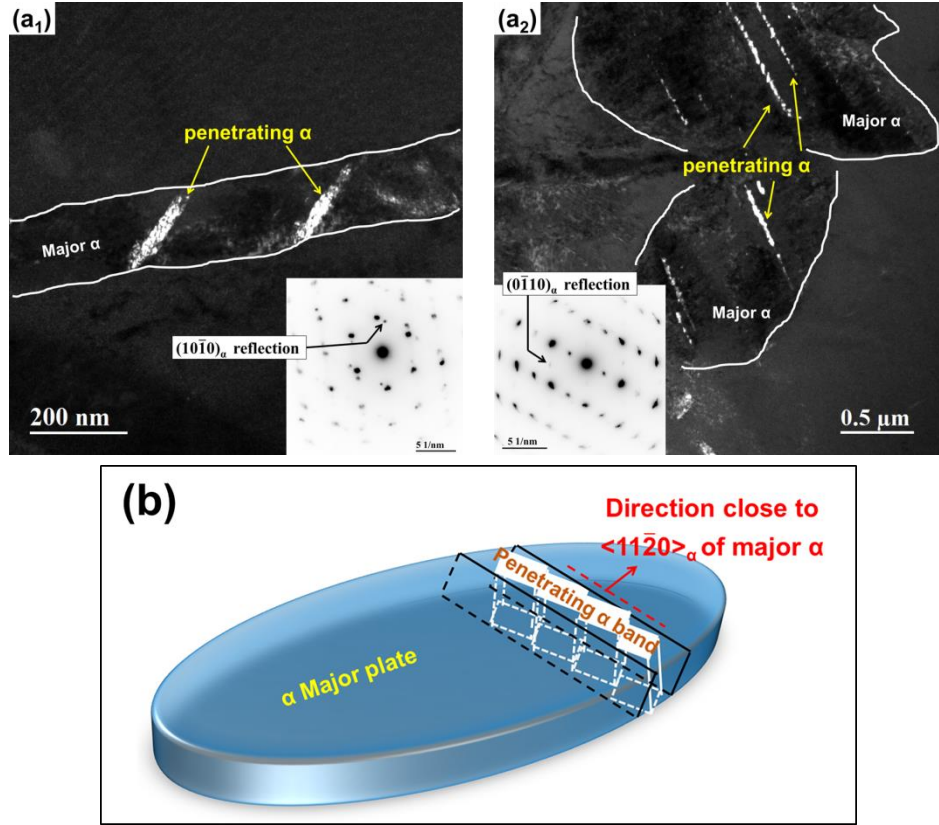


**Fig. 3.8** TEM dark field images of two differently oriented major  $\alpha$  plates showing the penetrating  $\alpha$  domains in the major  $\alpha$  plate and the illustration of the band of the penetrating  $\alpha$  domains. (a<sub>1</sub>) and (a<sub>2</sub>) the major  $\alpha$  plate is with its habit plane perpendicular and parallel to the TEM screen. The dark field image is obtained using the (10 $\bar{1}$ 0) <sub>$\alpha$</sub>  and the (0 $\bar{1}$ 10) <sub>$\alpha$</sub>  reflection, respectively. (b) Illustration of the band of penetrating  $\alpha$  band in the major  $\alpha$  plate.

The second type of  $\alpha$  domains are in plate shape with a thickness of about 20 nm and run through the major  $\alpha$  plates, as shown in Fig. 3.8 (a<sub>1</sub>). We denote such  $\alpha$  domains penetrating  $\alpha$ . Different from the interface  $\alpha$ , the penetrating  $\alpha$  lamellae are organized in parallel bands and the bands are repeated regularly, as seen in Fig. 3.8 (a<sub>2</sub>). In each band, the penetrating  $\alpha$  domains are aligned and spaced regularly, as illustrated in Fig. 3.8 (b). Further orientation analysis using the SAED and the Kikuchi pattern of the penetrating  $\alpha$  domains, the major  $\alpha$  plate and the  $\beta$  matrix revealed that the broad face of the bands are roughly normal to the  $\langle 11\bar{2}0 \rangle_\alpha$  of the major  $\alpha$  plate or the  $\langle \bar{1}1\bar{1} \rangle$  of the  $\beta$  matrix, as illustrated in Fig. 3.8 (b). Analysis with the SAED patterns obtained from the penetrating  $\alpha$  domains within one major  $\alpha$  plate demonstrated that they possess the same orientation, as shown by the SAED patterns in

Fig. 3.9 (a). Calculations using the orientations determined from the Kikuchi patterns of the penetrating  $\alpha$ , the major  $\alpha$  and the surrounding  $\beta$  matrix, as shown in Fig. 3.9 (b), showed that the penetrating  $\alpha$  is related to the major  $\alpha$  by a  $60^\circ$  around the  $\langle 11\bar{2}0 \rangle_\alpha$  axis but it does not obey the BOR with the  $\beta$  matrix, as shown with the pole figures in Fig. 3.9 (c). Such  $\alpha$  domains have not been reported in the literature, thus the origin of their formation is not yet known.

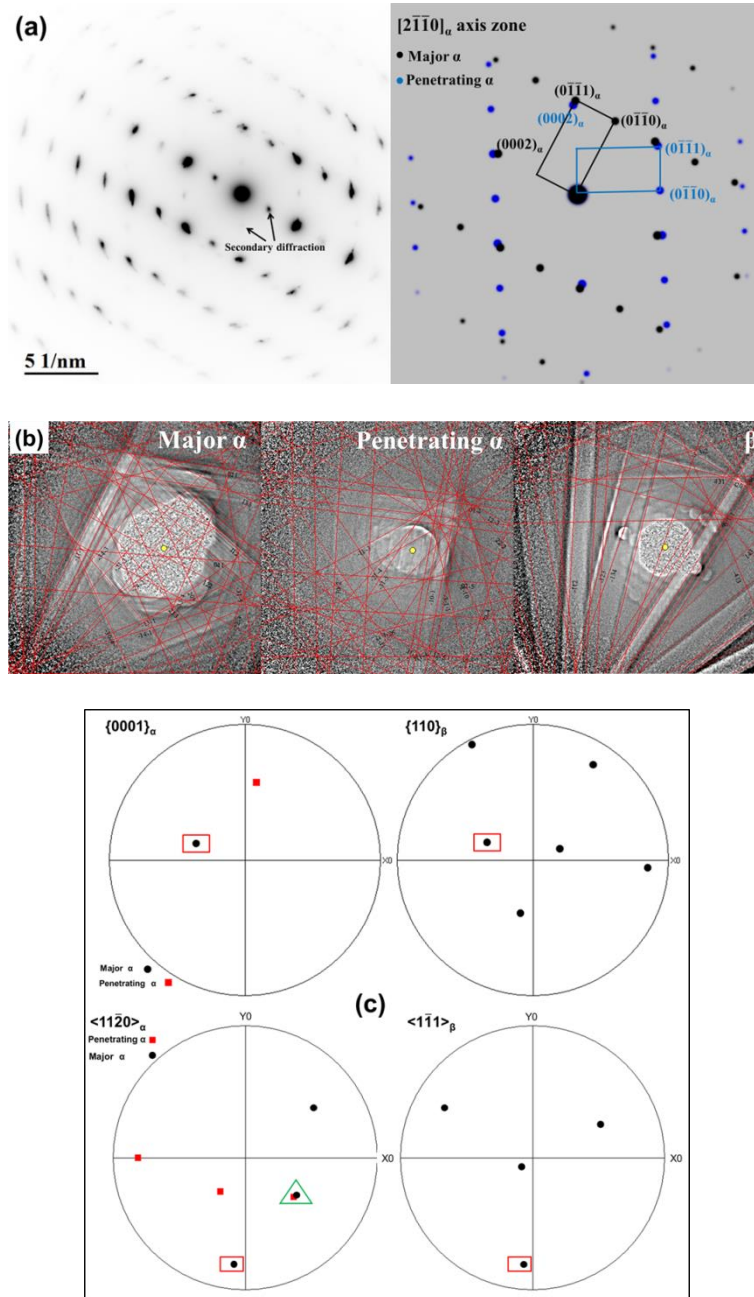


**Fig. 3.9 (a)** Selected Area Electron Diffraction (SAED) pattern of the penetrating  $\alpha$  domains attached to one major  $\alpha$  plate and the corresponding SAED pattern simulated using the

Crystal Maker software. **(b)** TEM Kikuchi line patterns from the major  $\alpha$  plate, the penetrating  $\alpha$  domains and the surrounding  $\beta$  matrix. The red lines are the simulated Kikuchi lines using EP. **(c)** BOR plane and direction pole figures of the major  $\alpha$  plate, the penetrating  $\alpha$  domains and the surrounding  $\beta$  matrix. The common directions shared by the major  $\alpha$  and the penetrating  $\alpha$  are outlined with the green triangle, and the common plane and direction shared by the major  $\alpha$  plate and the  $\beta$  matrix are outlined with the red rectangles.

For the  $\beta$  matrix around each major  $\alpha$  plate, large amount of dislocations are present. The dislocations are organized in parallel arrays, as shown in Fig. 3.10. The lines stretch from the  $\alpha/\beta$  interfaces to the interior of the  $\beta$  matrix. Further analysis using the determination method in [119] demonstrated that they are mainly  $\langle 1\bar{1}1 \rangle \{110\}_\beta$  edge dislocations that are typical of BCC metals.

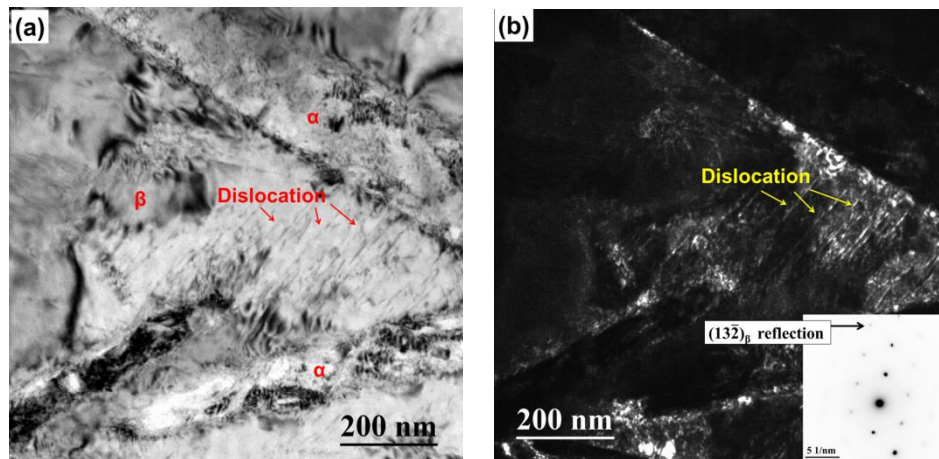


**Fig. 3.10** (a) and (b) TEM bright field and dark field images showing dislocation arrays in  $\beta$  stretching from the  $\alpha/\beta$  interface. The dark field image is obtained using the  $(13\bar{2})_\beta$  reflection as indicated in the figure.



### 3.5 Formation mechanisms of sub-structures of intragranular $\alpha$ precipitates

#### 3.5.1 Phase transformation lattice strain characters

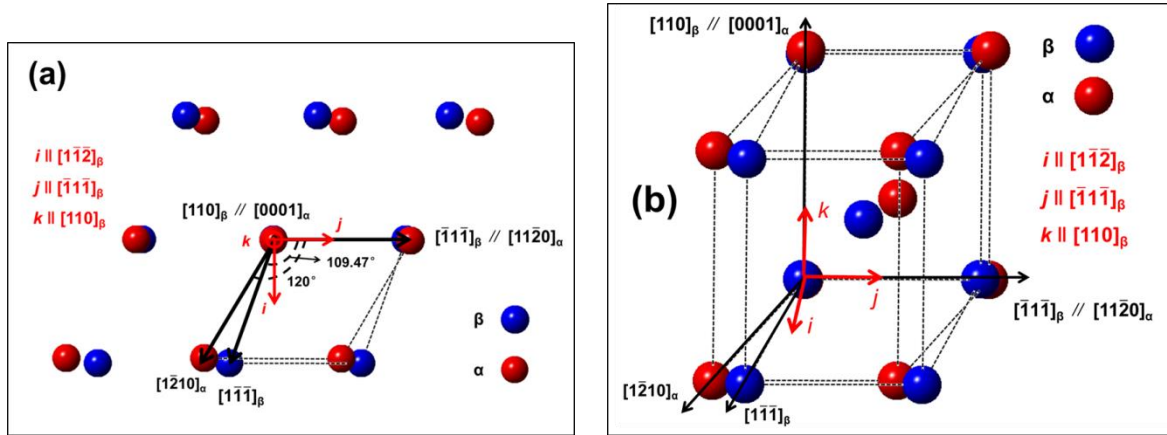


**Fig. 3.11** (a) Atomic correspondences between  $\beta$  phase and  $\alpha$  phase on the BOR plane and the reference frame ( $i-j-k$ ) under the BOR, i.e.,  $j$  is parallel to the OR directions in the two phases,  $k$  to the direction normal to the OR planes in the two phases and  $i$  is the vector cross product of  $k$  and  $j$ . (b) 3D atomic correspondences between  $\beta$  phase and  $\alpha$  phase in the  $i-j-k$  reference frame.

For the  $\beta$  to  $\alpha$  transformation in Ti alloys, in addition to the diffusion process, it evolves a structure change from the BCC to HCP system through lattice deformation, like the case of martensitic transformation. By examining the atomic correspondences between the two phases, the deformation gradient tensor for the structure transformation in the stress free condition can be obtained. For the present transformation, the BOR is obeyed by the two phases, thus the deformation gradient tensor  $A$   $[120]$  expressed in the frame of the BOR, as shown in Fig. 3.11, can be established. As displayed in Eq. (1),  $\varepsilon_{ii}$  ( $i=1, 2$  and  $3$ ), the diagonal elements, means elongation ( $\varepsilon_{ii}>1$ ) or contraction ( $\varepsilon_{ii}<1$ ) in the  $i$  direction, whereas  $\varepsilon_{ij}$  ( $i$  and  $j=1, 2$  and  $3$ ), the off diagonal elements, means a shear in the direction of  $i$  and on the plane normal to  $j$ . The normal strain is accumulative in  $i$ , whereas the shear amount is proportional to the dimension in the direction normal to the shear plane, i.e. in  $j$ . This means that the

normal strain restricts the growth of the new phase in the strain direction, whereas the shear strain confines the growth of the new phase in the direction normal to the shear plane.

$$A = \begin{pmatrix} \varepsilon_{11} & \varepsilon_{12} & \varepsilon_{13} \\ \varepsilon_{21} & \varepsilon_{22} & \varepsilon_{23} \\ \varepsilon_{31} & \varepsilon_{32} & \varepsilon_{33} \end{pmatrix} \quad (3.1)$$

For the present alloy, the deformation gradient tensor of the variant satisfying  $(110)_\beta // (0001)_\alpha$  and  $[\bar{1}1\bar{1}]_\beta // [11\bar{2}0]_\alpha$  is given in Table 3.1 in the BOR reference frame (as shown in Fig. 3.11). It is seen that the formation of this variant requires a contraction of 0.0416 in the  $[1\bar{1}\bar{2}]_\beta$  direction ( $\varepsilon_{11}$ ), an elongation of 0.0434 in the  $[\bar{1}1\bar{1}]_\beta$  direction  $\varepsilon_{22}$ , an elongation of 0.0189 in the  $[110]_\beta$  direction  $\varepsilon_{33}$  and a shear of 0.1844 on the  $(1\bar{1}\bar{2})_\beta$  plane and in the  $[\bar{1}1\bar{1}]_\beta$  direction  $\varepsilon_{21}$ , as summarized in Table 3.2. It is seen that the most important strain is the shear on the plane of  $(1\bar{1}\bar{2})_\beta$  and in the  $[\bar{1}1\bar{1}]_\beta$  direction that is more than 3 times higher than that of the contraction in the  $[1\bar{1}\bar{2}]_\beta$  direction and the elongation in the  $[\bar{1}1\bar{1}]_\beta$  direction and almost one order higher than the elongation in the  $[110]_\beta$  direction.

**Table 3.1** Deformation gradient tensor of the variant expressed in its BOR reference frame

$((110)_\beta // (0001)_\alpha \text{ and } [\bar{1}1\bar{1}]_\beta // [11\bar{2}0]_\alpha)$	
Variant	Deformation gradient tensor
$(110)_\beta // (0001)_\alpha$ $[\bar{1}1\bar{1}]_\beta // [11\bar{2}0]_\alpha$	$\begin{pmatrix} -0.0416 & 0 & 0 \\ -0.1844 & 0.0434 & 0 \\ 0 & 0 & 0.0189 \end{pmatrix}$

**Table 3.2** Strain components of the transformation deformation

Deformation	Strain
Dilation $[1\bar{1}\bar{2}]_\beta$	0.0416
Dilation $[\bar{1}1\bar{1}]_\beta$	0.0434
Dilation $[110]_\beta$	0.0189
Shear $(1\bar{1}\bar{2})_\beta$ $[\bar{1}1\bar{1}]_\beta$	0.1844

Such a deformation characterized by a large shear strain well explains the plate shape of the major  $\alpha$ . One can find that the orientation of the plane of the  $[\bar{1}1\bar{1}]_\beta / (1\bar{1}\bar{2})_\beta$  shear ( $\varepsilon_{21}$ ) is close to that of the habit plane  $(11\bar{1}\bar{1}\bar{3})_\beta$  (with an angular deviation of about  $15^\circ$ ) that is

also the broad face of the  $\alpha$  phase. Thus this shear restricts the thickening of the  $\alpha$  precipitate in the direction perpendicular to the habit plane during the growth process. Moreover, the normal strain component  $\varepsilon_{11}$  also restricts the growth of the  $\alpha$  precipitate in this direction. Finally, the precipitated  $\alpha$  develops into plate shape. The dimension of the  $\alpha$  precipitates in the direction normal to the  $(11\ \bar{1}\bar{1}\ \bar{1}\bar{3})_\beta$  is indeed the smallest, as is evidenced for the major  $\alpha$  plates in the present alloy.

### 3.5.2 Formation mechanism of interface $\alpha$ and local variant selection of major $\alpha$

With the determined orientation of the interface  $\alpha$  with respect to the major  $\alpha$  plate ( $60^\circ/\langle 11\bar{2}0 \rangle_\alpha$ ) and the surrounding  $\beta$  matrix (BOR), the deformation gradient tensors of such  $\alpha$  variants were calculated and expressed in the BOR frame of the major  $\alpha$  plate. The tensors are displayed in Table 3.3. For reference, the deformation gradient tensors of the other BOR variants were also calculated in the frame of the major  $\alpha$  plate and displayed in Table 3.3. It is seen that among all the 11 possible BOR  $\alpha$  variants, only V1 and V2 that are related with the major  $\alpha$  plate by a  $60^\circ/\langle 11\bar{2}0 \rangle_\alpha$  rotation have the highest positive  $\varepsilon_{21}$ . That means that these variants have the highest accommodation capacity for the shear deformation generated by the major  $\alpha$  variant. In addition, the  $\varepsilon_{11}$  of these variants is larger than 1 (elongation), thus they can well accommodate the lattice contraction of the major  $\alpha$  plate in this direction ( $\varepsilon_{11}$  of the major  $\alpha$  plate is smaller than 1). As analyzed above, for these two components ( $\varepsilon_{21}$  and  $\varepsilon_{11}$ ), the highest deformation happens at the surface of the major  $\alpha$  plate. This is the exact place where are the interface  $\alpha$  domains in the present alloy. Thus the formation of the interface  $\alpha$  domains is indeed induced by the local deformation generated by the major  $\alpha$  plate. Moreover, the values of  $\varepsilon_{i2}$  of the two variants (V1 and V2) (Table 3.3) are exactly the same as those of the major  $\alpha$  plate (Table 3.1), meaning that the growth of the interface  $\alpha$  in the direction of  $[\bar{1}\bar{1}\bar{1}]_\beta$  is totally compatible with the major  $\alpha$  plate. However, the values of  $\varepsilon_{i3}$  of the interface  $\alpha$  are quite different from the corresponding values of the  $\varepsilon_{i3}$  of the major  $\alpha$ , thus the growths of the two kinds of  $\alpha$  in the direction of  $[110]_\beta$  are not compatible. This may be one of the reasons that the interface  $\alpha$  domains are in particle shape. Another reason may be the

incompatible interface between the two  $\alpha$ .

**Table 3.3** Deformation gradient tensors of the other 11 possible BOR  $\alpha$  variants expressed in the BOR frame of the major  $\alpha$  plate in **Table 3.1** and the disorientation with it

No.	Variant	Deformation gradient tensor	Disorientation
V1	$(10\bar{1})_{\beta}/(0001)_{\alpha}$ $[111]_{\beta}/[11\bar{2}0]_{\alpha}$	$\begin{pmatrix} 1.0038 & 0 & 0.0262 \\ 0.0922 & 1.0434 & -0.1597 \\ 0.0262 & 0 & 0.9735 \end{pmatrix}$	$60^{\circ}/\langle 11\bar{2}0 \rangle$
V2	$(01\bar{1})_{\beta}/(0001)_{\alpha}$ $[1\bar{1}\bar{1}]_{\beta}/[11\bar{2}0]_{\alpha}$	$\begin{pmatrix} 1.0038 & 0 & -0.0262 \\ 0.0922 & 1.0434 & 0.1597 \\ -0.0262 & 0 & 0.9735 \end{pmatrix}$	$60^{\circ}/\langle 11\bar{2}0 \rangle$
V3	$(101)_{\beta}/(0001)_{\alpha}$ $[1\bar{1}\bar{1}]_{\beta}/[11\bar{2}0]_{\alpha}$	$\begin{pmatrix} 1.0680 & 0.0695 & 0.1419 \\ -0.0277 & 0.9792 & -0.0780 \\ -0.0087 & -0.0247 & 0.9735 \end{pmatrix}$	$60.832^{\circ}/\langle \bar{1}377 \bar{1} 2.377 \rangle$ $0.359^{\circ}$
V4	$(\bar{1}01)_{\beta}/(0001)_{\alpha}$ $[\bar{1}1\bar{1}]_{\beta}/[11\bar{2}0]_{\alpha}$	$\begin{pmatrix} 1.0548 & -0.0134 & -0.0011 \\ 0.0789 & 0.9792 & -0.0193 \\ 0.1495 & -0.0726 & 0.9867 \end{pmatrix}$	$63.2618^{\circ}/\langle \bar{1}0 5 5 \bar{3} \rangle$
V5	$(\bar{1}0\bar{1})_{\beta}/(0001)_{\alpha}$ $[\bar{1}\bar{1}1]_{\beta}/[11\bar{2}0]_{\alpha}$	$\begin{pmatrix} 1.0082 & 0.0953 & 0.0186 \\ 0.0031 & 1.0258 & -0.0054 \\ 0.0186 & -0.1651 & 0.9867 \end{pmatrix}$	$60.832^{\circ}/\langle \bar{1}377 \bar{1} 2.377 \rangle$ $0.359^{\circ}$
V6	$(101)_{\beta}/(0001)_{\alpha}$ $[\bar{1}11]_{\beta}/[11\bar{2}0]_{\alpha}$	$\begin{pmatrix} 0.9395 & -0.0562 & -0.0829 \\ -0.0562 & 0.9792 & -0.0586 \\ 0.0677 & 0.0479 & 1.1020 \end{pmatrix}$	$90^{\circ}/\langle 1 \bar{2}38 1.38 0 \rangle$
V7	$(\bar{1}10)_{\beta}/(0001)_{\alpha}$ $[\bar{1}\bar{1}\bar{1}]_{\beta}/[11\bar{2}0]_{\alpha}$	$\begin{pmatrix} 1.0680 & 0.0695 & -0.1419 \\ -0.0277 & 0.9792 & 0.0780 \\ 0.0087 & 0.0247 & 0.9735 \end{pmatrix}$	$60.832^{\circ}/\langle \bar{1}377 \bar{1} 2.377 \rangle$ $0.359^{\circ}$
V8	$(\bar{1}0\bar{1})_{\beta}/(0001)_{\alpha}$ $[11\bar{1}]_{\beta}/[11\bar{2}0]_{\alpha}$	$\begin{pmatrix} 1.0082 & 0.0953 & -0.0186 \\ 0.0031 & 1.0258 & 0.0054 \\ -0.0186 & 0.1651 & 0.9867 \end{pmatrix}$	$10.5288^{\circ}/\langle 0001 \rangle$
V9	$(011)_{\beta}/(0001)_{\alpha}$ $[\bar{1}\bar{1}1]_{\beta}/[11\bar{2}0]_{\alpha}$	$\begin{pmatrix} 1.0082 & 0.0953 & -0.0186 \\ 0.0031 & 1.0258 & 0.0054 \\ -0.0186 & -0.1651 & 0.9867 \end{pmatrix}$	$60.832^{\circ}/\langle \bar{1}377 \bar{1} 2.377 \rangle$ $0.359^{\circ}$
V10	$(0\bar{1}\bar{1})_{\beta}/(0001)_{\alpha}$ $[\bar{1}1\bar{1}]_{\beta}/[11\bar{2}0]_{\alpha}$	$\begin{pmatrix} 1.0548 & -0.0134 & 0.0011 \\ 0.0789 & 0.9792 & 0.0193 \\ -0.1495 & 0.0726 & 0.9867 \end{pmatrix}$	$63.2618^{\circ}/\langle \bar{1}0 5 5 \bar{3} \rangle$
V11	$(\bar{1}10)_{\beta}/(0001)_{\alpha}$ $[111]_{\beta}/[11\bar{2}0]_{\alpha}$	$\begin{pmatrix} 0.9395 & -0.0562 & 0.0829 \\ -0.0562 & 0.9792 & 0.0586 \\ -0.0677 & -0.0479 & 1.1020 \end{pmatrix}$	$90^{\circ}/\langle 1 \bar{2}38 1.38 0 \rangle$

From Table 3.3 one can find that variants V4 and V10 also possess accommodation capacity to the shear deformation generated by the major  $\alpha$  plate (the  $\varepsilon_{2I}$  is positive and the

second largest among the 11 variants). The appearance of these variants has been predicted by the theoretical simulation [34]. However, in the present work, we did not find their existence. This may be due to their poor geometrical compatibility with the major  $\alpha$  plate in the directions of  $[\bar{1}\bar{1}\bar{1}]_\beta$  and  $[110]_\beta$ . It is seen from Table 3.3 that their values of  $\varepsilon_{2i}$  and  $\varepsilon_{3i}$  are very different from those of the corresponding  $\varepsilon_{2i}$  and  $\varepsilon_{3i}$  of the major  $\alpha$ , especially  $\varepsilon_{22}$ . The  $\varepsilon_{22}$  of V4 and V10 are smaller than 1, meaning contraction, whereas that of the major  $\alpha$  plate is larger than 1, meaning elongation. Thus in the direction of  $[\bar{1}\bar{1}\bar{1}]_\beta$ , the growth of the two  $\alpha$  is totally incompatible. Therefore, compared with variants V1 and V2, variants V4 and V10 are less favorable. They may form under very specific local strain conditions but their occurrence is certainly minor. This corresponds to our experimental observation.

It should be noted from Table 3.3 that the formation of the interface  $\alpha$  can only accommodate one part of the shear strain at the broad faces of the major  $\alpha$  plate. Moreover it also generates a relative large shear  $\varepsilon_{23}$  (-0.1597). Thus the remaining part of the shear  $\varepsilon_{21}$  from the major  $\alpha$  plate and the newly created shear  $\varepsilon_{23}$  from the interface  $\alpha$  should be accommodated by other mechanical systems of either the major  $\alpha$  plate or the surrounding  $\beta$  matrix. Further analysis shows that the shear system of  $\varepsilon_{21}$  is in coincidence with the  $\{\bar{1}12\} \langle 1\bar{1}1 \rangle_\beta$  slip system of the surrounding  $\beta$  matrix. This slip system is also in geometrical consistent with one of the prismatic slip  $\{0002\} \langle 11\bar{2}0 \rangle_\alpha$  of the major  $\alpha$  plate. The shear system of  $\varepsilon_{23}$  is in coincidence with the  $\{110\} \langle 1\bar{1}1 \rangle_\beta$  slip system. Our TEM examination on dislocations in  $\beta$  matrix did not reveal the existence of  $\{\bar{1}12\} \langle 1\bar{1}1 \rangle_\beta$  type dislocations in the  $\beta$  matrix near the major  $\alpha$  plate. However, large amount of Moiré fringes were observed in the major  $\alpha$  plate, as shown in Fig. 3.5 (a), indicating the shear of  $\varepsilon_{21}$  of the major  $\alpha$  plate may be absorbed mainly by its prismatic slip  $[121, 122]$ , as it is well known that the prismatic slip of the  $\alpha$  phase of the Ti has very small critical resolved shear stress (CRSS) [123, 124]. The activation of the prismatic slip may be much easier than the activation of the  $\{\bar{1}12\} \langle 1\bar{1}1 \rangle_\beta$  slip of the  $\beta$  phase. For the shear of  $\varepsilon_{23}$ , the TEM examination did evidence the existence of  $\{110\} \langle 1\bar{1}1 \rangle_\beta$  dislocations in the form of arrays stretching from the interface of the major  $\alpha$  plate to the interior of the surrounding  $\beta$  matrix, as shown in Fig. 3.10. This indicates that the relative large value of the  $\varepsilon_{23}$  resulting from the formation of the interface  $\alpha$  particles should be accommodated by the formation of the  $\{110\} \langle 1\bar{1}1 \rangle_\beta$  dislocations in the nearby  $\beta$  matrix.

Obviously the interface  $\alpha$  particles further serve as sympathetic nuclei for the formation of the neighboring major  $\alpha$  plate with the same orientation and eventually contribute to formation of the triangular variant cluster of the three  $60^\circ/\langle 11\bar{2}0 \rangle_\alpha$  inter-related major  $\alpha$  plates, as shown in Fig. 3.4 (a). Thus the formation of each triangular variant cluster is to minimize the shear strain generated by the major  $\alpha$  plates in the cluster. Moreover, by obeying the BOR, the low CRSS shear systems of the major  $\alpha$  plates (the prismatic slip) and the  $\beta$  matrix ( $\{110\} \langle 1\bar{1}1 \rangle_\beta$ ) are in perfect geometrical consistency with the lattice deformation components of the structure transformation. The transformation strains can be further accommodated by the activation of these compatible systems, thus the formation of the triangular clusters is energetically favorable in terms of minimizing the overall transformation strain.

### 3.5.3 Formation mechanism of non BOR $\alpha$ domains

The above analysis shows that by forming the interface  $\alpha$  and the triangular  $\alpha$  cluster, the shear deformation created by the displacive structure transformation from the  $\beta$  phase to the major  $\alpha$  plates can be well accommodated. However, the normal strain, especially  $\varepsilon_{22}$  (Table 3.1), of each major  $\alpha$  plate is not accommodated. This strain becomes un-ignorable when the major  $\alpha$  plate enlarges its dimension in the  $[\bar{1}1\bar{1}]_\beta$  direction. From Table 3.1 one can see that the value of  $\varepsilon_{22}$  of the major  $\alpha$  plate is larger than 1, meaning that the  $\beta$  lattice extends in the  $[\bar{1}1\bar{1}]_\beta$  direction when it transforms to the  $\alpha$  lattice and the remaining  $\beta$  lattice in the transformation front is contracted. The contraction accumulated with the growth of the major  $\alpha$  plate in this direction. Thus the accommodation to release the constraint is needed. The formation of the penetrating  $\alpha$  bands that go through and are with their broad faces normal to the  $[\bar{1}1\bar{1}]_\beta$  direction, as shown in Fig. 3.8 (a) and (b) should be related to such a need.

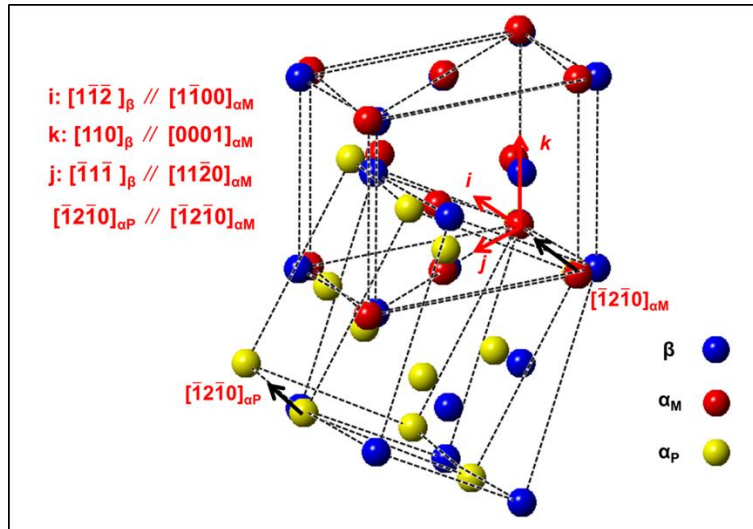


**Fig. 3.12** Atomic correspondences between the  $\beta$  phase, the major  $\alpha$  plate and the penetrating  $\alpha$  under the BOR between the  $\beta$  phase and the major  $\alpha$  plate  $(110)_{\beta} // (0001)_{\alpha} - [\bar{1}\bar{1}\bar{1}]_{\beta} // [11\bar{2}0]_{\alpha}$ , and the  $60^{\circ} / [\bar{1}2\bar{1}0]_{\alpha}$  rotation between the major  $\alpha$  and the penetrating  $\alpha$ .

Thus, the deformation gradient tensor of the penetrating  $\alpha$  was established and is expressed in the same BOR reference frame as their host major  $\alpha$  plate. With the determined BOR between the  $\beta$  matrix and the major  $\alpha$  ( $(110)_{\beta} // (0001)_{\alpha}$  and  $[\bar{1}\bar{1}\bar{1}]_{\beta} // [11\bar{2}0]_{\alpha}$ ) and the  $60^{\circ} / [\bar{1}2\bar{1}0]_{\alpha}$  rotation between the major  $\alpha$  and the penetrating  $\alpha$ , as shown by the pole figure in Fig. 3.9 (c), the atomic correspondences between the  $\beta$  matrix and the penetrating  $\alpha$  were established, as shown in Fig. 3.12. As seen from the figures, no plane and in-plane direction parallelisms between the  $\beta$  phase and the penetrating  $\alpha$  can be figured out. This further demonstrates that the penetrating  $\alpha$  is transformed from the deformed  $\beta$ . By examining the atomic correspondences between the  $\beta$  and the penetrating  $\alpha$  via the major  $\alpha$ , the lattice deformation with the smallest atomic movements was worked out and thus the deformation gradient tensor for the structure transformation of the  $\beta$  matrix to the penetrating  $\alpha$  plates expressed in the same BOR reference frame as for the major  $\alpha$  plate was obtained. The tensor is given in Table 3.4. It is seen that the formation of the penetrating  $\alpha$  domains ( $\varepsilon_{22}=0.8675$ ) indeed accommodates the normal strain in the  $[\bar{1}\bar{1}\bar{1}]_{\beta}$  direction produced by the major  $\alpha$  plate ( $\varepsilon_{22}=1.0434$ ). Moreover, the  $\varepsilon_{11}$  ( $0.8984 < 1$ ; contraction) and the  $\varepsilon_{21}$  ( $-0.286$ ; negative) of the penetrating  $\alpha$  demonstrate similar characters to the  $\varepsilon_{11}$  ( $0.9584 < 1$ ; contraction) and the  $\varepsilon_{21}$  ( $-0.1844$ ; negative) of the major  $\alpha$  plate, i.e., contraction in the  $[\bar{1}\bar{1}\bar{2}]_{\beta}$  direction and shear on

$(1\bar{1}\bar{2})_\beta$  plane along the  $[\bar{1}\bar{1}\bar{1}]_\beta$  direction. Thus in the  $[1\bar{1}\bar{2}]_\beta$  direction, the growths of the two  $\alpha$  are rather compatible than accommodative. This corresponds well to the going-through feature of the penetrating  $\alpha$  in the major  $\alpha$  plate, as these strains produce maximum deformations at the broad face of the major  $\alpha$  plate but not in the volume. However, it should be noted that the formation of the penetrating  $\alpha$  also creates relative large shears on the  $(1\bar{1}\bar{2})_\beta$  plane in the  $[110]_\beta$  direction ( $\varepsilon_{31}$ ), and on the  $(\bar{1}\bar{1}\bar{1})_\beta$  plane in the  $[110]_\beta$  direction ( $\varepsilon_{32}$ ), especially the latter. However, for  $\varepsilon_{31}$  and  $\varepsilon_{32}$ , there are no slip systems or twinning systems in either  $\beta$  matrix or the major  $\alpha$  to accommodate these two shears. Thus the width of the penetrating  $\alpha$  bands is very small due to the large restriction of  $\varepsilon_{32}$ . Further accommodation of the  $\varepsilon_{22}$  of the major  $\alpha$  during growth is realized by the repeated formation of the penetrating  $\alpha$  bands, as seen in Fig. 3.8 (a<sub>2</sub>).

**Table 3.4** Deformation gradient tensor of the penetrating  $\alpha$  expressed in the same BOR reference frame as for the major  $\alpha$  plate in Table 2

Deformation gradient tensor		
$\begin{pmatrix} 0.8984 & -0.1039 & 0.0248 \\ -0.2860 & 0.8675 & 0.0421 \\ -0.2617 & -0.4532 & 1.0778 \end{pmatrix}$		

### 3.6 Summary

In this work, the characteristics of  $\beta$  to  $\alpha$  phase transformation in Ti-7333 during the heat treatment were studied. Special attention was made to the lattice strain to realize the structure change from the BCC structure of the  $\beta$  phase to the HCP of the  $\alpha$  phase and its impact on the formation of the composite structure of the  $\alpha$  precipitates and on local variant selection.

The elastic strain generated by the  $\beta$  to  $\alpha$  transformation induces the formation of two kinds of nano-sized  $\alpha$  domains in each major  $\alpha$  plate. This demonstrates that the  $\alpha$  plates are rather polycrystalline than monocrystalline as has traditionally been considered. One kind of domains forms at the interfaces between the major  $\alpha$  plate and the  $\beta$  matrix (interface  $\alpha$ ). Such domains respect the BOR with the  $\beta$  matrix and related to the major  $\alpha$  by a  $60^\circ/\langle 11\bar{2}0 \rangle_\alpha$  rotation. The formation of such  $\alpha$  domains can effectively accommodate the shear strain and one component of the normal strain present at the interface between the major  $\alpha$  plate and the



$\beta$  matrix. The geometrical characteristics of the lattice strain of such  $\alpha$  domains allow a maximum profit from the low CRSS slip systems of the major  $\alpha$  plate and the  $\beta$  to minimize the overall strain. These domains further serve as sympathetic nuclei for the formation of the other major  $\alpha$  plate with the same orientation and contribute to the formation of the triangular structured major  $\alpha$  plate clusters.

The other  $\alpha$  domains (penetrating  $\alpha$ ) are in lamellar shape and organized into parallel bands going through the major  $\alpha$  plate. The broad faces of the bands are roughly normal to one of the large normal strains generated by the major  $\alpha$  plate. These  $\alpha$  domains are related with the major  $\alpha$  by a  $60^\circ/\langle 11\bar{2}0 \rangle_\alpha$  rotation but it does not obey the BOR with the  $\beta$  matrix. The formation of the bands of the penetrating  $\alpha$  domains is to accommodate the larger extension strain from the major  $\alpha$  plate. As these domains also generate large incompatible strains either with the major  $\alpha$  plate or with the  $\beta$  matrix, their growth are largely confined, thus each band is formed by the aligned and equally spaced identical penetrating  $\alpha$  domains. The results of the present work provide new information on the displacive characters of the  $\beta$  to  $\alpha$  phase transformation and its impact on the sub-structure and the microstructure features of the product  $\alpha$  phase. Such information can be incorporated to simulation models for  $\beta$  to  $\alpha$  transformation of Ti alloys.



## **Chapter 4 Phase transformation and $\alpha$ variant selection mechanism during isothermal compression**

### **4.1 Introduction**

For phase transformation in solid state, a specific orientation relationship (OR) between the parent phase and the product phase is present in many metals and alloys. Due to the symmetry of the parent and the product phase and the OR, the product phase can be represented with a fixed number of crystallographic orientation variants. When only a small subset of the variants is formed preferentially within one parent crystal, variant selection occurs. The variant selection plays an important role in determining the transformation texture and the final mechanical properties of the material, and is sensible to many external factors relating to the treatment processes. The previous investigations have evidenced that  $\alpha$  variant selection happens in both thermal and thermomechanical processes in Ti alloys. The selection could be induced by both internal materials factors and external treatment factors. The possible interplay between the imposed external deformation and the internal transformation lattice deformation is still not clearly addressed. In this chapter, a thorough investigation with statistical significance on phase transformation and variant selection in the Ti-7333 alloy under uniaxial isothermal compression was conducted at two temperatures (700 °C and 600 °C). Special attention was paid to the interplay between the transformation strain and the imposed strain and the applied load. This study is expected to work out the underlying mechanism of phase transformation variant selection that could be generalized to other alloys.

### **4.2 Experimental**

In this chapter, the Ti-7333 alloy was used. The detailed information on specimen preparation and isothermal compression experiment are given in Section 2.1 (page 18) and Section 2.2 (page 18) in Chapter 2, respectively. The microstructural and crystallographic features were investigated by SEM-EBSD and TEM.

### 4.3 Microstructure of the initial $\beta$ phase

For easy consultation of the initial microstructure, the as-solution-treated microstructure was presented again, as Fig. 4.1. It is seen that the alloy is composed of single  $\beta$  phase in the form of equiaxed grains with an average size of about 250  $\mu\text{m}$ . Such a microstructure is typical of metastable  $\beta$  Ti alloys [125, 126].

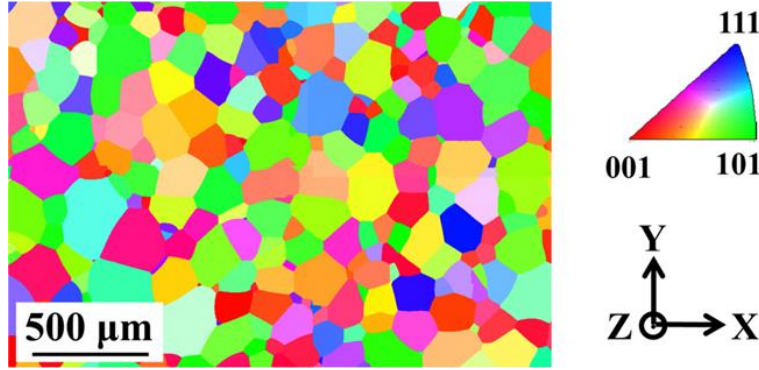


**Fig. 4.1** SEM-EBSD Y axis inverse pole figure (IPF) micrograph of the solution-treated Ti-7333 alloy. Y is parallel to the axial axis of the cylindrical specimen.

## 4.4 Phase transformation and $\alpha$ variant selection during 700 °C compression

### 4.4.1 Phase transformation and $\alpha$ variant selection in stress-free state

Fig. 4.2 displays the microstructures and the pole figures of the  $\beta$  and the  $\alpha$  phase in the 700°C aged specimen. It is seen that for the aged specimen three typical  $\alpha$  constituents, i.e.  $\alpha_{\text{GB}}$ ,  $\alpha_{\text{W}}$  and intragranular  $\alpha$  [127, 128], are formed (Fig. 4.2(a)). As the present work focuses on variant selection in a homogeneous environment, only the intragranular  $\alpha$  is considered. The  $\alpha_{\text{GB}}$  and  $\alpha_{\text{W}}$  are excluded as there exist additional influences from grain boundaries. Further orientation analyses show that the intragranular  $\alpha$  obeys the BOR with the  $\beta$  matrix (Fig. 4.2(c)) and the  $\alpha/\beta$  interfaces are close to the  $\{11\ 11\ 13\}_{\beta}$ , as mentioned in the last chapter. Globally, there are 12 BOR  $\alpha$  variants in each  $\beta$  grain (denoted V1 – V12, as detailed in Table A1 in Appendix), as indicated in Fig. 4.2(b) and (c). However, locally 3 specific variants form the characteristic triangular clusters, as outlined with the black rectangle in Fig.

4.2(b). These three variants are interrelated by a  $60^\circ$  rotation around the  $\langle 11\bar{2}0 \rangle_\alpha$  axis, as illustrated with the  $\langle 11\bar{2}0 \rangle_\alpha$  pole figures in Fig. 4.2(d). The formation mechanisms of the triangular variant clusters has been thoroughly studied in the last chapter.

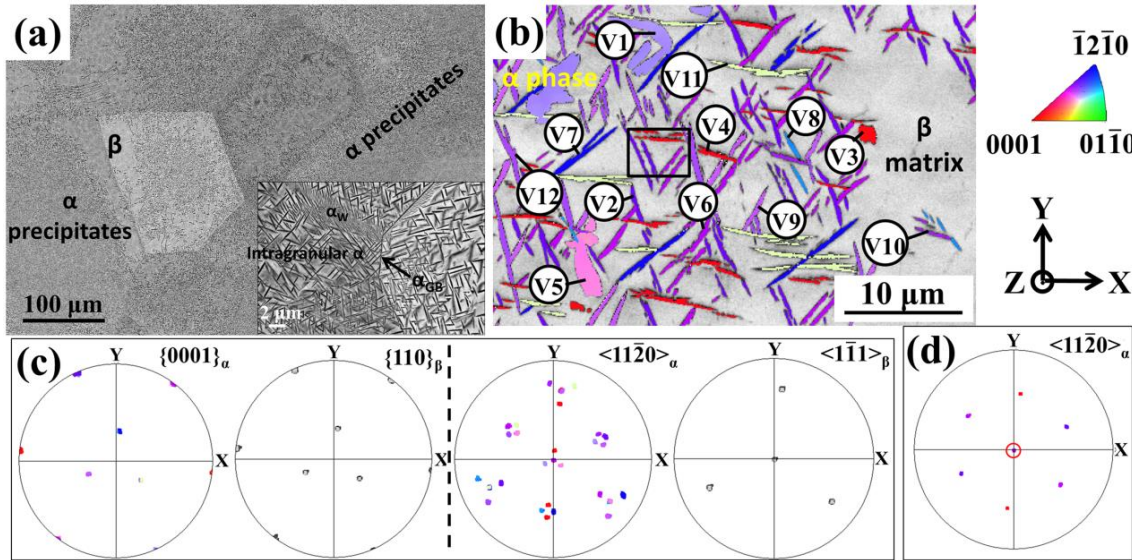


**Fig. 4.2** (a) BSE micrograph of the 700°C aged Ti-7333 alloy. The insert is a magnified micrograph showing grain boundary  $\alpha$  ( $\alpha_{GB}$ ), Widmanstätten  $\alpha$  ( $\alpha_W$ ) and intragranular  $\alpha$ . (b) EBSD micrograph ( $\beta$  in band quality contrast;  $\alpha$  in Y axis IPF micrograph. Y is the axial axis of the cylindrical specimen) demonstrating the triangular structured intragranular  $\alpha$  clusters in the 700°C aged specimen and the 12 orientation variants denoted V1 – V12. (c) BOR plane and direction pole figures of the 12  $\alpha$  variants and the  $\beta$  matrix in (b). (d)  $\langle 11\bar{2}0 \rangle_\alpha$  pole figures of the 3  $\alpha$  variants forming the triangular structure enclosed in the black rectangle in (b).

#### 4.4.2 Phase transformation and $\alpha$ variant selection under 700 °C isothermal compression

Fig. 4.3 shows the global microstructure of the Ti-7333 alloy after the isothermal compression. It can be seen that the  $\beta$  grains are deformed and elongated (Fig. 4.3 (a)). Global examination evidenced that the  $\beta$  to  $\alpha$  phase transformation happened selectively in the  $\beta$  grains, especially for the intragranular  $\alpha$  precipitates, which is in contrast to that in the aged specimen where the transformation is relatively homogeneous. For easy reference, the

intragranular  $\alpha$  precipitates are classified into two categories: group I and group II. In the former, large amount of intragranular  $\alpha$  precipitates appear in the central area of the  $\beta$  grains, as shown in Fig. 4.3 (b1), whereas in the latter, the  $\alpha$  precipitates appear occasionally in the  $\beta$  grain interiors, as shown in Fig. 4.3 (b2). The transformation is heavily affected by the deformation.

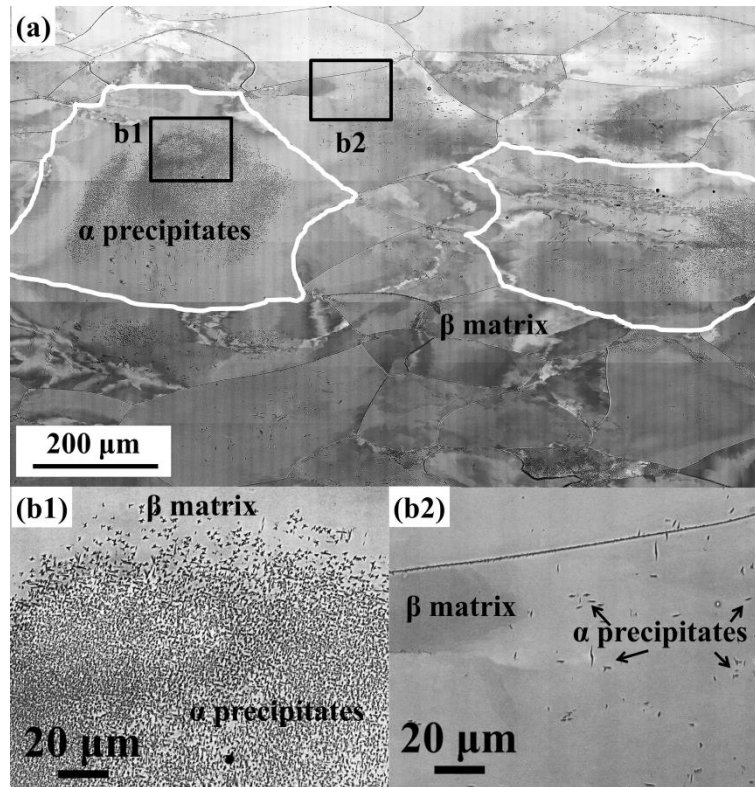


**Fig. 4.3** (a) BSE micrograph showing the global microstructure of Ti-7333 after the isothermal compression at 700°C to a true strain of 0.35 at a strain rate of  $10^{-3} \text{ s}^{-1}$ . (b1) and (b2) the magnified micrographs of the two kinds of representative  $\alpha$  precipitates outlined with the black frames in (a).

Detailed microstructural examinations revealed that for the group I  $\alpha$  precipitates they are still in plate shape but with much smaller sizes with respect to those in the aged specimen, inferring that the imposed strain is effective in refining the precipitates. In addition, the group I  $\alpha$  precipitates always tend to agglomerate in the center region of the  $\beta$  grains (Fig. 4.3 (a)). Close examinations revealed that the group I  $\alpha$  plates are oriented in two directions, forming the characteristic ‘cross-shaped’ clusters with the one variant intersecting the other, as shown

in Fig. 4.4 (a). Detailed crystallographic analysis using the SEM-EBSD orientation data revealed that the two  $\alpha$  plates (as indicated in Fig. 4.4 (a) with their EBSD Kikuchi line diffraction patterns in Fig. 4.4 (b)) still obey the BOR with the parent  $\beta$  grain, as shown with the OR plane and direction pole figures in Fig. 4.4 (c)). The two variants are interrelated by a  $90^\circ$  rotation around the  $\langle 1\ 1.38\ \overline{2.38}\ 0 \rangle_\alpha$  axis. Statistical analysis showed that the selected variant pair is either V6-V8 or V7-V12 in one  $\beta$  grain. This result demonstrates that strong variant selection occurred for the group I  $\alpha$  precipitates.

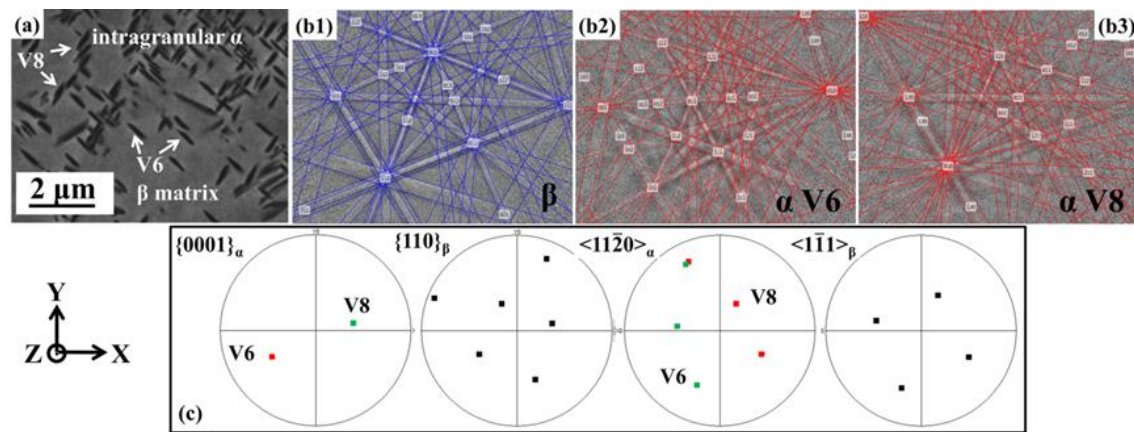


**Fig. 4.4** (a) BSE micrograph demonstrating the ‘cross-shaped’ clusters of the group I intragranular  $\alpha$  precipitates; (b1), (b2) and (b3) the experimental EBSD Kikuchi patterns with the calculated patterns of the  $\beta$  matrix and the two  $\alpha$  variants indicated in (a); (c) the corresponding BOR plane and direction pole figures of the two selected  $\alpha$  variants (V6 and V8) and the surrounding  $\beta$  matrix.

For the group II  $\alpha$  precipitates, they are mainly distributed in the more deformed and elongated  $\beta$  grains. It should be noted that the quantity of the  $\alpha$  precipitates in this group is very low. This indicates that the deformation of the  $\beta$  grains impedes the  $\beta$  to  $\alpha$  phase transformation and thus there exists a strong competition between the deformation of the  $\beta$  matrix and its phase transformation. This will be analyzed in detail later. The group II  $\alpha$  precipitates are still in plate shape. Crystallographic analysis showed that they still obey the BOR with the parent  $\beta$  grain. In contrast, the numbers of the variants are not consistent, varying from 2 to 4 from one  $\beta$  grain to another. This result still implies that variant selection also happened during the compression. When the grain contains only 2 variants, the 2 variants

possess the same disorientation as those in group I, i.e., interrelated by a  $90^\circ$  rotation around the  $\langle 1\ 1.38\ \overline{2.38}\ 0 \rangle_\alpha$  axis. However, when 3 or 4 variants are precipitated in one  $\beta$  grain, the orientation relationships between the variants are changed to  $60^\circ/\langle 11\overline{2}0 \rangle_\alpha$ ,  $60.832^\circ/\langle \overline{1.377}\ \overline{1}\ 2.377\ 0.359 \rangle_\alpha$  or  $63.2618^\circ/\langle \overline{1}0\ 5\ 5\ \overline{3} \rangle_\alpha$ . One example of the group II  $\alpha$  precipitates in one  $\beta$  grain is shown in Fig. 4.5. In this  $\beta$  grain, there appear 3 variants, i.e. V1, V5 and V6 (as shown in Fig. 4.5 (a) with their Kikuchi line diffraction patterns displayed in Fig. 4.5 (b) and their BOR is displayed with the OR plane and direction pole figures in Fig. 4.5 (c)). The orientation relationship between each pair of the variants is either  $60^\circ/\langle 11\overline{2}0 \rangle_\alpha$  (V1-V6),  $60.832^\circ/\langle \overline{1.377}\ \overline{1}\ 2.377\ 0.359 \rangle_\alpha$  (V5-V6) or  $63.2618^\circ/\langle \overline{1}0\ 5\ 5\ \overline{3} \rangle_\alpha$  (V1-V5). It should be noted that the microstructural and crystallographic characteristics of the two groups of  $\alpha$  precipitates were examined in all  $\beta$  grains in a large sample area ( $1.5 \times 1.2\ \text{mm}^2$ ). Their statistical representation was confirmed.

Further TEM examinations showed that dislocation quantities in the  $\beta$  grains with intensive  $\alpha$  precipitation (Group I) and with much less precipitation (Group II) are quite different, as shown with the representative TEM micrographs in Fig. 4.6. In the intensive precipitation regions, few dislocations appear (Fig. 4.6 (a)), whereas in the less precipitation regions, large amount of dislocations organized into dislocation bands (the so-called slip bands) are visible (Fig. 4.6 (b)). Further analysis using the method in [119] evidenced that the dislocations in the slip bands are the  $\{110\}_\beta \langle \overline{1}\overline{1}1 \rangle_\beta$  edge type dislocations. Moreover, it should be noted that no  $\{1\overline{1}\overline{2}\}_\beta \langle \overline{1}1\overline{1} \rangle_\beta$  dislocations were detected in the present deformed alloy. This result indicates that the dislocation slip in the  $\beta$  grains indeed suppresses the  $\alpha$  precipitation.



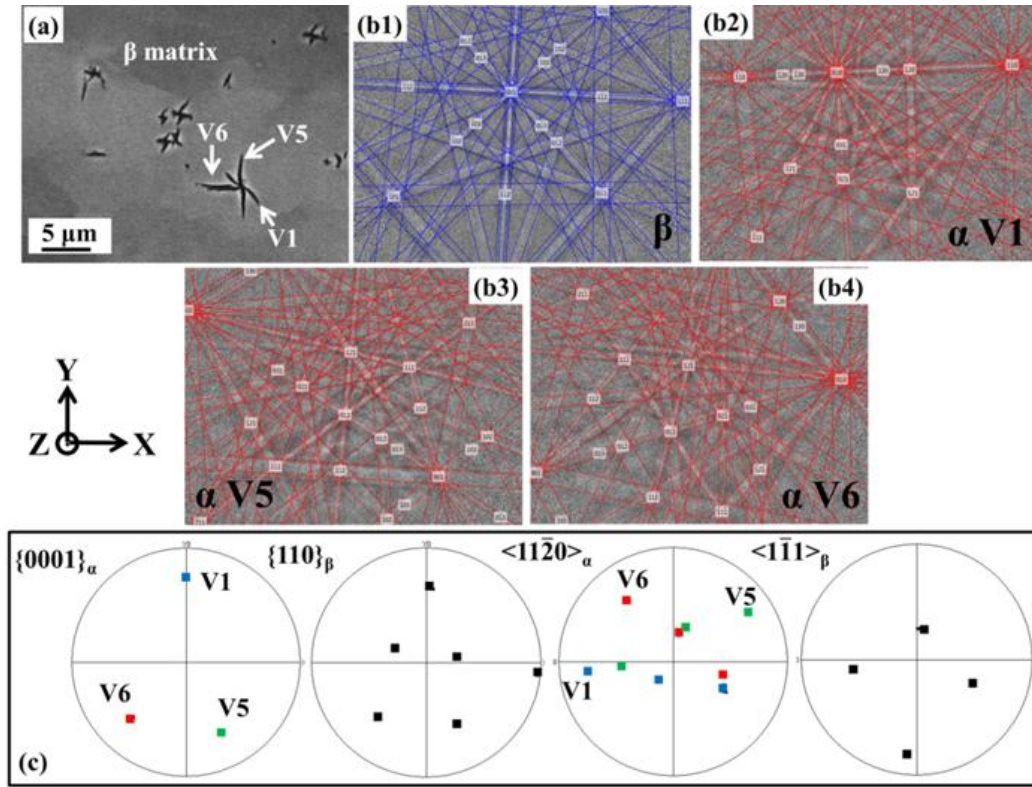


**Fig. 4.5** (a) BSE micrograph demonstrating the group II  $\alpha$  precipitates; (b1), (b2) (b3) and (b4) the experimental EBSD Kikuchi patterns with the calculated patterns of the  $\beta$  matrix and the  $\alpha$  variants V1, V5 and V6 in (a); (c) the corresponding BOR plane and direction pole figures of the  $\beta$  matrix and the three  $\alpha$  variants.

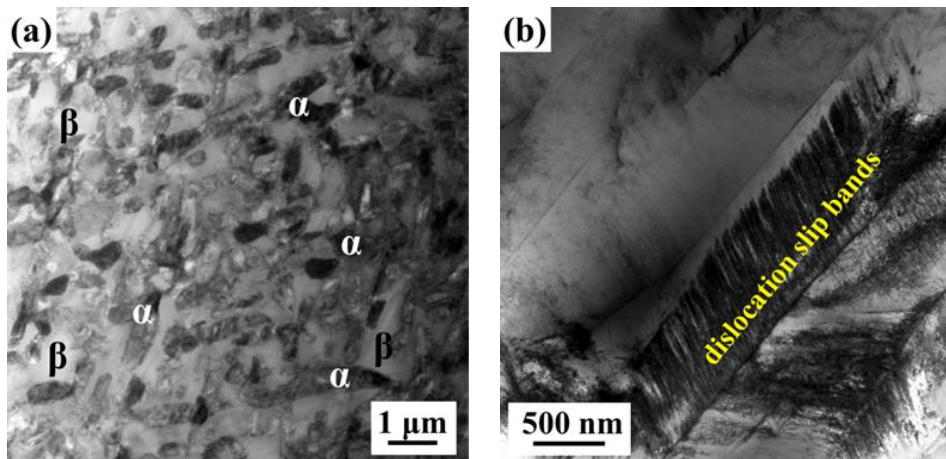


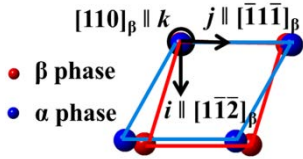
**Fig. 4.6** TEM bright field images showing (a) few dislocations in the  $\beta$  regions with large amount of  $\alpha$  precipitates and (b) few  $\alpha$  precipitates in the  $\beta$  regions containing large amount of dislocation slip bands.

### 4.4.3 Variant selection mechanisms

#### 4.4.3.1 $\beta$ to $\alpha$ phase transformation induced lattice strain

It is known that the  $\beta$  to  $\alpha$  phase transformation requires a crystal structure change from the parent BCC structure to the product HCP structure and a redistribution of the chemical elements. The structure transformation from  $\beta$  to  $\alpha$  can be regarded as a kind of crystal deformation, different from the common deformation processes in metallic materials, i.e., dislocation slip and twinning. Such a transformation associated deformation can be fully described by a displacement gradient tensor, as analyzed in detail in the previous chapter. Table 4.1 displays the displacement gradient tensor of each BOR  $\alpha$  variant expressed in the BOR reference frame. From the tensor, it is seen that the structure transformation is indeed composed of several strain components: 3 normal strains, i.e., a contraction in the  $[1\bar{1}\bar{2}]_\beta$  direction ( $\varepsilon_{11}$ ), an elongation in the  $[\bar{1}\bar{1}\bar{1}]_\beta$  ( $\varepsilon_{22}$ ) and in the  $[110]_\beta$  direction ( $\varepsilon_{33}$ ), and a shear on the  $(1\bar{1}\bar{2})_\beta$  plane and in the  $[1\bar{1}\bar{1}]_\beta$  direction ( $\varepsilon_{21}$ ). Obviously the shear strain component is the largest among all the components for the structure transformation. Interestingly, the shear system ( $\{1\bar{1}\bar{2}\}_\beta < \bar{1}\bar{1}\bar{1} >_\beta$ ) is also a well-recognized slip system in BCC crystals. Thus the most favorable variants should be the ones consume the maximum deformation work under the external compressive load.

**Table 4.1** Displacement gradient tensor of the variant expressed in its BOR reference frame ( $((110)_\beta // (0001)_\alpha$  and  $[\bar{1}\bar{1}\bar{1}]_\beta // [11\bar{2}0]_\alpha$ ).

OR reference frame	Displacement gradient tensor
	$\begin{pmatrix} -0.0416 & 0 & 0 \\ -\mathbf{0.1844} & 0.0434 & 0 \\ 0 & 0 & 0.0189 \end{pmatrix}$

In the present work, the deformation work  $U$  of the  $\alpha$  variants is evaluated following the Patel and Cohen method [129], i.e.,  $U = (\sum_p \sigma^p \delta^p + \sum_q \tau^q s^q)$ , where  $\sigma^p$  is the resolved normal stress from the applied load along the respective three principle axes of the BOR reference system,  $\delta^p$  the normal strain in the corresponding direction,  $\tau^q$  the shear stress

along the principle axis and in a planes perpendicular to the axis and  $s^q$  the corresponding shear strain. For simplicity, it is assumed that the  $\beta$  grains behave like a Sachs aggregate having the local microscopic stress state being identical to the applied compressive stress and we normalized the magnitude of the applied stress to 1, as treated in Ref. [130]. Then the deformation work  $U$  of all the 12 possible variants in each  $\beta$  grain by the external load was calculated in their BOR reference systems to figure out the selection criterion. The analyses were conducted for the  $\alpha$  precipitates in the two groups as detailed below.

#### 4.4.3.2 Origin of $\alpha$ variant selection in group I

With the measured orientations of the  $\beta$  grains, we calculated the deformation energy of all the 12 possible  $\alpha$  variants in each  $\beta$  grain in the observed area (containing 15 grains in the observed area of  $1.5 \times 1.2 \text{ mm}^2$ . The size of the grain is about  $250 \text{ }\mu\text{m}$ ). Table 4.2 displays an example of the deformation work of the 12 BOR  $\alpha$  variants from one parent  $\beta$  grain and the corresponding stress tensors expressed in the BOR frame of each variant. The experimentally observed (or selected) variants are highlighted in bold. It is seen that among the 12 BOR variants, only V6 and V8 have positive deformation work  $U > 0$ , inferring that the formation of these variants can consume the maximum imposed work of the macroscopic compression and thus they are preferentially selected, whereas the deformation work of the other variants (V1, V2, V3, V4, V5, V7, V9, V10, V11 and V12) are all negative, suggesting that the formation of these variants are not energetically favored by the macroscopic deformation. Between the two selected variants, V6 possesses the higher deformation energy. This variant should be energetically more advantageous. The microstructure observation indeed confirmed the appearance of the two variants and the dominant occurrence of V6.

**Table 4.2** One example of applied stress tensors and deformation work of the 12 possible BOR  $\alpha$  variants in one  $\beta$  grain within group I  $\alpha$  precipitates. The tensors of the applied stress are expressed in the BOR frame of the corresponding  $\alpha$  variant.

No.	Variant	Applied stress tensor	Deformation work
V1	$(110)_{\beta} // (0001)_{\alpha}$ $[\bar{1}\bar{1}\bar{1}]_{\beta} // [11\bar{2}0]_{\alpha}$	$\begin{pmatrix} -0.0020 & 0.0183 & 0.0405 \\ 0.0183 & -0.1689 & -0.3750 \\ 0.0405 & -0.3750 & -0.8282 \end{pmatrix}$	-0.0263
V2	$(110)_{\beta} // (0001)_{\alpha}$ $[\bar{1}\bar{1}1]_{\beta} // [11\bar{2}0]_{\alpha}$	$\begin{pmatrix} -0.1396 & 0.0670 & 0.3401 \\ 0.0670 & -0.0321 & -0.1632 \\ 0.3401 & -0.1632 & -0.8282 \end{pmatrix}$	-0.0263
V3	$(\bar{1}10)_{\beta} // (0001)_{\alpha}$ $[111]_{\beta} // [11\bar{2}0]_{\alpha}$	$\begin{pmatrix} -0.4761 & 0.4324 & 0.2499 \\ 0.4324 & -0.3927 & -0.2269 \\ 0.2499 & -0.2269 & -0.1311 \end{pmatrix}$	-0.0795
V4	$(\bar{1}10)_{\beta} // (0001)_{\alpha}$ $[11\bar{1}]_{\beta} // [11\bar{2}0]_{\alpha}$	$\begin{pmatrix} -0.1302 & 0.3101 & 0.1307 \\ 0.3101 & -0.7387 & -0.3112 \\ 0.1307 & -0.3112 & -0.1311 \end{pmatrix}$	-0.0863
V5	$(0\bar{1}1)_{\beta} // (0001)_{\alpha}$ $[111]_{\beta} // [11\bar{2}0]_{\alpha}$	$\begin{pmatrix} -0.0010 & -0.0197 & -0.0244 \\ -0.0197 & -0.3927 & -0.4880 \\ -0.0244 & -0.4880 & -0.6063 \end{pmatrix}$	-0.0248
V6	$(\bar{1}01)_{\beta} // (0001)_{\alpha}$ $[1\bar{1}\bar{1}]_{\beta} // [11\bar{2}0]_{\alpha}$	$\begin{pmatrix} -0.6567 & -0.4039 & 0.3375 \\ -0.4039 & -0.1698 & -0.1716 \\ 0.3375 & -0.1716 & -0.1735 \end{pmatrix}$	<b>0.0782</b>
V7	$(011)_{\beta} // (0001)_{\alpha}$ $[1\bar{1}\bar{1}]_{\beta} // [11\bar{2}0]_{\alpha}$	$\begin{pmatrix} -0.5866 & 0.3156 & 0.3780 \\ 0.3156 & -0.1698 & -0.2034 \\ 0.3780 & -0.2034 & -0.2436 \end{pmatrix}$	-0.0458
V8	$(101)_{\beta} // (0001)_{\alpha}$ $[11\bar{1}]_{\beta} // [11\bar{2}0]_{\alpha}$	$\begin{pmatrix} -0.2441 & -0.4246 & 0.0649 \\ -0.4246 & -0.7387 & 0.1129 \\ 0.0649 & 0.1129 & -0.0173 \end{pmatrix}$	<b>0.0561</b>
V9	$(011)_{\beta} // (0001)_{\alpha}$ $[11\bar{1}]_{\beta} // [11\bar{2}0]_{\alpha}$	$\begin{pmatrix} -0.0321 & -0.1748 & 0.1281 \\ -0.1748 & -0.9506 & 0.0236 \\ 0.1281 & 0.0236 & -0.0173 \end{pmatrix}$	-0.0080
V10	$(101)_{\beta} // (0001)_{\alpha}$ $[\bar{1}\bar{1}1]_{\beta} // [11\bar{2}0]_{\alpha}$	$\begin{pmatrix} -0.6177 & 0.1145 & -0.0657 \\ 0.1145 & -0.1387 & 0.4242 \\ -0.0657 & 0.4242 & -0.2436 \end{pmatrix}$	-0.0060
V11	$(\bar{1}01)_{\beta} // (0001)_{\alpha}$ $[111]_{\beta} // [11\bar{2}0]_{\alpha}$	$\begin{pmatrix} -0.5616 & 0.1078 & -0.4682 \\ 0.1078 & -0.0321 & 0.1396 \\ -0.4682 & 0.1396 & -0.4063 \end{pmatrix}$	-0.0056
V12	$(01\bar{1})_{\beta} // (0001)_{\alpha}$ $[\bar{1}\bar{1}1]_{\beta} // [11\bar{2}0]_{\alpha}$	$\begin{pmatrix} -0.0019 & -0.1139 & -0.2743 \\ -0.1139 & -0.9898 & -0.2610 \\ -0.2743 & -0.2610 & -0.0083 \end{pmatrix}$	-0.0220

**Table 4.3** Displacement gradient tensors of the 12 possible BOR  $\alpha$  variants in one  $\beta$  grain within group I  $\alpha$  precipitates expressed in the sample coordinate system and the resolved shear

$$\text{stress } \tau_{\{1\bar{1}\bar{2}\}_{\beta} < \bar{1}1\bar{1} >_{\beta}} \text{ on } \{1\bar{1}\bar{2}\}_{\beta} < \bar{1}1\bar{1} >_{\beta}.$$

No.	Variant	Displacement gradient tensor	$\tau_{\{1\bar{1}\bar{2}\}_{\beta} < \bar{1}1\bar{1} >_{\beta}}$
V1	$(110)_{\beta} // (0001)_{\alpha}$ $[\bar{1}1\bar{1}]_{\beta} // [11\bar{2}0]_{\alpha}$	$\begin{pmatrix} 0.0899 & -0.0128 & -0.0830 \\ -0.0467 & 0.0251 & 0.0570 \\ 0.0848 & -0.0115 & -0.0969 \end{pmatrix}$	0.0183
V2	$(110)_{\beta} // (0001)_{\alpha}$ $[\bar{1}11]_{\beta} // [11\bar{2}0]_{\alpha}$	$\begin{pmatrix} 0.0896 & -0.0431 & 0.0678 \\ -0.0092 & 0.0223 & -0.0052 \\ -0.0999 & 0.0633 & -0.0939 \end{pmatrix}$	0.0670
V3	$(\bar{1}10)_{\beta} // (0001)_{\alpha}$ $[111]_{\beta} // [11\bar{2}0]_{\alpha}$	$\begin{pmatrix} 0.0291 & 0.0356 & -0.0253 \\ 0.0202 & 0.0787 & -0.0402 \\ 0.0414 & 0.1309 & -0.0898 \end{pmatrix}$	0.4324
V4	$(\bar{1}10)_{\beta} // (0001)_{\alpha}$ $[11\bar{1}]_{\beta} // [11\bar{2}0]_{\alpha}$	$\begin{pmatrix} 0.0290 & 0.0215 & 0.0346 \\ 0.0369 & 0.0855 & 0.1150 \\ -0.0321 & -0.0561 & -0.0965 \end{pmatrix}$	0.3101
V5	$(0\bar{1}1)_{\beta} // (0001)_{\alpha}$ $[111]_{\beta} // [11\bar{2}0]_{\alpha}$	$\begin{pmatrix} -0.0809 & 0.0014 & 0.0521 \\ -0.1016 & 0.0257 & 0.0605 \\ -0.0914 & 0.0080 & 0.0752 \end{pmatrix}$	-0.0197
V6	$(\bar{1}01)_{\beta} // (0001)_{\alpha}$ $[1\bar{1}1]_{\beta} // [11\bar{2}0]_{\alpha}$	$\begin{pmatrix} \mathbf{0.0401} & \mathbf{0.1033} & \mathbf{0.0896} \\ \mathbf{-0.0151} & \mathbf{-0.0690} & \mathbf{-0.0777} \\ \mathbf{0.0128} & \mathbf{0.0409} & \mathbf{0.0569} \end{pmatrix}$	<b>-0.4039</b>
V7	$(011)_{\beta} // (0001)_{\alpha}$ $[1\bar{1}\bar{1}]_{\beta} // [11\bar{2}0]_{\alpha}$	$\begin{pmatrix} -0.0707 & -0.1425 & 0.0561 \\ 0.0098 & 0.0449 & -0.0132 \\ -0.0349 & -0.0633 & 0.0438 \end{pmatrix}$	0.3156
V8	$(101)_{\beta} // (0001)_{\alpha}$ $[11\bar{1}]_{\beta} // [11\bar{2}0]_{\alpha}$	$\begin{pmatrix} \mathbf{0.0291} & \mathbf{-0.0002} & \mathbf{-0.0102} \\ \mathbf{0.1367} & \mathbf{-0.0467} & \mathbf{-0.1077} \\ \mathbf{-0.0345} & \mathbf{0.0133} & \mathbf{0.0456} \end{pmatrix}$	<b>-0.4246</b>
V9	$(011)_{\beta} // (0001)_{\alpha}$ $[11\bar{1}]_{\beta} // [11\bar{2}0]_{\alpha}$	$\begin{pmatrix} -0.0805 & 0.0211 & -0.0448 \\ -0.1312 & 0.0562 & -0.0663 \\ 0.0462 & -0.0162 & 0.0424 \end{pmatrix}$	-0.1748
V10	$(101)_{\beta} // (0001)_{\alpha}$ $[\bar{1}11]_{\beta} // [11\bar{2}0]_{\alpha}$	$\begin{pmatrix} 0.0386 & 0.1289 & -0.0414 \\ -0.0080 & -0.0053 & 0.0226 \\ -0.0172 & -0.0984 & 0.0501 \end{pmatrix}$	0.1145
V11	$(\bar{1}01)_{\beta} // (0001)_{\alpha}$ $[111]_{\beta} // [11\bar{2}0]_{\alpha}$	$\begin{pmatrix} 0.0305 & -0.0051 & 0.0097 \\ 0.1134 & -0.0064 & 0.0538 \\ 0.0865 & -0.0648 & 0.0621 \end{pmatrix}$	0.1078
V12	$(01\bar{1})_{\beta} // (0001)_{\alpha}$ $[\bar{1}11]_{\beta} // [11\bar{2}0]_{\alpha}$	$\begin{pmatrix} -0.0716 & -0.1081 & -0.1052 \\ -0.0051 & 0.0266 & 0.0013 \\ 0.0383 & 0.0539 & 0.0730 \end{pmatrix}$	-0.1139

To elucidate the interplay of the macroscopic deformation (strain and applied load) with the lattice deformation of the selected variants that is behind the unique energy criterion and their influence on the morphology of the  $\alpha$  precipitates, the lattice deformation of the 12 variants are further expressed in the sample coordinate system X-Y-Z as presented in the microstructure figures and their resolved shear stress on the  $\{1\bar{1}\bar{2}\}_{\beta}<\bar{1}1\bar{1}>_{\beta}$  shear system are also calculated. The results are displayed in Table 4.3 and the experimentally observed (or selected) variants are highlighted in bold. As the Y axis is the compression axis, the elements in the second row of the tensor are of particular importance with respect to the imposed macroscopic compression.  $\varepsilon_{22}<0$  means that the  $\beta$  to  $\alpha$  transformation induces a contraction in the compression direction (Y direction). This contraction is compatible to the macroscopic compression and thus can effectively contribute to the macroscopic deformation. The negative  $\tau_{\{1\bar{1}\bar{2}\}_{\beta}<\bar{1}1\bar{1}>_{\beta}}$  implies that the shear stress revolved from the applied load on the  $\{1\bar{1}\bar{2}\}_{\beta}<\bar{1}1\bar{1}>_{\beta}$  shear system is in the same direction as that of the shear strain for structure transformation (that is also negative, as given in Table 4.1). It should be noted that the negative shear ensures a smallest atomic movement for structure transformation, as seen in the figure of the atomic correspondence between the  $\beta$  and the  $\alpha$  phase in Table 4.1. Thus the shear deformation to realize the structure transformation is unidirectional similar to the case of twinning. Only a negative resolved shear stress is possible to active the  $\{1\bar{1}\bar{2}\}_{\beta}<\bar{1}1\bar{1}>_{\beta}$  shear system for structure transformation. From Table 4.3, it is seen that the selected variants V6 and V8 satisfy simultaneously the two conditions, i.e.  $\varepsilon_{22}<0$  and  $\tau_{\{1\bar{1}\bar{2}\}_{\beta}<\bar{1}1\bar{1}>_{\beta}}<0$ . Thus the reasons behind the unique deformation energy criterion of the selected variants in Table 4.2 can be interpreted such that the resolved shear stress  $\tau_{\{1\bar{1}\bar{2}\}_{\beta}<\bar{1}1\bar{1}>_{\beta}}$  should be able to activate the  $\{1\bar{1}\bar{2}\}_{\beta}<\bar{1}1\bar{1}>_{\beta}$  shear system for the initiation of the transformation, as this shear system is a slip system of the  $\beta$  phase, and the shear amount is very large with respect to the normal strains (as shown in Table 4.1) and the growth of the variants should make maximum contribution to the macroscopic deformation. Such a compatible stress and strain characterized energy criterion of variant selection has been verified for all the group I  $\alpha$  precipitates in the large observation area mentioned above ( $1.5 \times 1.2 \text{ mm}^2$ ), and the results

represented by the  $\varepsilon_{22}$  values and the  $\tau_{\{1\bar{1}\bar{2}\}_{\beta} < \bar{1}1\bar{1} >_{\beta}}$  on the  $\{1\bar{1}\bar{2}\}_{\beta} < \bar{1}1\bar{1} >_{\beta}$  shear system are displayed in Fig. 4.7, where  $U > 0$  and  $U < 0$  are signified by the respective red and blue colors. As seen in the figure, for the selected variants, the deformation work  $U$  is always positive. In detail, they have both the smallest  $\tau_{\{1\bar{1}\bar{2}\}_{\beta} < \bar{1}1\bar{1} >_{\beta}}$  (from -0.4 to -0.5) and the smallest  $\varepsilon_{22}$  values ( $\varepsilon_{22} < 0$ ). For the inactive variants,  $U$  is negative and they have either positive  $\tau_{\{1\bar{1}\bar{2}\}_{\beta} < \bar{1}1\bar{1} >_{\beta}}$  for the  $\{1\bar{1}\bar{2}\}_{\beta} < \bar{1}1\bar{1} >_{\beta}$  shear systems (from 0.02 to 0.35) or the positive  $\varepsilon_{22}$  (from 0.0127 to 0.155). This statistical result further validates the energy criterion of the variant selection for the group I  $\alpha$  precipitates and this energy criterion corresponds to a compatible stress and strain associated selection mechanism, *i.e.*, only the variants that can receive the largest resolved shear stress from the applied compressive load to activate the  $\{1\bar{1}\bar{2}\}_{\beta} < \bar{1}1\bar{1} >_{\beta}$  shear system for structure transformation and that can make highest contribution to the macroscopic deformation will be selected. These variants also appear in highest amounts.

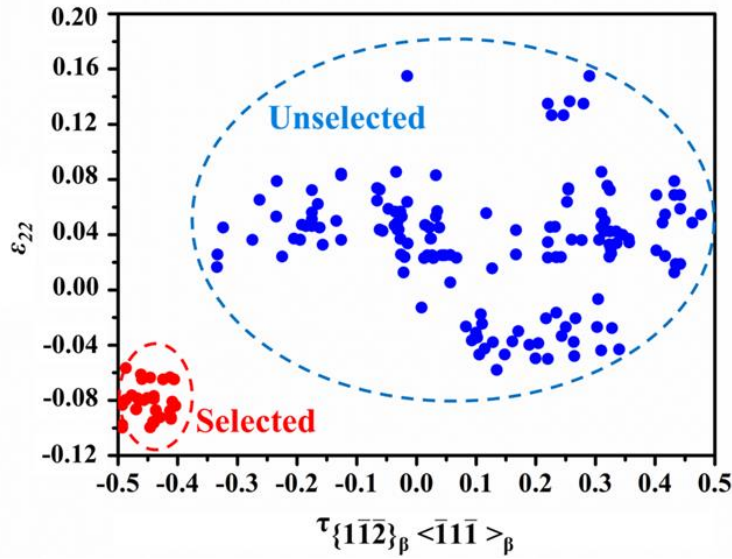


**Fig. 4.7** The resolved shear stress on  $\{1\bar{1}\bar{2}\}_{\beta} < \bar{1}1\bar{1} >_{\beta}$  shear system of all the possible group I  $\alpha$  variants under the external compressive load and their corresponding  $\varepsilon_{22}$  values in the observed area ( $1.5 \times 1.2 \text{ mm}^2$ ). The active variants consuming positive deformation work are in red, whereas the unselected variants consuming negative work are in blue.

It should be noted that any non-zero values of  $\varepsilon_{21}$  and  $\varepsilon_{23}$  in Table 4.3 represent shears in the direction of Y (compression direction). These shears increase the dimension of the  $\alpha$

precipitates with respect to the original  $\beta$  matrix in this direction, and thus could be incompatible with the macroscopic compression. The shear components  $\varepsilon_{21}$  and  $\varepsilon_{23}$  of V6 and V8 in group I are not zero, meaning that the formation of these variants also induces a dimension increase in the compression direction that cancels, to some extent, the contribution of  $\varepsilon_{22}$ . However, the dimension increase induced by the shear strain depends on the thickness of the precipitates in the two direction perpendicular to the compression direction (X and Z direction indicated in Fig. 4.4). To diminish the negative effect of the two shears, the size of the precipitates should be reduced. Thus the two shears induced by the structure transformation impede the growth of the  $\alpha$  precipitates. The smaller size of the group I precipitates with respect to those formed during aging is indeed confirmed by the microstructure observation.

#### 4.4.3.3 Origin of $\alpha$ variant selection in group II

The deformation energy criterion for the selection of the group I precipitates were verified for the group II  $\alpha$  precipitates. Table 4.4 shows the deformation work  $U$  of the 12 BOR  $\alpha$  variants from one parent  $\beta$  grain and their corresponding applied stress tensors expressed in the BOR frame of each variant. Table 4.5 displays the lattice deformation of the 12 variants in the sample coordinate system X-Y-Z and the  $\tau_{\{1\bar{1}\bar{2}\}_{\beta}<\bar{1}\bar{1}\bar{1}>_{\beta}}$  on the  $\{1\bar{1}\bar{2}\}_{\beta}<\bar{1}\bar{1}\bar{1}>_{\beta}$  shear system to further resolve the interplay of the imposed deformation and the applied loads with the transformation deformation. In the two tables the selected variants are highlighted in bold. In this example, there are 5 variants (V1, V2, V5, V6 and V11) satisfying the energy criterion (having the positive work) (Table 4.4) and the formation of these variants receives a negative  $\tau_{\{1\bar{1}\bar{2}\}_{\beta}<\bar{1}\bar{1}\bar{1}>_{\beta}}$  (Table 4.5) that is prerequisite for the activation of the  $\{1\bar{1}\bar{2}\}_{\beta}<\bar{1}\bar{1}\bar{1}>_{\beta}$  shear system for transformation and provides a contraction in the compression direction, making positive contribution to the macroscopic deformation, however, only 3 variants (V1, V5 and V6) were detected (Table 4.4 and 4.5). Thus, in principle the energy criterion of the selection is respected by the transformation but with restrictions. The energy criterion and the compatible stress and strain characters of the selected variants were further verified with all the group II  $\alpha$  precipitates in the whole observation area (containing 9 grains in the observed area of  $1.5 \times 1.2 \text{ mm}^2$ ) and the results are displayed in Fig. 4.8.



**Table 4.4** One example of applied stress tensors and deformation work of the 12 possible BOR  $\alpha$  variants in one  $\beta$  grain within group II  $\alpha$  precipitates. The applied stress tensors are expressed in the BOR frame of each  $\alpha$  variant.

No.	Variant	Applied stress tensor	Deformation work
V1	$(110)_{\beta} // (0001)_{\alpha}$ $[\bar{1}\bar{1}\bar{1}]_{\beta} // [11\bar{2}0]_{\alpha}$	$\begin{pmatrix} -0.0777 & -0.0987 & -0.2528 \\ -0.0987 & -0.0992 & -0.2857 \\ -0.2528 & -0.2857 & -0.8232 \end{pmatrix}$	<b>0.0016</b>
V2	$(110)_{\beta} // (0001)_{\alpha}$ $[\bar{1}\bar{1}\bar{1}]_{\beta} // [11\bar{2}0]_{\alpha}$	$\begin{pmatrix} -0.1519 & -0.0615 & 0.3536 \\ -0.0615 & -0.0249 & 0.1431 \\ 0.3536 & 0.1431 & -0.8232 \end{pmatrix}$	0.0010
V3	$(\bar{1}10)_{\beta} // (0001)_{\alpha}$ $[111]_{\beta} // [11\bar{2}0]_{\alpha}$	$\begin{pmatrix} -0.7326 & 0.4329 & 0.0826 \\ 0.4329 & -0.2545 & -0.0485 \\ 0.0826 & -0.0485 & -0.0093 \end{pmatrix}$	-0.0604
V4	$(\bar{1}10)_{\beta} // (0001)_{\alpha}$ $[11\bar{1}]_{\beta} // [11\bar{2}0]_{\alpha}$	$\begin{pmatrix} -0.0360 & 0.1853 & 0.0182 \\ 0.1853 & -0.9548 & -0.0940 \\ 0.0182 & -0.0940 & -0.0093 \end{pmatrix}$	-0.0743
V5	$(0\bar{1}1)_{\beta} // (0001)_{\alpha}$ $[111]_{\beta} // [11\bar{2}0]_{\alpha}$	$\begin{pmatrix} -0.1195 & -0.1744 & -0.2735 \\ -0.1744 & -0.2545 & -0.3991 \\ -0.2735 & -0.3991 & -0.6260 \end{pmatrix}$	<b>0.0143</b>
V6	$(\bar{1}01)_{\beta} // (0001)_{\alpha}$ $[1\bar{1}\bar{1}]_{\beta} // [11\bar{2}0]_{\alpha}$	$\begin{pmatrix} -0.4178 & -0.2585 & -0.4492 \\ -0.2585 & -0.0992 & -0.2188 \\ -0.4492 & -0.2188 & -0.4830 \end{pmatrix}$	<b>0.0415</b>
V7	$(011)_{\beta} // (0001)_{\alpha}$ $[1\bar{1}\bar{1}]_{\beta} // [11\bar{2}0]_{\alpha}$	$\begin{pmatrix} -0.8558 & 0.2913 & 0.1964 \\ 0.2913 & -0.0992 & -0.0669 \\ 0.1964 & -0.0669 & -0.0451 \end{pmatrix}$	-0.0233
V8	$(101)_{\beta} // (0001)_{\alpha}$ $[11\bar{1}]_{\beta} // [11\bar{2}0]_{\alpha}$	$\begin{pmatrix} -0.0317 & -0.1741 & 0.0207 \\ -0.1741 & -0.9548 & 0.1134 \\ 0.0207 & 0.1134 & -0.0135 \end{pmatrix}$	-0.0083
V9	$(011)_{\beta} // (0001)_{\alpha}$ $[11\bar{1}]_{\beta} // [11\bar{2}0]_{\alpha}$	$\begin{pmatrix} -0.2616 & 0.1547 & 0.1138 \\ 0.1547 & -0.7249 & -0.0183 \\ 0.1138 & -0.0183 & -0.0135 \end{pmatrix}$	-0.0494
V10	$(101)_{\beta} // (0001)_{\alpha}$ $[\bar{1}\bar{1}\bar{1}]_{\beta} // [11\bar{2}0]_{\alpha}$	$\begin{pmatrix} -0.5001 & 0.0112 & 0.0024 \\ 0.0112 & -0.4548 & 0.2075 \\ 0.0024 & 0.2075 & -0.0451 \end{pmatrix}$	-0.0019
V11	$(\bar{1}01)_{\beta} // (0001)_{\alpha}$ $[111]_{\beta} // [11\bar{2}0]_{\alpha}$	$\begin{pmatrix} -0.3491 & -0.0935 & -0.4675 \\ -0.0935 & -0.0249 & -0.1248 \\ -0.4675 & -0.1248 & -0.6260 \end{pmatrix}$	0.0188
V12	$(01\bar{1})_{\beta} // (0001)_{\alpha}$ $[\bar{1}\bar{1}\bar{1}]_{\beta} // [11\bar{2}0]_{\alpha}$	$\begin{pmatrix} -0.9045 & 0.2086 & -0.3561 \\ 0.2086 & -0.0630 & 0.3506 \\ -0.3561 & -0.3506 & -0.0325 \end{pmatrix}$	-0.0042

**Table 4.5** Displacement gradient tensors of the 12 possible BOR  $\alpha$  variants in one  $\beta$  grain (group II  $\alpha$  precipitates) expressed in the sample coordinate system and the resolved shear

$$\text{stress } \tau_{\{1\bar{1}\bar{2}\}_{\beta} < \bar{1}1\bar{1} >_{\beta}} \text{ on } \{1\bar{1}\bar{2}\}_{\beta} < \bar{1}1\bar{1} >_{\beta}.$$

No.	Variant	Deformation gradient tensor	$\tau_{\{1\bar{1}\bar{2}\}_{\beta} < \bar{1}1\bar{1} >_{\beta}}$
V1	$(110)_{\beta} // (0001)_{\alpha}$ $[\bar{1}\bar{1}\bar{1}]_{\beta} // [11\bar{2}0]_{\alpha}$	$\begin{pmatrix} \mathbf{0.0982} & \mathbf{0.0227} & \mathbf{-0.0633} \\ \mathbf{-0.0537} & \mathbf{-0.0011} & \mathbf{0.0492} \\ \mathbf{0.1040} & \mathbf{0.0362} & \mathbf{-0.0794} \end{pmatrix}$	<b>-0.0987</b>
V2	$(110)_{\beta} // (0001)_{\alpha}$ $[\bar{1}\bar{1}1]_{\beta} // [11\bar{2}0]_{\alpha}$	$\begin{pmatrix} 0.1011 & -0.0463 & 0.0872 \\ 0.0301 & -0.0023 & 0.0382 \\ -0.0801 & 0.0511 & -0.0808 \end{pmatrix}$	-0.0615
V3	$(\bar{1}10)_{\beta} // (0001)_{\alpha}$ $[111]_{\beta} // [11\bar{2}0]_{\alpha}$	$\begin{pmatrix} 0.0171 & -0.0033 & 0.0023 \\ 0.0045 & 0.0598 & -0.0100 \\ 0.0200 & 0.1733 & -0.0588 \end{pmatrix}$	0.4329
V4	$(\bar{1}10)_{\beta} // (0001)_{\alpha}$ $[11\bar{1}]_{\beta} // [11\bar{2}0]_{\alpha}$	$\begin{pmatrix} 0.0173 & 0.0064 & 0.0194 \\ -0.0014 & 0.0736 & 0.1611 \\ 0.0017 & -0.0222 & -0.0728 \end{pmatrix}$	0.1853
V5	$(0\bar{1}1)_{\beta} // (0001)_{\alpha}$ $[111]_{\beta} // [11\bar{2}0]_{\alpha}$	$\begin{pmatrix} \mathbf{-0.0343} & \mathbf{-0.0195} & \mathbf{0.0125} \\ \mathbf{-0.1036} & \mathbf{-0.0123} & \mathbf{0.0354} \\ \mathbf{-0.1334} & \mathbf{-0.0396} & \mathbf{0.0677} \end{pmatrix}$	<b>-0.1744</b>
V6	$(\bar{1}01)_{\beta} // (0001)_{\alpha}$ $[\bar{1}\bar{1}1]_{\beta} // [11\bar{2}0]_{\alpha}$	$\begin{pmatrix} \mathbf{-0.0082} & \mathbf{0.0952} & \mathbf{0.1234} \\ \mathbf{0.0189} & \mathbf{-0.0325} & \mathbf{-0.0738} \\ \mathbf{-0.0047} & \mathbf{0.0345} & \mathbf{0.0687} \end{pmatrix}$	<b>-0.2585</b>
V7	$(011)_{\beta} // (0001)_{\alpha}$ $[1\bar{1}\bar{1}]_{\beta} // [11\bar{2}0]_{\alpha}$	$\begin{pmatrix} -0.0300 & -0.1578 & 0.0108 \\ -0.0050 & 0.0226 & -0.0044 \\ -0.0284 & -0.0998 & 0.0254 \end{pmatrix}$	0.2913
V8	$(101)_{\beta} // (0001)_{\alpha}$ $[11\bar{1}]_{\beta} // [11\bar{2}0]_{\alpha}$	$\begin{pmatrix} -0.0112 & 0.0084 & 0.0146 \\ 0.1690 & 0.0076 & -0.0912 \\ -0.0068 & -0.0033 & 0.0217 \end{pmatrix}$	-0.1741
V9	$(011)_{\beta} // (0001)_{\alpha}$ $[11\bar{1}]_{\beta} // [11\bar{2}0]_{\alpha}$	$\begin{pmatrix} -0.0414 & 0.0017 & -0.0372 \\ -0.1511 & 0.0395 & -0.1000 \\ 0.0019 & -0.0046 & 0.0199 \end{pmatrix}$	0.1547
V10	$(101)_{\beta} // (0001)_{\alpha}$ $[\bar{1}\bar{1}1]_{\beta} // [11\bar{2}0]_{\alpha}$	$\begin{pmatrix} 0.0031 & 0.1697 & -0.0147 \\ 0.0091 & -0.0108 & -0.0012 \\ 0.0067 & -0.0891 & 0.0257 \end{pmatrix}$	0.0112
V11	$(\bar{1}01)_{\beta} // (0001)_{\alpha}$ $[111]_{\beta} // [11\bar{2}0]_{\alpha}$	$\begin{pmatrix} -0.0198 & 0.0238 & -0.0130 \\ 0.1001 & -0.0094 & 0.0466 \\ 0.1151 & -0.0617 & 0.0772 \end{pmatrix}$	-0.0935
V12	$(01\bar{1})_{\beta} // (0001)_{\alpha}$ $[\bar{1}\bar{1}1]_{\beta} // [11\bar{2}0]_{\alpha}$	$\begin{pmatrix} -0.0198 & -0.1011 & -0.1409 \\ -0.0169 & -0.0199 & -0.0497 \\ 0.0039 & 0.0253 & 0.0578 \end{pmatrix}$	0.2086

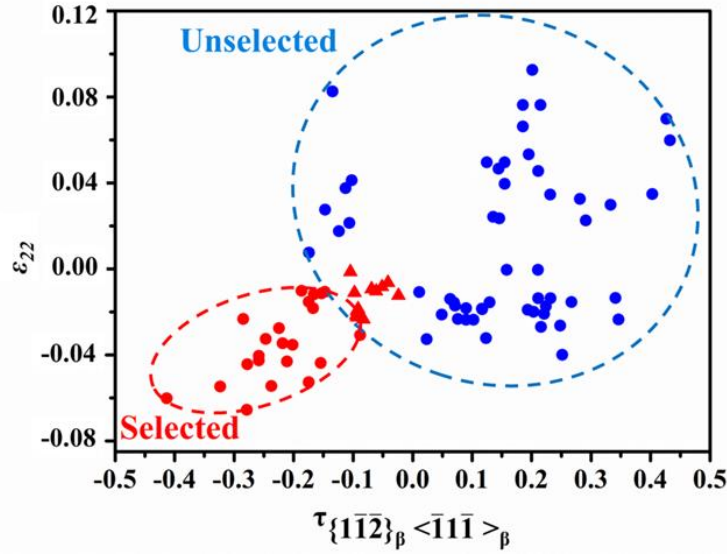


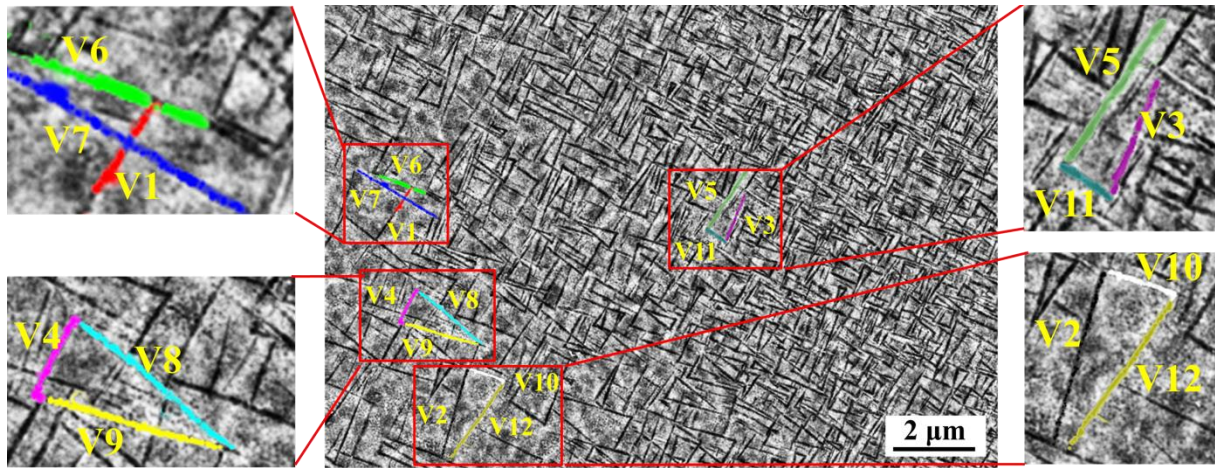
**Fig. 4.8** The resolved shear stress on  $\{1\bar{1}\bar{2}\}_{\beta} < \bar{1}1\bar{1} >_{\beta}$  shear systems of all the possible group II  $\alpha$  variants under the external compressive load and their corresponding  $\epsilon_{22}$  values in the observed area ( $1.5 \times 1.2 \text{ mm}^2$ ). The active variants consuming positive deformation work are in red, whereas the unselected variants consuming negative work are in blue. For the unselected variants consuming positive work, they are represented with the red triangles.

It is seen that for the selected variants the energy criterion is well respected and the compatible characters of the macroscopic compression with the lattice strain and the  $\tau_{\{1\bar{1}\bar{2}\}_{\beta} < \bar{1}1\bar{1} >_{\beta}}$  with the shear strain for transformation are well reproduced. However, there are still some variants that fulfill the energy criteria and possess the compatible characters with the macroscopic deformation that did not appear, as indicated with the red triangles in Fig. 4.8. For such variants, the resolved shear stress on their  $\{1\bar{1}\bar{2}\}_{\beta} < \bar{1}1\bar{1} >_{\beta}$  shear systems and their  $\epsilon_{22}$  are very close to the limit (-0.0945 to -0.0237 for the  $\tau_{\{1\bar{1}\bar{2}\}_{\beta} < \bar{1}1\bar{1} >_{\beta}}$  and -0.0234 to -0.0013 for the  $\epsilon_{22}$ ), meaning that they receive limited resolved shear stress to activate the  $\{1\bar{1}\bar{2}\}_{\beta} < \bar{1}1\bar{1} >_{\beta}$  shear system for phase transformation and provide limited contribution to the macroscopic compression. Moreover, the local environment of the host  $\beta$  grains also exerts strong influence on the formation of such variants. For the group II  $\alpha$  precipitates, they are nucleated in the  $\beta$  grains heavily deformed by dislocation slip. As evidenced by the TEM observations (Fig. 4.6 (b)), large amount of  $\{110\}_{\beta} < \bar{1}1\bar{1} >_{\beta}$  dislocations exist in the host  $\beta$  grains of the group II  $\alpha$  precipitates. Calculation demonstrated that for these  $\beta$  grains the  $\{110\}_{\beta} < \bar{1}1\bar{1} >_{\beta}$

slip systems are indeed at the favorable activation position (Schmid Factors  $>0.42$ ). As the dislocations are organized in slip bands and the bands nearly occupy the entire  $\beta$  grains, we can deduce that dislocation multiplication and dynamic recovery happened intensively during the deformation, and in consequence, the  $\beta$  lattice is largely distorted. Such an environment is unfavorable for the  $\beta$  to  $\alpha$  transformation as the phase transformation requires certain crystalline perfection to realize the coordinated atomic movements for the structure change. Thus with the modified local stress and strain state, the formation of the variants with less competitiveness with respect to the external compression is not certain. They can be selected or not selected depending on the local state of the  $\beta$  grain. Thus the selection of the  $\alpha$  variants are further restricted by the local stress and strain conditions.

## 4.5 Phase transformation and $\alpha$ variant selection during 600°C compression

### 4.5.1 Phase transformation and $\alpha$ variant selection during heat treatment



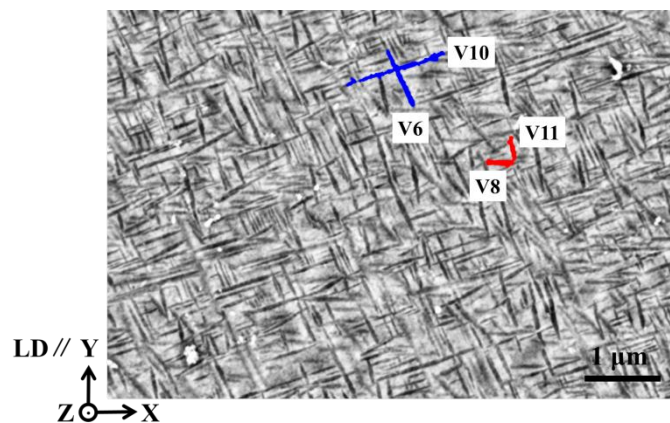
**Fig. 4.9** BSE micrograph of the 600°C aged Ti-7333 alloy. The micrograph shows the 12 intragranular  $\alpha$  precipitates formed during the heat treatment. The variants are denoted V1 – V12 and indicated with different colors lines. The 12 variants form 4 characteristic triangles as shown in the magnified micrographs.

Fig. 4.9 displays the microstructure of the 600°C aged specimen. It is seen that the intragranular  $\alpha$  precipitates were intensively formed and organized in the so-called

basket-weave structures during the isothermal holding. For this part of work, only the  $\alpha$  variant selection of the intragranular  $\alpha$  precipitates was focused, as the case of the 700°C aged specimen. Orientation analyses show that the BOR is still obeyed by the intragranular  $\alpha$  precipitates and the  $\beta$  matrix and the  $\alpha/\beta$  interfaces are also close to the  $\{11\ 11\ 13\}_{\beta}$ . Thus, the  $\alpha/\beta$  interface traces were further used to identify the  $\alpha$  variants in one  $\beta$  grain by using the trace analysis method [119]. The analysis results show that there are still 12 BOR  $\alpha$  variants in each  $\beta$  grain (denoted V1 – V12), as shown in the magnified micrographs in Fig. 4.9. This means that globally all the variants are precipitated. This is consistent with the case of the phase transformation at 700 °C. Further microstructure examinations revealed that locally 3 specific variants are formed in the characteristic triangular clusters. Totally, the 12 BOR  $\alpha$  variants form 4 triangular clusters, as represented with the different color lines in the magnified micrographs in Fig. 4.9. The formation mechanisms of the triangular variant clusters have been thoroughly studied in the previous chapter (Section 3.4 Page 36).

## 4.5.2 Phase transformation and $\alpha$ variant selection during 600 °C isothermal compression

### 4.5.2.1 Microstructural and crystallographic characteristics



**Fig. 4.10** BSE micrographs of the Ti-7333 alloy after the isothermal compression at 600 °C to a true strain of 0.10 showing the intragranular  $\alpha$  precipitates. Y is the compression axis. LD means Loading Direction.

Fig. 4.10 shows one representative example of the microstructure of the Ti-7333 alloy after the isothermal compression at 600 °C to a true strain of 0.10. It can be seen that the  $\alpha$  precipitates are still in plate shape, as the case of the intragranular  $\alpha$  precipitates in the aged specimen. However, compared with the sizes of the  $\alpha$  in that case, the intragranular  $\alpha$  precipitates in the compressed specimen are much smaller, inferring that the imposed strain is effective in refining the precipitates. Moreover, compared with the compression at 700 °C, the microstructural characteristics in the two temperatures are different. For the compression at 600 °C, all  $\beta$  grains are covered with the  $\alpha$  precipitates and the amount of precipitation is higher than the case at 700 °C. This should be due to the temperature effect. The phase transformation at 600 °C possesses a higher undercooling for the transformation than that at 700 °C and then equilibrium amount of the transformation is much higher at 600 °C. The microstructure examination in large sample areas showed that the  $\alpha$  plates are often oriented in four different directions and form two sets of ‘cross-shaped’ clusters, as indicated in Fig. 4.10. Crystallographic analysis revealed that there are four  $\alpha$  variants that still obey the BOR with the parent  $\beta$  grain and the  $\beta/\alpha$  interfaces are still close to the  $\{11\ 11\ 13\}_\beta$ . The selected variants in one  $\beta$  grain are V6-V8-V10-V11. The two clusters are constituted of V6-V10 and V8-V11, as indicated with blue and red color lines in Fig. 4.10. The orientation relationship of the two variants in each cross-shaped cluster is either  $90^\circ/\langle 1\ 1.38\ \overline{2.38}\ 0 \rangle_\alpha$  (V6-V10) or  $10^\circ/\langle 0001 \rangle$  (V6-V11). Such characteristics of the intragranular  $\alpha$  precipitates are checked in a large sample area ( $2 \times 2\ \text{mm}^2$ ) and the statistical relevance of the results is confirmed.

#### 4.5.2.2 Variant selection mechanism

Clearly, there is a strong variant selection during the isothermal compression at 600°C. Considering the existence of strong interaction between the lattice deformation of the phase transformation and the imposed macroscopic deformation and resultant variant selection at 700°C, the transformation lattice deformation strain is used to evaluate the interplay between the lattice deformation and the imposed macroscopic strain and the two selection criteria at 700 °C, i.e., a) the maximum accommodation to the macroscopic deformation, and b) the maximum resolved shear stress on the  $\{1\ \overline{1}\ \overline{2}\}_\beta/\langle \overline{1}\ 1\ \overline{1} \rangle_\beta$  shear systems for the phase transformation were taken into account. Hence, similarly, with the measured orientations of

the  $\beta$  grains and the BOR, the transformation displacement gradient tensors of all the 12 possible  $\alpha$  variants in the  $\beta$  grains in the examined area ( $2 \times 2 \text{ mm}^2$ ) were calculated. The displacement gradient tensors were expressed in the macroscopic sample coordinate system X-Y-Z drawn in the microstructure figures.

Table 4.6 displays one example of the transformation displacement gradient tensors of the 12 BOR  $\alpha$  variants in one parent  $\beta$  grain. Meanwhile, the resolved shear stress of a unitary external load on the  $\{1\bar{1}2\}_{\beta} <\bar{1}1\bar{1}>_{\beta}$  shear systems of each variant was also calculated and is listed in the table. The selected variants are highlighted in bold. It is clearly seen that among the 12 BOR variants, only V6 and V10 satisfy simultaneously the two selection criteria, whereas V8 and V11 respect only the strain accommodation criterion, and V5 and V12 obey only the resolved shear stress criterion. In the experiment observation, V6, V8, V10 and V11 are formed during the compression, whereas V5 and V12 did not appear. This selection situation suggests that for the 600 °C compression the accommodation to the macroscopic compression should be the most important criterion. Thus only the 4 variants among the 12 variants are favorable and can be selected. Such a strain compatible variant selection criterion was verified in the large observation area mentioned above ( $2 \times 2 \text{ mm}^2$ ) and was obeyed by appearing variants.

**Table 4.6** One example of displacement gradient tensors of the 12 possible BOR  $\alpha$  variants in one  $\beta$  grain expressed in the sample coordinate system and the resolved shear stress

$\tau_{\{1\bar{1}2\}_{\beta} < \bar{1}1\bar{1} >_{\beta}}$  on  $\{1\bar{1}2\}_{\beta} < \bar{1}1\bar{1} >_{\beta}$  shear system for phase transformation.

No.	Variant	Deformation gradient tensor	$\tau_{\{1\bar{1}2\}_{\beta} < \bar{1}1\bar{1} >_{\beta}}$
V1	$(110)_{\beta} // (0001)_{\alpha}$ $[\bar{1}\bar{1}\bar{1}]_{\beta} // [11\bar{2}0]_{\alpha}$	$\begin{pmatrix} 0.0982 & 0.0227 & -0.0633 \\ -0.0537 & 0.0111 & 0.0492 \\ 0.1040 & 0.0362 & -0.0794 \end{pmatrix}$	0.0273
V2	$(110)_{\beta} // (0001)_{\alpha}$ $[\bar{1}\bar{1}1]_{\beta} // [11\bar{2}0]_{\alpha}$	$\begin{pmatrix} 0.1011 & -0.0463 & 0.0872 \\ 0.0301 & 0.0323 & 0.0382 \\ -0.0801 & 0.0511 & -0.0808 \end{pmatrix}$	0.0540
V3	$(\bar{1}10)_{\beta} // (0001)_{\alpha}$ $[111]_{\beta} // [11\bar{2}0]_{\alpha}$	$\begin{pmatrix} 0.0171 & -0.0033 & 0.0023 \\ 0.0045 & 0.0598 & -0.0100 \\ 0.0200 & 0.1733 & -0.0588 \end{pmatrix}$	0.4124
V4	$(\bar{1}10)_{\beta} // (0001)_{\alpha}$ $[11\bar{1}]_{\beta} // [11\bar{2}0]_{\alpha}$	$\begin{pmatrix} 0.0173 & 0.0064 & 0.0194 \\ -0.0014 & 0.0736 & 0.1611 \\ 0.0017 & -0.0222 & -0.0728 \end{pmatrix}$	0.3401
V5	$(0\bar{1}1)_{\beta} // (0001)_{\alpha}$ $[111]_{\beta} // [11\bar{2}0]_{\alpha}$	$\begin{pmatrix} -0.0343 & -0.0195 & 0.0125 \\ -0.1036 & 0.0123 & 0.0354 \\ -0.1334 & -0.0396 & 0.0677 \end{pmatrix}$	-0.0097
V6	$(\bar{1}01)_{\beta} // (0001)_{\alpha}$ $[1\bar{1}\bar{1}]_{\beta} // [11\bar{2}0]_{\alpha}$	$\begin{pmatrix} -0.0037 & -0.0174 & -0.0388 \\ -0.0802 & -0.0399 & -0.1541 \\ 0.0202 & 0.0088 & 0.0617 \end{pmatrix}$	-0.4899
V7	$(011)_{\beta} // (0001)_{\alpha}$ $[1\bar{1}\bar{1}]_{\beta} // [11\bar{2}0]_{\alpha}$	$\begin{pmatrix} -0.0300 & -0.1578 & 0.0108 \\ -0.0050 & 0.0226 & -0.0044 \\ -0.0284 & -0.0998 & 0.0254 \end{pmatrix}$	0.2156
V8	$(101)_{\beta} // (0001)_{\alpha}$ $[11\bar{1}]_{\beta} // [11\bar{2}0]_{\alpha}$	$\begin{pmatrix} 0.0678 & -0.1414 & -0.0835 \\ 0.0196 & -0.0606 & -0.0445 \\ 0.0003 & -0.0127 & 0.0108 \end{pmatrix}$	0.3110
V9	$(011)_{\beta} // (0001)_{\alpha}$ $[11\bar{1}]_{\beta} // [11\bar{2}0]_{\alpha}$	$\begin{pmatrix} -0.0414 & 0.0017 & -0.0372 \\ -0.1511 & 0.0395 & -0.1000 \\ 0.0019 & -0.0046 & 0.0199 \end{pmatrix}$	0.1748
V10	$(101)_{\beta} // (0001)_{\alpha}$ $[\bar{1}\bar{1}1]_{\beta} // [11\bar{2}0]_{\alpha}$	$\begin{pmatrix} 0.0535 & 0.0085 & -0.0027 \\ -0.1525 & -0.0507 & -0.0054 \\ -0.0864 & -0.0372 & 0.0152 \end{pmatrix}$	-0.4911
V11	$(\bar{1}01)_{\beta} // (0001)_{\alpha}$ $[111]_{\beta} // [11\bar{2}0]_{\alpha}$	$\begin{pmatrix} -0.0009 & -0.0812 & 0.0284 \\ -0.0184 & -0.0539 & 0.0194 \\ -0.0306 & -0.1435 & 0.0729 \end{pmatrix}$	0.3115
V12	$(01\bar{1})_{\beta} // (0001)_{\alpha}$ $[\bar{1}\bar{1}1]_{\beta} // [11\bar{2}0]_{\alpha}$	$\begin{pmatrix} -0.0198 & -0.1011 & -0.1409 \\ -0.0169 & 0.0199 & -0.0497 \\ 0.0039 & 0.0253 & 0.0578 \end{pmatrix}$	-0.1239



## 4.6 Summary

In this Chapter, the phase transformation and variant selection of intragranular  $\alpha$  during isothermal compression at different temperatures (700 °C and 600 °C) in Ti-7333 alloy was thoroughly investigated by SEM, EBSD and TEM, and analyzed with transformation strain.

For the phase transformation and variant selection of intragranular  $\alpha$  under deformation at 700 °C, the interplay between the lattice strain induced by phase transformation and the imposed compressive strain and the applied compressive load was evidenced as the key factor for  $\alpha$  variant selection. A strong variant selection of the intragranular  $\alpha$  precipitates occurred during the isothermal compression and the selected variants can be classified into two groups (group I and group II), according to their precipitation amount.

For the group I  $\alpha$  precipitates, the precipitation amount is large and the precipitates are agglomerated in the  $\beta$  grains with fewer dislocations. Only 2 variants forming ‘cross-shaped’ clusters are selected. The 2 variants respect the BOR and are interrelated by a 90° rotation around the  $\langle 1\ 1.38\ \overline{2.38}\ 0 \rangle_\alpha$  axis. Such variants consume the maximum amount of deformation work by the external compression. This energy criterion can be further interpreted by the compatibility of the microscopic strain to the macroscopic strain and the shear stress resolved from the external load to the local transformation shear deformation. That is the formation of the selected variants offer the maximum contribution to the imposed compression strain and receive the maximum resolved shear stress on the  $\{1\overline{1}\overline{2}\}_\beta \langle \overline{1}1\overline{1} \rangle_\beta$  shear system for the structure transformation. For the group II  $\alpha$  precipitates, they appear in much smaller numbers and are dispersed in the  $\beta$  grains that are occupied also by large amount of dislocation slip bands. The numbers of the variants in group II are not constant, varying from 2 to 4 from one  $\beta$  grain to another. The selection of the variants still respects the energy criterion for the selection of the group I precipitates and reproduce the same strain and stress compatible characters as the group I precipitates but with restriction from the local stress and strain states imposed by the large amount of dislocations.

For the phase transformation and variant selection of intragranular  $\alpha$  under deformation at 600 °C. The interplay between the lattice strain induced by phase transformation and the macroscopic deformation was evidenced as the key factor for  $\alpha$  variant selection. Under such

a criterion, 4 BOR variants formed during the compression. The formation of the selected variants provided compatible strains to the macroscopic deformation.

The results of the present work reveal in-depth the interplay between the lattice strain of the phase transformation and the imposed macroscopic deformation and the applied external load.

## **Chapter 5 Correlation between microstructure evolution and deformation behavior during isothermal compression**

### **5.1 Introduction**

During hot deformation, two opposite effects - hardening from crystal defect multiplication and crystal reorientation, and softening from defect rearrangement or annihilation via recovery and recrystallization - interweave, resulting in characteristic stress-strain behavior and microstructure evolution. Thus the mechanical responses of the alloys during thermomechanical processes have been a topic of intensive experimental and theoretical investigations for process optimization and microstructure and mechanical property improvement. The hot deformation of metastable  $\beta$  titanium alloys with an initial single  $\beta$  phase in the  $\alpha+\beta$  two phase region has seldom been addressed. The deformation process should be more complicated as the  $\beta$  to  $\alpha$  phase transformation happens naturally in this temperature region. The influence of the transformation, especially the transformation associated lattice deformation, on the mechanical response of the alloy has not yet been reported. In this chapter, a study on the correlation between the microstructure evolution and the hot compression stress-strain behavior was conducted. The effort was made to resolve the underlying mechanisms of the hot deformation behavior of the alloy. Special attentions have been paid to the contribution of the  $\beta$  to  $\alpha$  phase transformation at different deformation stages. This study is expected to offer experimental data for theoretical simulation utilizing various mechanical models.

### **5.2 Experimental**

In this chapter, the Ti-7333 alloy was used. The detailed information on specimen preparation and isothermal compression experiment are given in Section 2.1 (page 18) and Section 2.2 (page 18) in Chapter 2. To obtain accurate and statistical experimental evidence, the in-situ hot compression under the neutron diffraction recording at 700 °C was conducted. The detailed information on the in-situ neutron diffraction compression tests is given in

Section 2.2.3 (page 20) in Chapter 2. The microstructural and crystallographic features were investigated by SEM-EBSD and TEM.

### 5.3 Microstructure of the initial $\beta$ phase

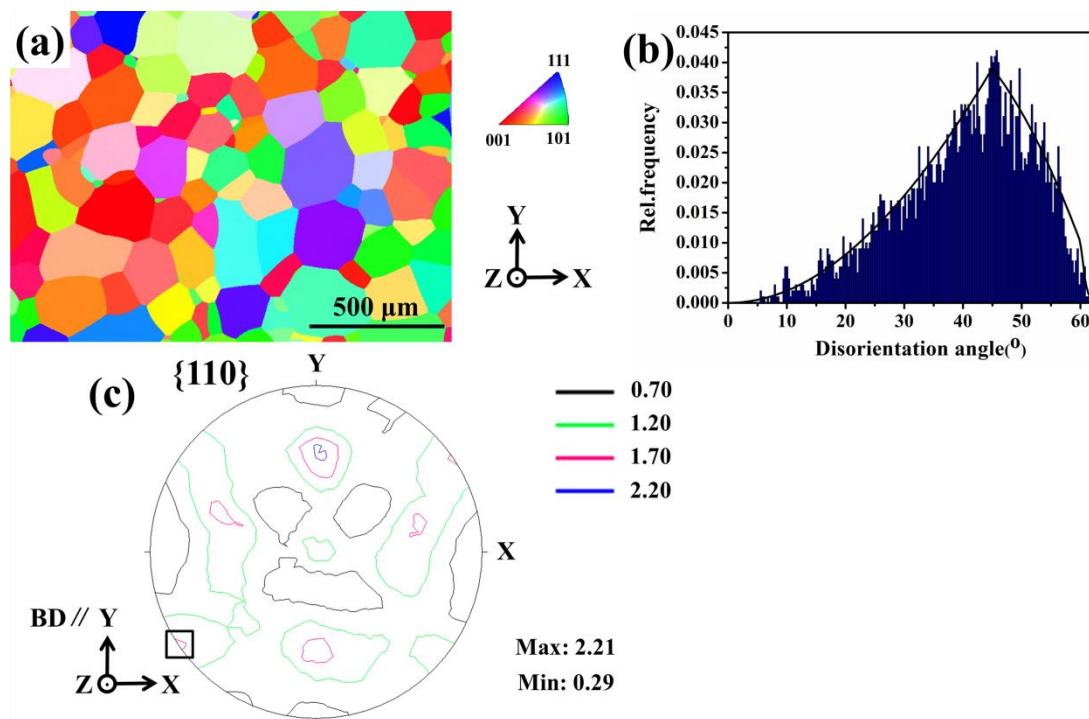


**Fig. 5.1** (a) SEM-EBSD Y axis inverse pole figure (IPF) micrograph of the solution-treated Ti-7333 alloy (Y//axial axis of the cylindrical specimen); (b) the corresponding correlated disorientation angle distribution, where the disorientation angle distribution of theoretical randomly oriented cubic polycrystals is represented with line profile; (c)  $\{110\}_{\beta}$  pole figure measured by neutron diffraction. The  $\{110\}_{\beta}$  reflection used to monitor the phase transformation for intragranular  $\alpha$  is indicated with the black square.

For easy consultation of the initial microstructure of the alloy, the as-solution treated microstructure features were repeated here. Fig. 5.1 shows the EBSD orientation micrograph of the as-solution-treated microstructure of the Ti-7333 with the corresponding correlated disorientation angle distribution. It is seen that the alloy is composed of the single  $\beta$  phase in a form of equiaxed grains with an average size of about  $122 \pm 74 \mu\text{m}$  (Fig. 5.1 (a)). Here the standard deviation indicates the size distribution spread but not the experimental error. The  $\beta$  grains are rather randomly oriented than textured, as shown by the correlated disorientation

angle distribution (Fig. 5.1 (b)). The initial texture is represented by the  $\{110\}_\beta$  pole figure measured by the neutron diffraction in Fig. 5.1 (c). It is seen that the texture is globally random. The uneven distribution of the pole densities is from two factors. The first one is that the grain sizes of the  $\beta$  grains are large. The total number of grains in the measured volume is relatively small (less than 1500). Thus not all the orientation space is occupied by orientations. The second is that the grain sizes are not homogeneous (with a spread of  $\pm 74 \mu\text{m}$ ). Thus the individually located higher pole densities are from large grains. According to the variant selection criteria revealed by the results in Chapter 4, The  $\{110\}_\beta$  planes that can be the Burgers orientation relationship plane for the selected intragranular  $\alpha$  precipitates during the 700 °C deformation can be determined. Thus the orientation of the specimen with respect to the incident beam and the detector can be figured out, as detailed in Appendix. B. In Fig. 5.1 (b), the  $\{110\}_\beta$  reflection used to monitor the phase transformation for intragranular  $\alpha$  is indicated with the black square.

## **5.4 Correlation between microstructure evolution and hot deformation behavior during 700°C compression**

### **5.4.1 Mechanical behavior**

Figure 5.2 shows the true stress-strain curve and the corresponding work hardening rate curve of one specimen unidirectionally compressed to the true strain of 0.35. From the true stress-strain ( $\sigma$ - $\epsilon$ ) curve (in red in Fig. 5.2), it is seen that, as a function of the strain, the stress starts with a linear part, corresponding to an elastic deformation, then undergoes a sudden drop from the peak, the so-called discontinuous yielding, and finally reaches a steady-state. Such a stress-strain behavior of the present alloy is typical of isothermally compressed metastable  $\beta$  Ti alloys [73]. The work hardening rate ( $d\sigma/d\epsilon$ ) (in blue in Fig. 5.2) well reveals the 3 stages of the present deformation. Thus we labeled them State I (elastic deformation), II (discontinuous yielding) and III (steady-state), as indicated in Fig. 5.2. To further reveal the origins of the three deformation stages, the evolution of the deformation microstructure will be focused

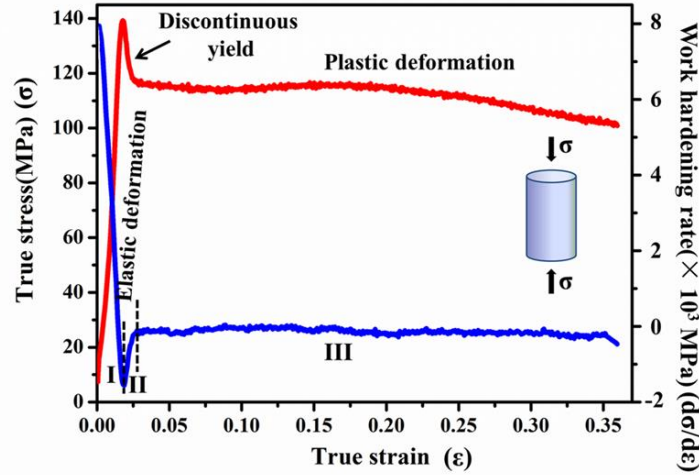


**Fig. 5.2** Stress-strain ( $\sigma$ - $\epsilon$ ) curve (in red) of the Ti-7333 alloy compressed at 700 °C to the true strain of 0.35 and the corresponding work hardening rate-strain ( $d\sigma/d\epsilon$ - $\epsilon$ ) curve (in blue).

## 5.4.2 Correlation between microstructure and deformation behavior

### 5.4.2.1 Stage I and II

Fig. 5.3 and Fig. 5.5 display large scaled microstructures of specimens deformed to the reduction of 1.5% and 3%, with the corresponding stress-strain curves. The former deformation corresponds to the strain at the peak stress just before the discontinuous yielding (Stage I), whereas the latter to the end position of the discontinuous yielding (Stage II).

It is seen that when the specimen was deformed to true strain of 0.015, the  $\beta$  grains still retain the equiaxed shape and there is no obvious grain growth. The average grain size is about  $121 \pm 66 \mu\text{m}$  (Fig. 5.3 (a)) (as noted above, the standard deviation indicates rather the size spread than experimental error). A close examination revealed that a large amount of  $\alpha$  phase is present along the grain boundaries of the  $\beta$  phase but no  $\alpha$  phase is spotted in the  $\beta$  grain interiors (Fig. 5.3 (b)). This evidences that the grain boundary  $\alpha$  precipitates ( $\alpha_{\text{GB}}$ ) were already formed before the end of the Stage I deformation, but the intragranular  $\alpha$  precipitates were not yet formed till then. According to the presence and the morphology of the grain boundary  $\alpha$  precipitates ( $\alpha_{\text{GB}}$ ), the  $\beta$  grain boundaries can be categorized into 3 types: with continuous  $\alpha_{\text{GB}}$ , with discontinuous  $\alpha_{\text{GB}}$  and without  $\alpha_{\text{GB}}$ , as shown in Fig. 5.3 (b). Statistical analysis made on a total area of  $2 \times 1 \text{ mm}^2$  revealed that 92% of the length of the  $\beta$  grain

boundaries is covered by  $\alpha$  precipitates. The majority part of the boundaries are covered by continuous  $\alpha$  (89%), whereas only a very minor portion of the  $\beta$  grain boundaries by discontinuous  $\alpha$  (3%), as shown in Fig. 5.6. This demonstrates that before the end of the first stage of the deformation (Stage I) the  $\beta$  to  $\alpha$  phase transformation happened intensively on the  $\beta$  grain boundaries. Almost all the boundary regions were transformed to the  $\alpha$  phase. As the  $\alpha$  phase is harder than the  $\beta$  phase, the formation of the  $\alpha_{GB}$  strengthens the  $\beta$  grain boundaries.

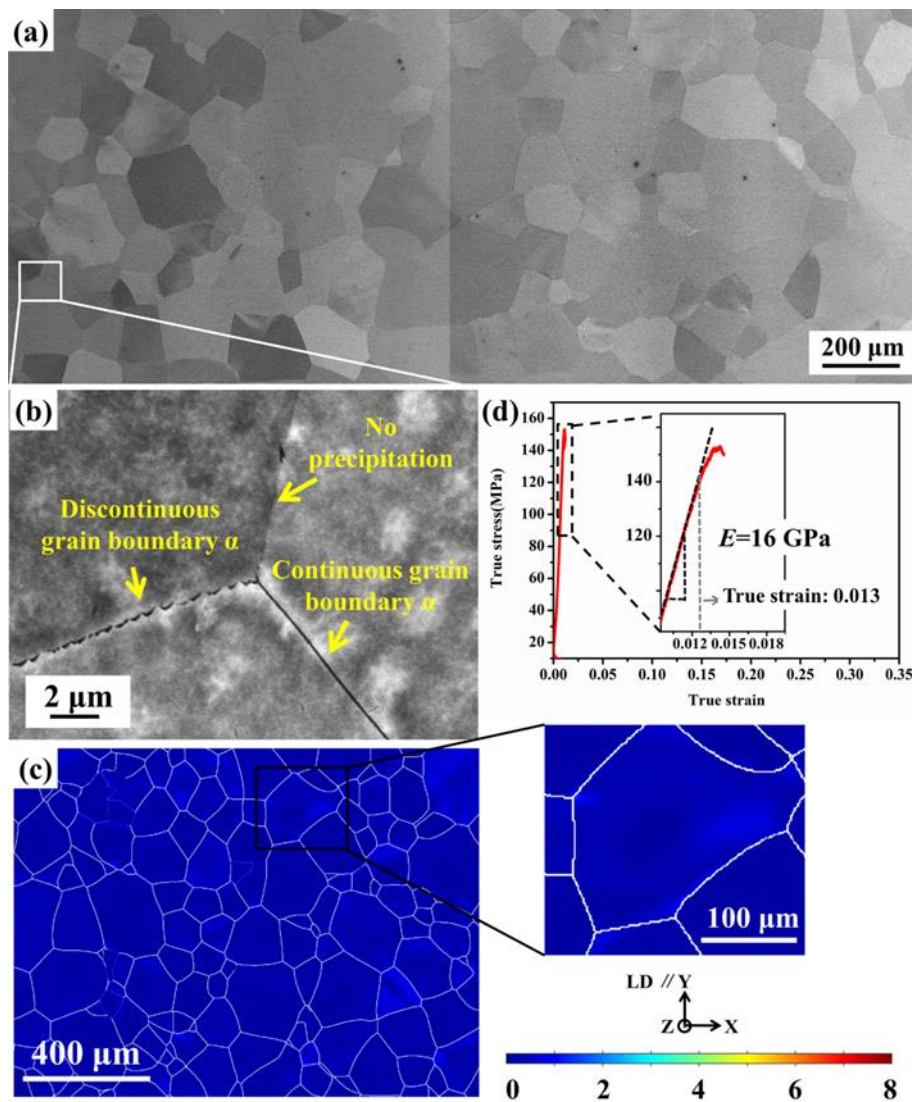


**Fig. 5.3** SEM-BSE and EBSD micrographs of the Ti-7333 deformed at 700°C to the true strain of 0.015 (loading direction is parallel to Y axis), showing (a) the global microstructure, (b)  $\beta$  grain boundaries with continuous and discontinuous  $\alpha$  precipitates, and without  $\alpha$  precipitates, (c) micrograph of Grain Gravity Center Referenced Orientation Deviation (GGCROD) with one example area magnified to show the GGCROD and (d) the

corresponding deformation stress-strain curve corresponding to Stage I. The inset shows the determined Young's modulus and the onset of the stress-strain curve deviating from the linear relation.

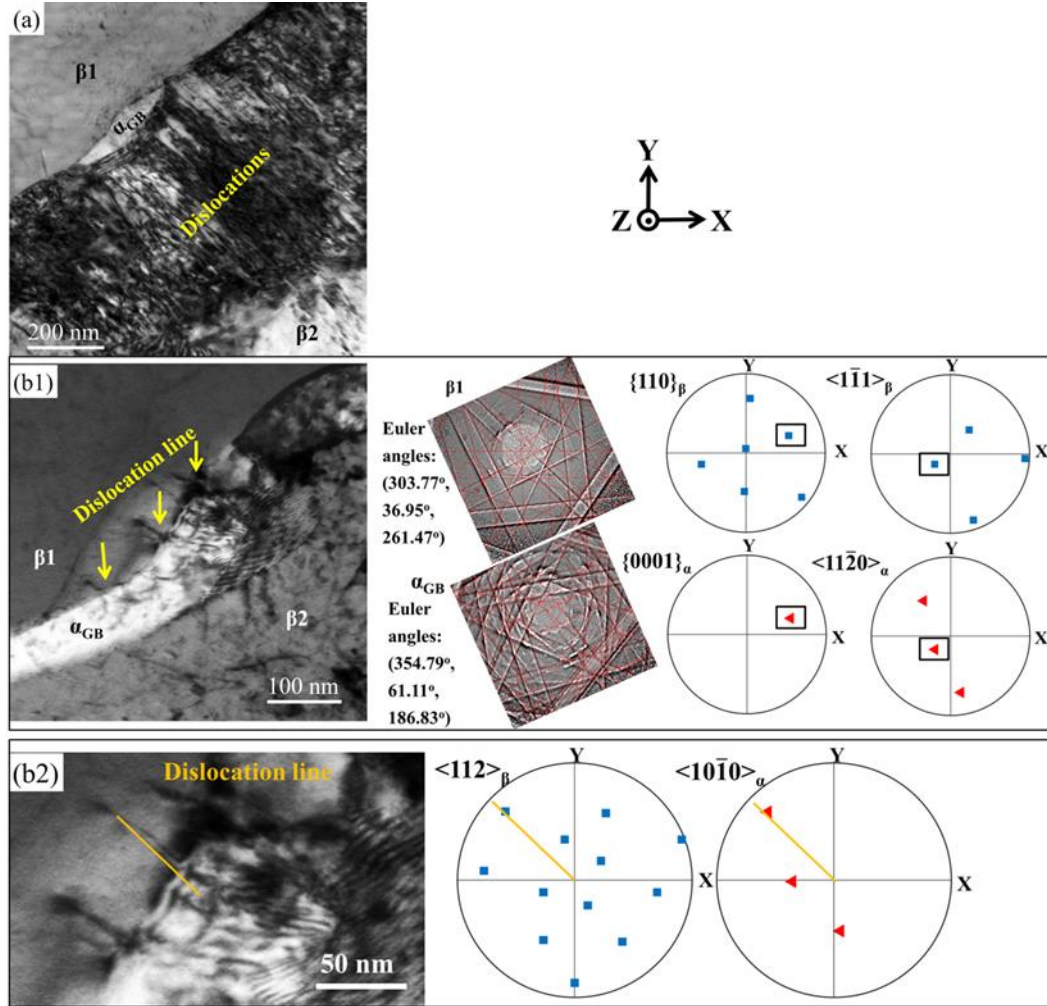


**Fig. 5.4** TEM bright field micrographs of Ti-7333 alloy after being deformed at 700 °C to the true strain of 0.015, showing (a) dislocation band along  $\alpha_{GB}$ ; (b) dislocations cutting through the  $\alpha_{GB}$ . In (b1), example Kikuchi line patterns from grain  $\beta_1$  and  $\alpha_{GB}$  are displayed, together with the BOR plane and direction pole figures. The common poles from the two phases are framed. (b2) shows the magnified image of the dislocation lines in the two phases (indicated with the orange line), together with the line direction pole figures.

From the Grain Gravity Center Referenced Orientation Deviation (GGCROD) analysis result displayed in Fig. 5.3 (c) (Note: the GGCROD map is represented with the disorientation



angle of each EBSD measurement pixel within each recognized grain referenced to the orientation of the pixel at the grain gravity center), one can find that in many  $\beta$  grain boundary regions, especially where near triple junctions, the orientations of these regions are deviated from those of the corresponding grain gravity centers. A deviation as large as  $1\text{--}2^\circ$  can be detected, as shown in the zoomed GGCROD map in Fig. 5.3 (c). This suggests that plastic deformation already started in the linear part of the stress-strain curve. Further TEM examination in the deformed  $\beta$  grain boundary regions at the true strain of 0.015) revealed that such regions contain large amounts of dislocations, organizing into dislocation bands (slip bands), as shown in Fig. 5.4 (a). Further determination using the trace analysis method [119] demonstrated that most of the dislocations are of  $\{110\}_\beta \langle 1\bar{1}1 \rangle_\beta$  edge type. Such dislocations are mobile. Some dislocations present at the phase boundaries are with the one part of the lines in the  $\beta$  phase and the other part in the  $\alpha$  phase, as shown by one example in Fig. 5.4 (b1). Detailed crystallographic analysis showed that the  $\alpha_{GB}$  respects the Burgers orientation relationship (BOR) with the  $\beta$  grain,  $\beta 1$ , as demonstrated with the BOR plane and direction pole figures in Fig. 5.4 (b) (the OR planes and directions are outlined with the black rectangles), with some angular deviations (about  $1.78^\circ$  between the OR planes and about  $2.97^\circ$  between the OR directions). In fact, the BOR plane ( $\{110\}_\beta / \{0001\}_\alpha$ ) and BOR direction ( $\langle 1\bar{1}1 \rangle_\beta / \langle 11\bar{2}0 \rangle_\alpha$ ) in the two phases belong to their slip systems. Further dislocation line orientation analysis demonstrated that the dislocations in  $\beta 1$  (Fig. 5.4 (b1)) are also  $\{110\}_\beta \langle 1\bar{1}1 \rangle_\beta$  edge type with the line vector parallel to  $\langle 1\bar{1}2 \rangle_\beta$ . The dislocation in the  $\alpha_{GB}$  is edge type basal ( $\{0001\}_\alpha \langle 11\bar{2}0 \rangle_\alpha$ ) dislocation with dislocation lines parallel to the  $\langle 10\bar{1}0 \rangle_\alpha$ , as shown in the  $\langle 1\bar{1}2 \rangle_\beta$  and  $\langle 10\bar{1}0 \rangle_\alpha$  pole figures in Fig. 5.4 (b2), where the orange lines indicate the projection of the dislocation lines. These dislocations lie just on the BOR planes in the two phases. Such a result could be from two processes. The one could be that the two phases had reacted independently with the external loading and the slip systems coincident with the BOR systems had been activated simultaneously. The other could be that dislocations had first formed on the BOR system in the  $\beta$  phase and the concentrated stress accumulated at the phase boundaries when they moved to the boundary regions activated the BOR system in the  $\alpha$  phase. The slip transfer conditions have been theoretically analyzed in detailed by Joseph et al. [131] and Zheng et al. [132]. The formation of the large amount of dislocations

near the grain boundary regions evidences that the plastic deformation indeed started in the linear part of the deformation, before the yielding point. To further clarify the possible starting point of the plastic deformation in Stage I, the Young's modulus of the alloy were calculated using the linear part of the curve in Fig. 5.3 (d). The obtained value is about 16 GPa. By comparing the slope of the curve in Stage I with the determined Young's modulus, as shown by Fig. 5.3 (d)-inset, it is found that the curve started to deviate from the linear relation at the strain of about 0.013. Thus the detectable macroscopic plastic deformation happened at the late state of Stage I.

When the specimen was deformed to the true strain of 0.03, the end point of the discontinuous yielding (the end of Stage II), the  $\beta$  grains are still in equiaxed shape but certain grains underwent further grain growth (Fig. 5.5 (a)). Concerning the  $\beta$  to  $\alpha$  transformation, no intragranular  $\alpha$  precipitates were observed and the amount of  $\alpha_{GB}$  stays almost unchanged. Still 92% of the length of the  $\beta$  grain boundaries is covered by the  $\alpha_{GB}$ , as shown in Fig. 5.5(b). However, the amount of discontinuous  $\alpha_{GB}$  is increased from 3% at the reduction of 1.5% to 14% to the reduction of 3% (Fig. 5.6), indicating that more  $\alpha_{GB}$  becomes discontinuous or fragmented. Such fragmentation of the  $\alpha_{GB}$  should be related to the cut-through of the dislocations, as already happened at the true strain of 0.015) (Fig. 5.4 (b)).

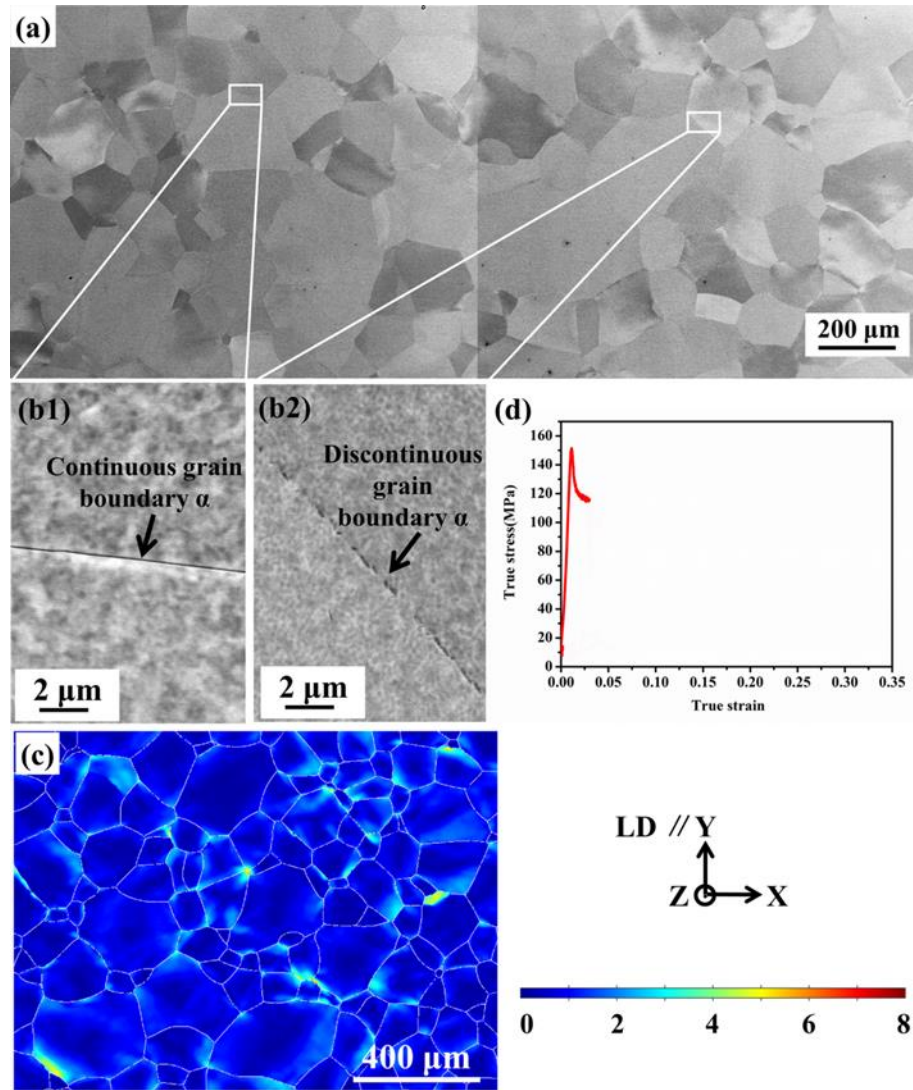


**Fig. 5.5** SEM-BSE and EBSD micrographs of the Ti-7333 deformed at 700 °C to the true strain of 0.03 (loading direction is parallel to Y axis), showing **(a)** the global microstructure, **(b1)** and **(b2)** the  $\beta$  grain boundaries with continuous and discontinuous  $\alpha$  precipitates and without  $\alpha$  precipitates, **(c)** micrograph of Grain Gravity Center Referenced Orientation Deviation (GGCROD) and **(d)** the corresponding deformation stress-strain curve.

As more than 90% of the boundary length is covered by  $\alpha_{GB}$ , the movement of the dislocations across  $\beta$  grain boundaries has to cut through the  $\alpha_{GB}$ , and as a result, the continuous  $\alpha_{GB}$  is fragmented. Clearly, the fragmentation of the continuous  $\alpha_{GB}$  weakens the strengthening effect of the  $\alpha_{GB}$  to the  $\beta$  grain boundaries. Furthermore, almost all the  $\beta$  grain boundary regions are deformed, as evidenced by the GGCROD micrograph in Fig. 5.5 (c). The orientations of the  $\beta$  regions near the grain boundaries are largely deviated ( $2.5^\circ$ - $5^\circ$ ) from

those of their gravity center, inferring the intensive formation of dislocations. Therefore the rapid stress drop during the discontinuous yielding in Stage II should be related to the fragmentation of the  $\alpha_{GB}$  and the formation of the dislocations in a collective avalanche-like way near the  $\beta$  grain boundary areas. The present result provides more detailed experimental evidences to the assertion that the discontinuous yielding in Ti alloys is from the formation of the large quantities of mobile dislocations. Moreover, the fragmentation of the  $\alpha_{GB}$  softened the material at  $\beta$  grain boundary regions and thus contributes also to the yielding.

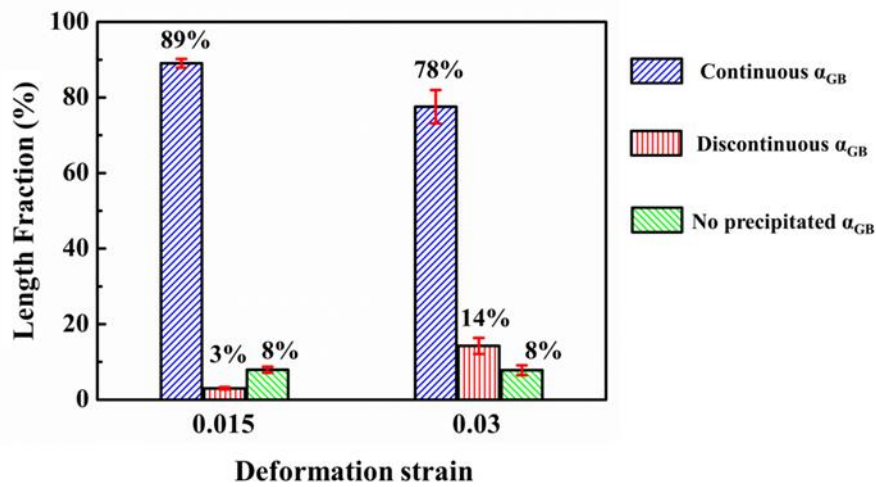


**Fig. 5.6** Length percentages of  $\beta$  grain boundaries with continuous  $\alpha_{GB}$ , with discontinuous  $\alpha_{GB}$  and without  $\alpha_{GB}$  in the specimens deformed to the respective true strain of 0.015) and true strain of 0.03). The data are collected from an area of  $2 \times 1 \text{ mm}^2$ .

#### 5.4.2.2 Stage III

Fig. 5.7 shows the neutron diffraction intensity evolutions of the  $\{110\}_{\beta}$  reflection from the  $\beta$  phase and the  $\{0002\}_{\alpha}$  reflection from the  $\alpha$  phase during the compression. It should be mentioned that the diffraction intensity of the  $\alpha$  phase is from the intragranular  $\alpha$ . The experimental setup allowing such detection is detailed in Appendix B. It is seen that the intragranular  $\alpha$  started to precipitate with detectable amount at the strain of 0.14 (corresponding to 140s of the isothermal holding and in the middle of the steady stress-strain state, Stage III). After the transformation, the intensity of the diffraction peak of the  $\alpha$  phase presents a very slow increase till the true strain of 0.2) and stays stable afterwards, meaning that the transformation started very rapidly at the beginning and finished at strains of about

0.20. Correspondingly in the stress-strain curve, the stress increases very slightly at 0.14 but decreases from 0.20. The slight upturning of the stress-strain curve in Stage III is coincident with the formation of the intragranular  $\alpha$  precipitates.

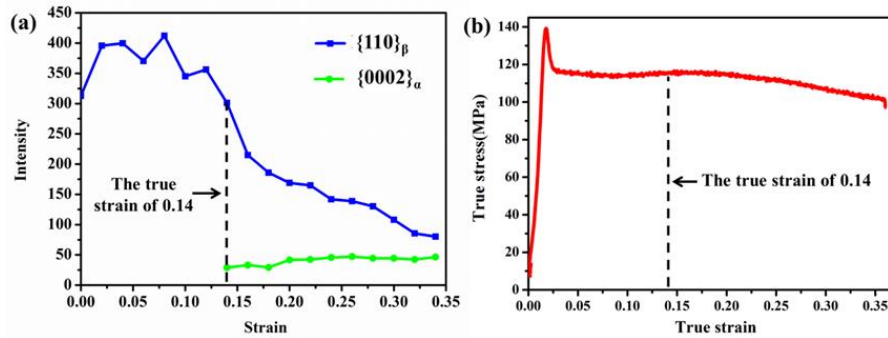


**Fig. 5.7** Evolution of the diffraction intensities of the  $\{110\}_{\beta}$  reflection of the  $\beta$  phase and the  $\{0002\}_{\alpha}$  reflection of the  $\alpha$  phase during the isothermal compression.

Fig. 5.8 presents the deformed microstructures of the specimen compressed to the true strain of 0.35) corresponding to the end point of Stage III in the stress-strain curve in Fig. 5.2. It is seen that after the deformation to the reduction of 30%, most of the  $\beta$  grains are elongated in a direction either perpendicular to the compression direction or inclined, to some extent, to this direction. Furthermore,  $\alpha$  phase is intensively precipitated in the  $\beta$  grains. However, the precipitation amount in different  $\beta$  grains is very heterogeneous. According to the precipitation amount, the  $\beta$  grains are further classified into two types, Type I and Type II. For the type I grains, as outlined with the yellow lines in Fig. 5.8 (a), there appear almost no or very slight amount of  $\alpha$  precipitates. A magnified micrograph of such grains is displayed in Fig. 5.8 (b). However, for the type II grains, as outlined with the blue lines in Fig. 5.8 (a), large amount of  $\alpha$  precipitates appear in the  $\beta$  grains, especially in the grain interiors. A magnified micrograph of such grains is displayed in Fig. 5.8 (c). The area percentages of the two kinds of grains were measured in a cross section area of  $1.7 \times 3 \text{ mm}^2$ . This area cuts the whole homogeneous deformation zone in the sample. The results showed that the area percentage for the type I grains is about 54%, and that for the type II grains is about 46%. Detailed microstructural and crystallographic examination of the  $\alpha$  precipitates in the interiors of the type II  $\beta$  grains revealed that the  $\alpha$  precipitates are in plate-shape (Fig. 5.8 (c)-insert)

and respect the BOR with the surrounding  $\beta$  matrix. In each type II grain, only two  $\alpha$  variants are detected and the two variants are disoriented by  $90^\circ$  around the  $\langle 1\ 1.38\ \overline{2.38}\ 0 \rangle_\alpha$ , forming cross shaped clusters. Such a crystallographic character of the  $\alpha$  precipitates was verified in all the type II  $\beta$  grains in the whole cross section of the deformed zone in the sample ( $1.7 \times 3\text{ mm}^2$ ) and found to be reproduced in all the type II grains. Thus the results are statistically relevant. The deformation of the  $\beta$  grains was further analyzed, using the measured EBSD data, and represented with the micrograph of Grain Gravity Center Referenced Orientation Deviation (GGCROD), as shown in Fig. 5.8 (d). It is seen that the most deformed regions are still located near the  $\beta$  grain boundaries, especially the triple junctions, with the maximum disorientation (in angle) up to  $19^\circ$ . Compared with the deformation situation shown in Fig. 5.3 (c) (true strain of 0.015) and in Fig. 5.5 (c) (true strain of 0.35), the deformed regions in each  $\beta$  grain extend from the grain boundary regions toward the grain interiors, especially in the type I  $\beta$  grains. For the type II grains the disoriented regions are mainly located in the “mantle” part of the  $\beta$  grains where almost no  $\alpha$  precipitates appear.

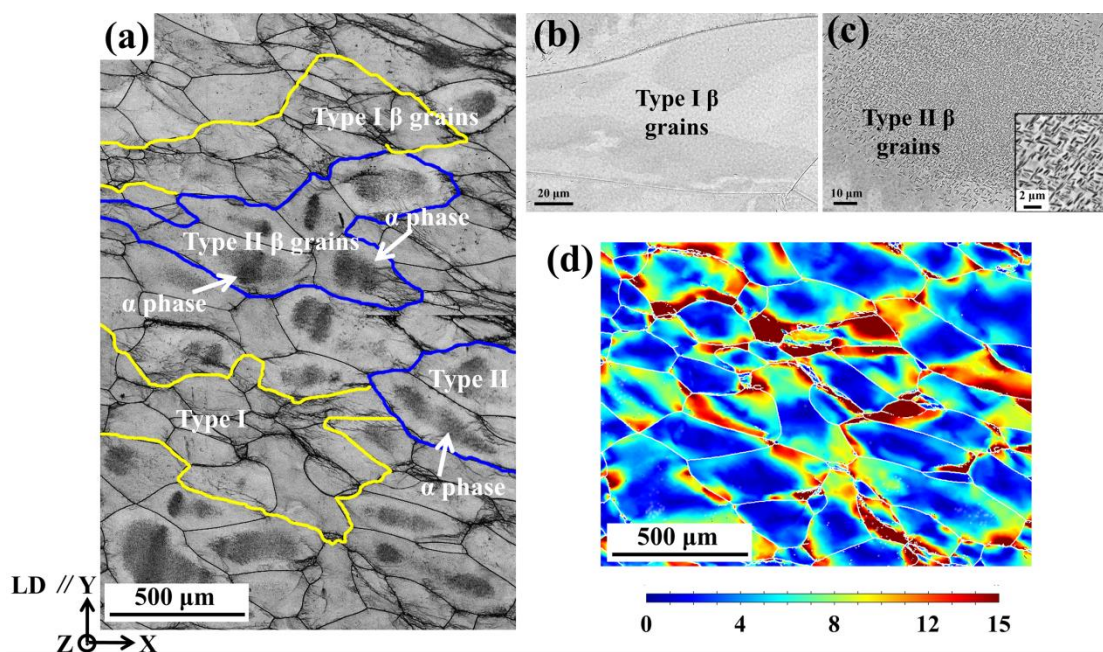


**Fig. 5.8** (a) EBSD band contrast micrograph of the Ti-7333 alloy after unidirectional compression at  $700^\circ\text{C}$  (loading direction is parallel to Y axis) to the true strain of 0.35. The  $\beta$  grains are in light gray and the  $\alpha$  phase are in dark gray, as shown in the figure. The black



lines represent the  $\beta$  grain boundaries. **(b)** A magnified BSE image showing type I  $\beta$  grains with few  $\alpha$  precipitates. **(c)** A magnified BSE image showing type II  $\beta$  grains with  $\alpha$  precipitates in the grain interiors. **(d)** Grain Gravity Center Referenced Orientation Deviation (GGCROD) micrograph.

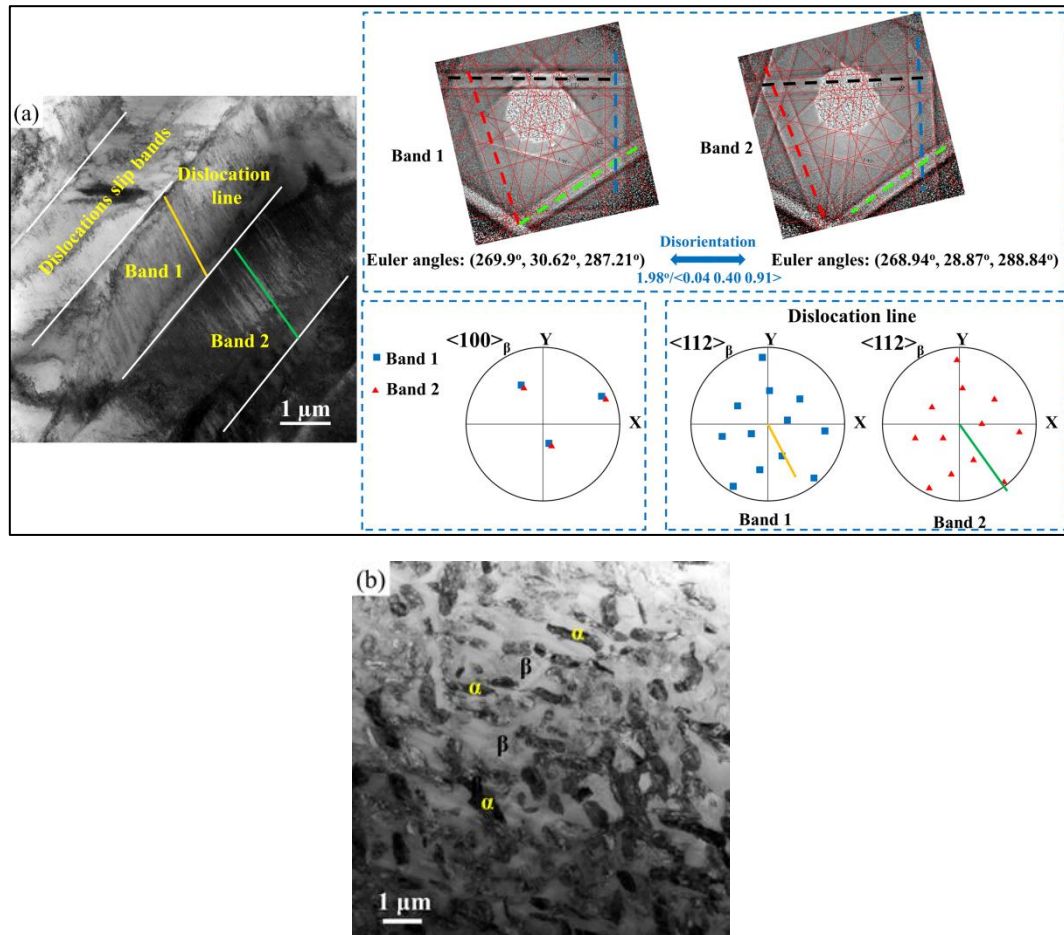


**Fig. 5.9** TEM bright field micrographs of Ti-7333 alloy after being compressed at 700 °C to the true strain of 0.35, **(a)** showing the dislocations in slip bands in the type I  $\beta$  grains where there are almost no  $\alpha$  precipitates and **(b)** showing the large amount of  $\alpha$  precipitates in type II  $\beta$  grains. In (a), example Kikuchi line patterns from Bands 1 and 2 are displayed, together with the  $\langle 100 \rangle_{\beta}$  direction pole figure to show that the band regions are slightly disoriented. The dislocation lines in the two bands are also indicated with the  $\langle 112 \rangle_{\beta}$  direction pole figures, showing that the dislocations in the bands are of the same type but are crystallographic variants.

Further TEM examinations revealed that in the type I  $\beta$  grains there exists large amount

of dislocations, as shown in Fig. 5.9 (a). The dislocations are organized in bands (as outlined with the white lines in the figure) and within each band the dislocation lines are aligned roughly in the same direction (as indicated with the orange and green lines). Orientation analysis using the acquired Kikuchi patterns from different slip bands, for example Bands 1 and 2 in Fig. 5.9 (a), demonstrated that the slip bands are slightly disoriented (about  $2^\circ$ ), as shown by the  $\langle 100 \rangle_\beta$  pole figure. Further determination using the method developed by the ref. [119] confirmed that the dislocations are still of the  $\{110\}_\beta \langle 1\bar{1}1 \rangle_\beta$  edge type with the dislocation lines parallel to the  $\langle 1\bar{1}2 \rangle_\beta$  direction. The dislocations in different bands are of the same type but are crystallographic variants, as shown by the  $\langle 1\bar{1}2 \rangle_\beta$  pole figures in Fig. 5.9 (a), where the projections of the dislocations in Bands 1 and 2 are indicated with the consistent color lines as those in the TEM bright field micrograph. It is found that such slip bands go through the entire  $\beta$  grains (type I). It is worth mentioning that no  $\{112\}_\beta \langle 11\bar{1} \rangle_\beta$  dislocations were evidenced in the present alloy. The absence of this type of dislocations is consistent with what reported in the literature that the  $\{112\}_\beta \langle 11\bar{1} \rangle_\beta$  slip system in BCC crystals are more easily activated at low deformation temperatures than at high temperatures [133]. The formation of the slip bands should be related to the temperature effect. Obviously recovery occurred intensively with the deformation. However, no recrystallized grains were detected, suggesting that there is no occurrence of recrystallization during the present compression to the true strain of 0.35. In contrast, in the type II grains no dislocation bands were found existing in the zones where the  $\alpha$  precipitates were intensively formed, as shown in Fig. 5.9 (b), indicating that the deformation mechanisms are different in the two types of grains. In the former the deformation is controlled by dislocation activity and in the latter the deformation is accommodated mainly by phase transformation.



**Table 5.2** Displacement gradient tensor of  $\{110\}_\beta \langle \bar{1}\bar{1}1 \rangle_\beta$  slip and that of  $\beta$  to  $\alpha$  phase transformation expressed in Burgers Orientation Relationship (BOR) coordinate system: ( *i.e.*

$i // [\bar{1}\bar{1}\bar{2}]_\beta, j // [\bar{1}1\bar{1}]_\beta$  and  $k // [110]_\beta$  ).

Deformation system	Displacement gradient tensor
$\{110\}_\beta \langle \bar{1}\bar{1}1 \rangle_\beta$	$\begin{pmatrix} 0 & 0 & 0 \\ 0 & 0 & \pm 0.3772 \\ 0 & 0 & 0 \end{pmatrix}$
$\beta$ to $\alpha$ transformation	$\begin{pmatrix} -0.0416 & 0 & 0 \\ -\mathbf{0.1844} & 0.0434 & 0 \\ 0 & 0 & 0.0189 \end{pmatrix}$

Obviously the two types of  $\beta$  grains contribute to the external deformation in different ways. For the type I grains, the contribution is made mainly by the  $\{110\}_\beta \langle \bar{1}\bar{1}1 \rangle_\beta$  dislocation slip. Thus their crystallographic orientations ensure the  $\{110\}_\beta \langle \bar{1}\bar{1}1 \rangle_\beta$  slip system to be in the favorable activation position to the external load. For the type II  $\beta$  grains, the contribution is mainly made by the lattice deformation from the  $\beta$  to  $\alpha$  transformation, as the structure transformation involves a large shear in the  $\{1\bar{1}\bar{2}\}_\beta \langle \bar{1}1\bar{1} \rangle_\beta$  system and some normal strain components, as shown in Table 5.2. For comparison, the displacement gradient tensor of the  $\{110\}_\beta \langle \bar{1}\bar{1}1 \rangle_\beta$  slip expressed in the same reference system (BOR system  $i // [\bar{1}\bar{1}\bar{2}]_\beta, j // [\bar{1}1\bar{1}]_\beta, k // [110]_\beta$ ) is also given in the table. It should be mentioned that the value in the displacement gradient tensor of the  $\{110\}_\beta \langle \bar{1}\bar{1}1 \rangle_\beta$  slip is obtained by dividing the magnitude of the Burgers Vector ( $b$ ) with the interplanar spacing of the  $\{110\}_\beta$  slip planes in the  $\beta$  phase. The value is only indicative and far from the reality, as in the real case the value in the tensor is dislocation density dependent. The crystallographic orientations of the type II  $\beta$  grains should allow the  $\{1\bar{1}\bar{2}\}_\beta \langle \bar{1}1\bar{1} \rangle_\beta$  system in the favorable position to be activated by the external load. To verify these assertions, the orientation of the two types of  $\beta$  grains measured from the sample area of  $1.7 \times 3 \text{ mm}^2$  that corresponds to the whole cross section area of the deformed zone were analyzed and represented in the orientation space (Euler angle space). Fig. 5.10 shows the  $\phi_2$  sections of the measured orientations of the two types of  $\beta$  grains and the calculated resolved shear stress of the unitary external compressive load on the respective  $\{110\}_\beta \langle \bar{1}\bar{1}1 \rangle_\beta$  and  $\{1\bar{1}\bar{2}\}_\beta \langle \bar{1}1\bar{1} \rangle_\beta$  systems of the randomly oriented  $\beta$  grains ( $2.85 \times 10^6$ ) that are distributed in the whole orientation space. The calculated resolved shear stress of each Euler orientation is

shown with the highest one among the system families. The random  $\beta$  orientations were generated using the algorithm proposed by Morawiec [134]. Comparing Fig. 5.10 (a) with Fig. 5.10 (b), and Fig. 5.10 (c) with Fig. 5.10 (d), one can find that the type I  $\beta$  grains are indeed oriented with one of their  $\{110\}_{\beta}<\bar{1}\bar{1}\rangle_{\beta}$  slip systems in the favorable position for activation, i.e., the external load resolves a maximum shear stress on the system, whereas the type II  $\beta$  grains are oriented with one of their  $\{1\bar{1}\bar{2}\}_{\beta}<\bar{1}\bar{1}\rangle_{\beta}$  shear systems in the favorable position for activation.

To evaluate the contribution possibilities of the two deformation modes ( $\{110\}_{\beta}<\bar{1}\bar{1}\rangle_{\beta}$  slip and the phase transformation) of the examined  $\beta$  grains, the displacement gradient tensors of the lattice transformation strain from the  $\beta$  matrix to the two selected  $\alpha$  variants in one example  $\beta$  grain having the maximum resolved shear stress for the  $\{1\bar{1}\bar{2}\}_{\beta}<\bar{1}\bar{1}\rangle_{\beta}$  system and those of the dislocation slip of one example  $\beta$  grain with the maximum absolute resolved shear stress for  $\{110\}_{\beta}<\bar{1}\bar{1}\rangle_{\beta}$  slip are further expressed in the sample coordinate system (X-Y-Z, as shown in the figures of the micrographs (Fig. 5.1, 5.3 , 5.5 and 5.8)) where the compression axis is parallel to Y and one example is given in Table 5.3. It should be mentioned that the tensors displayed in the table are from the systems receiving the maximum resolved shear stress. In the tensors, the  $\varepsilon_{22}$  component is very indicative for the strain of the systems contributed to the macroscopic compression. The negative  $\varepsilon_{22}$  means that the lattice deformation (either by slip or phase transformation) produces contraction in the macroscopic compression direction. It is seen that the formation of the two  $\alpha$  variants in the type II  $\beta$  grain makes positive contribution to the macroscopic compression. However for the  $\{110\}_{\beta}<\bar{1}\bar{1}\rangle_{\beta}$  slip, it can happen in two opposite directions, the one making positive contribution to the macroscopic deformation and the other one being opposite. The opposite ones are to accommodate local deformation. The two kinds of shear systems demonstrate quite different contribution to the macroscopic deformation. For the formation of the selected intragranular  $\alpha$  precipitates by phase transformation, the activation of the shear system ( $\{1\bar{1}\bar{2}\}_{\beta}<\bar{1}\bar{1}\rangle_{\beta}$  systems) is uni-directional. The deformation thus provided is compatible with the macroscopic compression. However, for the  $\{110\}_{\beta}<\bar{1}\bar{1}\rangle_{\beta}$  slip, it is bi-directional. The deformation provided can either contribute to the macroscopic deformation or to the local deformation, even though it is incompatible to the macroscopic deformation.

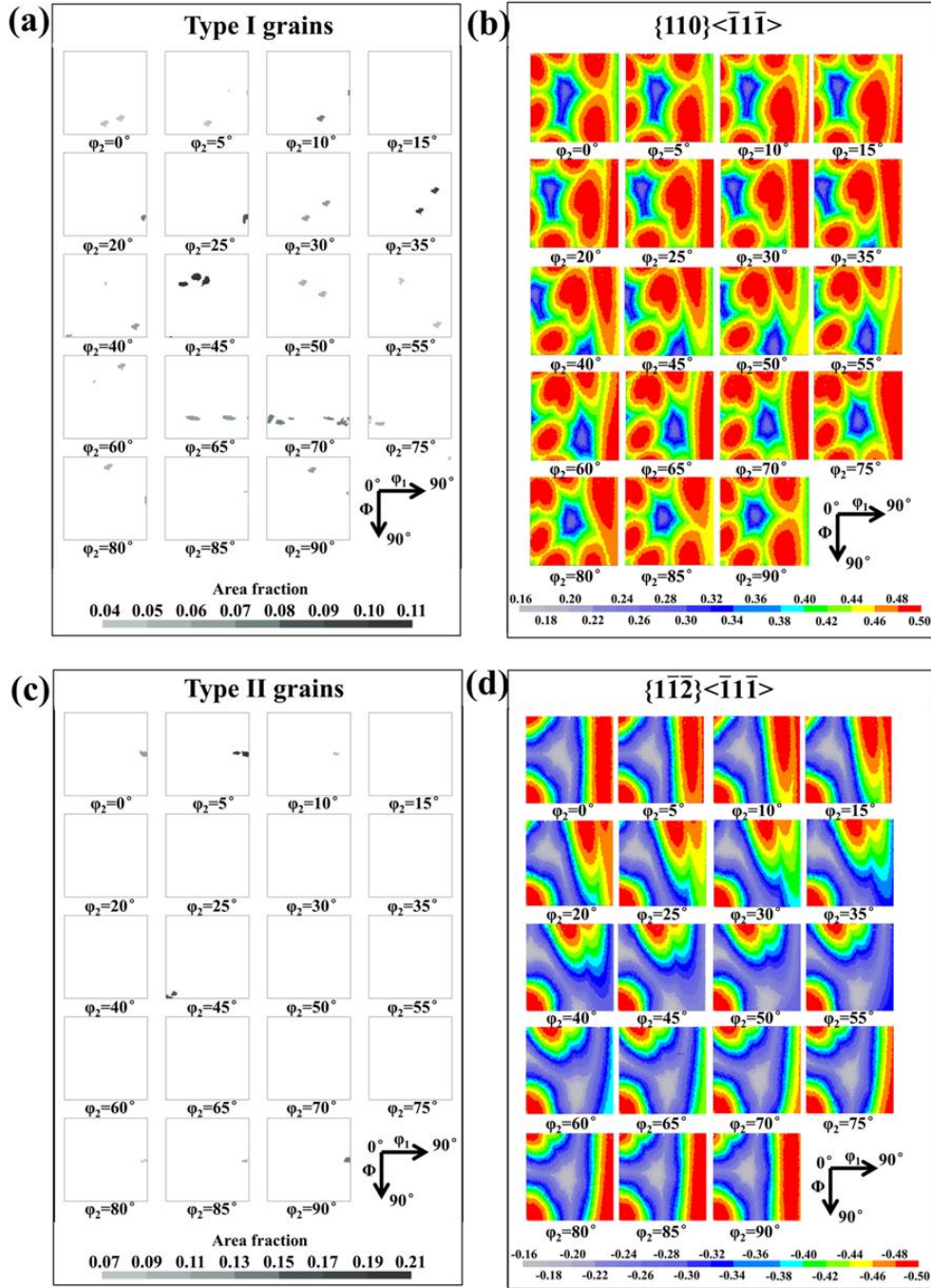


**Fig. 5.10** (a) and (c)  $\phi_2$  sections of the measured orientations of the respective type I and type II  $\beta$  grains normalized with the total areas of the respective type of  $\beta$  grains and (b) and (d) calculated resolved shear stress of the unitary external compressive load on the respective  $\{110\}_\beta\langle 111 \rangle_\beta$  and  $\{112\}_\beta\langle 111 \rangle_\beta$  systems of randomly oriented  $\beta$  grains ( $2.85 \times 10^6$ ) that are distributed in the whole orientation space. The resolved shear stress shown for each Euler orientation is that of the system with highest value among the shear system families considered.

**Table 5.3** Displacement gradient tensors of two  $\alpha$  precipitates in one example of type I  $\beta$  grain and that of  $\{110\}_{\beta} \langle \bar{1}\bar{1}1 \rangle_{\beta}$  slip system of one example of type II  $\beta$  grain expressed in the sample X-Y-Z coordinate system. The compression is along Y axis.

Precipitates No.	Displacement gradient tensor
A	$\begin{pmatrix} 0.0238 & 0.0279 & 0.0225 \\ -0.0224 & -0.0999 & -0.0812 \\ 0.0216 & 0.0962 & 0.0952 \end{pmatrix}$
B	$\begin{pmatrix} 0.0945 & -0.0757 & -0.0152 \\ 0.1010 & -0.0989 & -0.0182 \\ -0.0308 & 0.0319 & 0.0234 \end{pmatrix}$
$(0\bar{1}1)_{\beta}[\bar{1}\bar{1}\bar{1}]_{\beta}$	$\begin{pmatrix} 0.0032 & -0.0276 & 0.0211 \\ 0.0214 & -0.1824 & 0.1393 \\ 0.0275 & -0.2347 & 0.1792 \end{pmatrix}$
$(0\bar{1}1)_{\beta}[111]_{\beta}$	$\begin{pmatrix} -0.0032 & 0.0276 & -0.0211 \\ -0.0214 & 0.1824 & -0.1393 \\ -0.0275 & 0.2347 & -0.1792 \end{pmatrix}$

These results demonstrate that the steady stress-strain behavior of the alloy is rooted from the different contributions of the two types of  $\beta$  grains. For the type I grains, the hardening from the multiplication of the dislocations is balanced by the rearrangement of the dislocations to the soft configurations (the slip bands in the present work) through dislocation movement, as the activation energy of the dislocation slip is decreased at elevated temperatures [135, 136]. For the type II  $\beta$  grains, the formation of the intragranular  $\alpha$  precipitates should strengthen the type II  $\beta$  grain interiors. As they form intensively around the true strain of 0.14, as shown in Fig. 5.7, the slight hardening shown by the stress-strain curve in Fig. 5.2 is due to the formation of the intragranular  $\alpha$  precipitates in the type II  $\beta$  grains. With the further progress of the deformation from the strain of about 0.2, a slight but obvious softening can be seen in the stress-strain curve in Fig. 5.2. The softening is mainly related to the dislocation rearrangement, but not by the formed intragranular  $\alpha$  precipitates, as they did not show any fragmentation or spheroidization until the strain of 0.35.

## 5.5 Correlation between microstructure evolution and hot deformation behavior during 600°C compression

### 5.5.1 Mechanical behavior

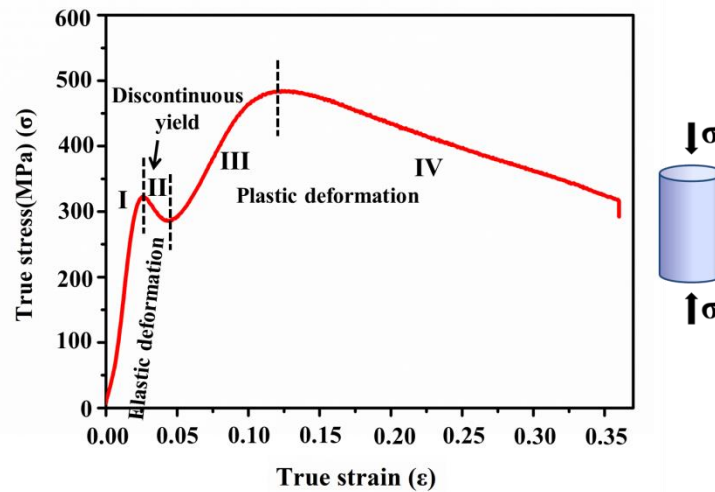


**Fig. 5.11** True stress-strain ( $\sigma$ - $\epsilon$ ) curve of the Ti-7333 alloy compressed at 600 °C to the true strain of 0.35.

Figure 5.11 shows the true stress-strain curve of one specimen unidirectionally compressed to the true strain of 0.35 at 600 °C. From the true stress-strain ( $\sigma$ - $\epsilon$ ) curve, it is seen that, as a function of the strain, the stress starts with a near linear part, corresponding to an elastic deformation, and then undergoes a sudden drop from the peak, the so-called discontinuous yielding. This is consistent with the flow stress behavior of the alloy compressed at 700 °C. The only difference is that the yielding at 600 °C happened at a stress much higher than that at 700 °C (Fig. 5.2). These flow stress behavior are labeled as Stage I, corresponding to the elastic deformation, and Stage II, corresponding to the discontinuous yielding. After the discontinuous yielding, the compression of this alloy presents a plastic feature. However, different from that at 700 °C (steady-state), the plastic deformation at 600 °C demonstrate first a hardening process and then a softening process, showing a different plastic behavior. The hardening part is labeled as Stage III, and the softening part Stage IV.

### 5.5.2 Correlation between microstructure and deformation behavior

Fig. 5.12 and Fig. 5.13 display large scaled microstructures of specimens deformed to the true strains of 0.025 and 0.04, respectively. The former corresponds to the end strain of Stage I, just before the discontinuous yielding, whereas the latter to the end position of the discontinuous yielding (Stage II).

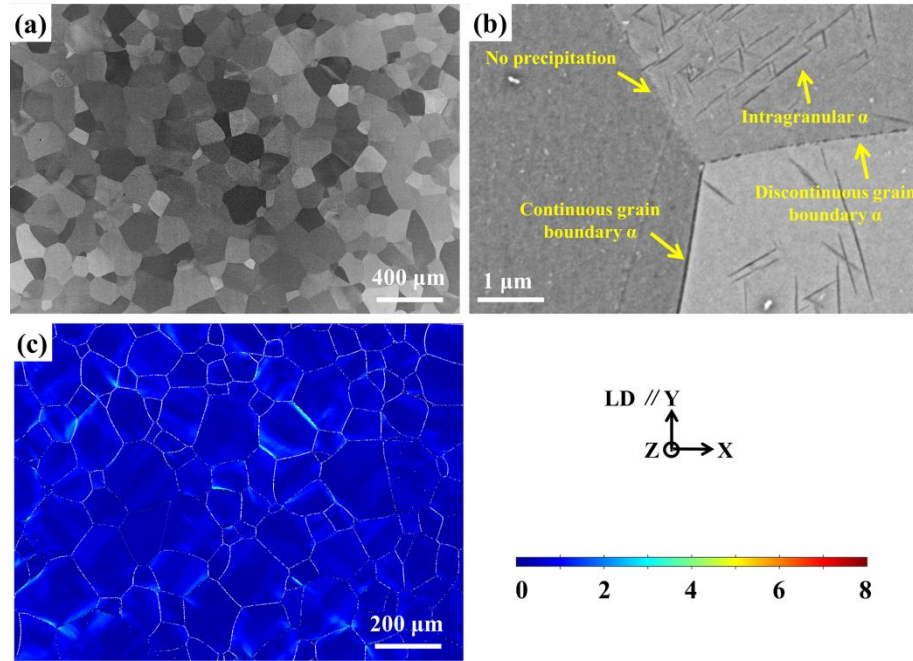


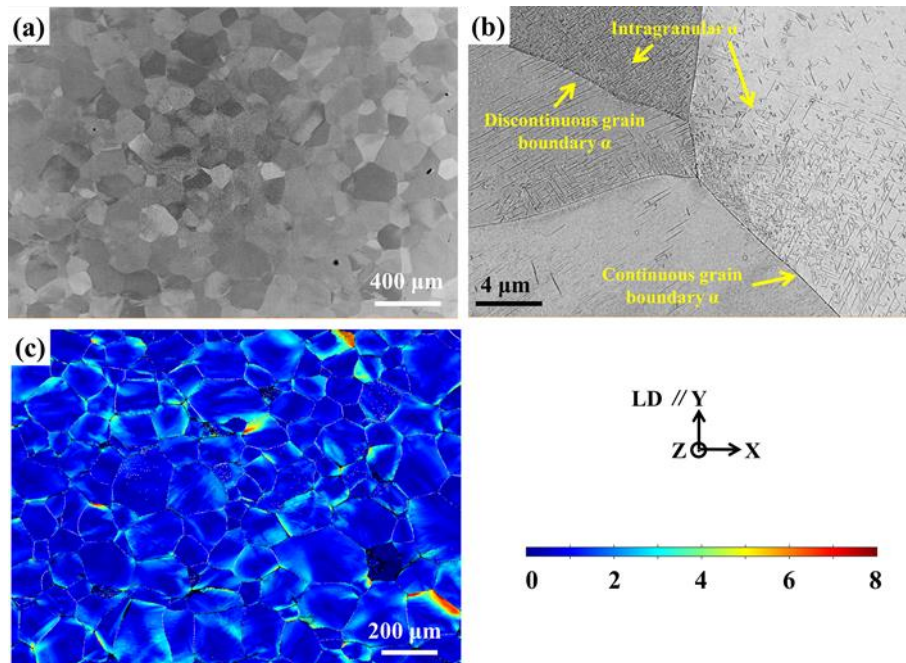
**Fig. 5.12** SEM-BSE and EBSD micrographs of the Ti-7333 deformed at 600°C to the true strains of 0.025 (loading direction is parallel to Y axis), showing (a) the global microstructure, (b)  $\beta$  grain boundaries with continuous and discontinuous  $\alpha$  precipitates, and without  $\alpha$  precipitates and intragranular  $\alpha$  precipitates, and (c) micrograph of Grain Gravity Center Referenced Orientation Deviation (GGCROD).

For the specimen deformed to the strain of 0.025, the  $\beta$  grains still retain the equiaxed shape. Further microstructures examination revealed that a large amount of  $\alpha$  phase exists along the grain boundaries of the  $\beta$  phase. This suggests that the grain boundary  $\alpha$  precipitates ( $\alpha_{GB}$ ) were already formed at the end of the Stage I deformation. According to the presence and the morphology of the  $\alpha_{GB}$ , the grain boundaries can also be categorized into 3 types: with continuous  $\alpha_{GB}$ , with discontinuous  $\alpha_{GB}$  and without  $\alpha_{GB}$ , as shown in Fig. 5.12 (b). Global examination demonstrated that more than 90% of the length of the  $\beta$  grain boundaries is



covered by  $\alpha$  precipitates (as indicated in Fig. 5.14). This implies that almost all the grain boundaries were transformed to the  $\alpha$  phase. Moreover, in addition to the precipitation of  $\alpha_{GB}$ , small amount of intragranular  $\alpha$  precipitates were formed near the grain boundary regions during the Stage I deformation, as shown in Fig. 5.12 (b). Global examination revealed that the amount of the intragranular  $\alpha$  precipitates in the  $\beta$  grains is not constant. It changes from grain to grain. No  $\alpha$  precipitates were formed in the interior region of the  $\beta$  grains. It is known that the  $\alpha$  phase is harder than the  $\beta$  phase. Thus the formation of the  $\alpha$  precipitates (including  $\alpha_{GB}$  and intragranular  $\alpha$  precipitates located near grain boundaries) strengthens the  $\beta$  grain boundary regions.

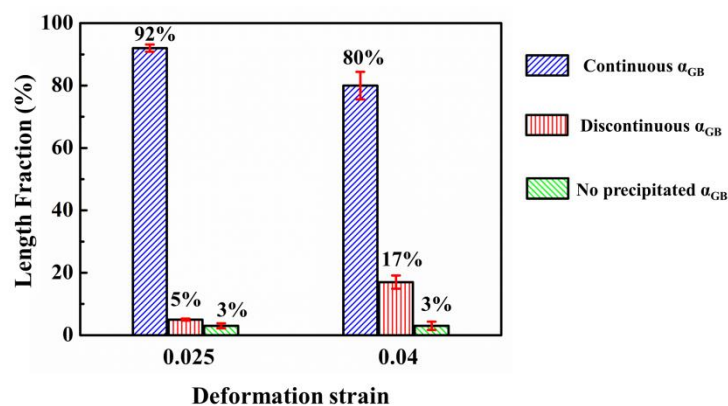
To further analyze the microstructural response to the deformation in Stage I, the Grain Gravity Center Referenced Orientation Deviation (GGCROD) analysis was conducted and the GGCROD micrograph is shown in Fig. 5.12 (c). It is seen that in many  $\beta$  grain boundary regions, especially where near the triple junctions, the orientations of these regions are deviated from those of the corresponding grain gravity centers. A deviation as large as  $2-4^\circ$  can be detected. Such orientation deviation is related to the formation of the intragranular  $\alpha$  precipitates near the boundary regions, as shown in Fig. 5.12(b).



**Fig. 5.13** SEM-BSE and EBSD micrographs of Ti-7333 deformed at 600°C to the true strain of 0.04 (loading direction is parallel to Y axis), showing (a) the global microstructure, (b)  $\beta$

grain boundaries with continuous and discontinuous  $\alpha$  precipitates, and without  $\alpha$  precipitates and intragranular  $\alpha$  precipitates and (c) micrograph of Grain Gravity Center Referenced Orientation Deviation (GGCROD).

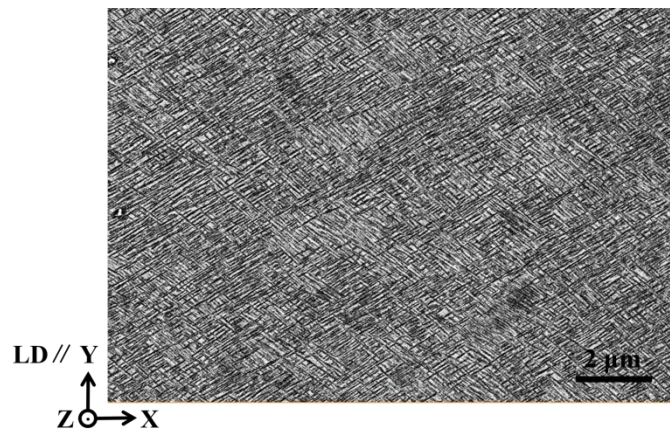
When the specimen was deformed to the strain of 0.04, the end point of the discontinuous yielding (the end of Stage II), the  $\beta$  grains are still in equiaxed shape. The global and local microstructure examination revealed that still more than 90% of the length of the  $\beta$  grain boundaries is covered by the  $\alpha_{GB}$ , as shown in Fig. 5.13(b). However, the amount of discontinuous  $\alpha_{GB}$  is increased from 5% at the true strain of 0.025 to 17% to the true strain of 0.04 (as shown in Fig. 5.14), indicating that more  $\alpha_{GB}$  becomes discontinuous or fragmented. As a result, the fragmentation of the continuous  $\alpha_{GB}$  weakens the strengthening effect of the  $\alpha_{GB}$  to the  $\beta$  grain boundaries. The GGCROD micrograph shown in Fig. 5.13(c) demonstrates that almost all the  $\beta$  grain boundary regions are deformed. The orientations of the  $\beta$  regions near the grain boundaries are largely deviated ( $3.5^\circ$ - $6^\circ$ ) from those of their gravity center. In many regions near the grain boundaries and triple junctions, the deviation reaches  $8^\circ$ . From the cases in  $700^\circ\text{C}$  deformation specimen, such orientation deviation may be from the formation of dislocations. Further TEM verification is needed. Clearly, the fragmentation of the  $\alpha_{GB}$  leads to the softening of the alloy. Therefore the flow stress behavior in Stage II is a result of softening related to the fragmentation of the  $\alpha_{GB}$  and the formation of dislocations.



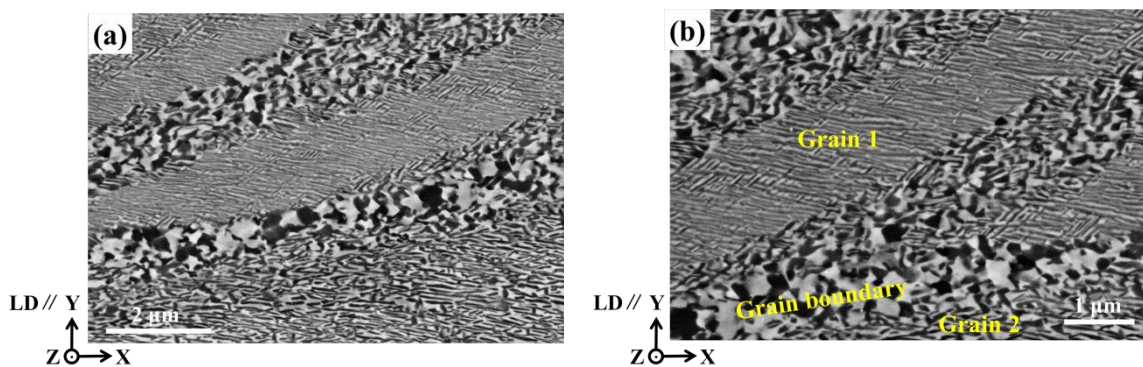
**Fig. 5.14** Length percentages of  $\beta$  grain boundaries with continuous  $\alpha_{GB}$ , with discontinuous  $\alpha_{GB}$  and without  $\alpha_{GB}$  in the specimens deformed to the respective true strain of 0.025 and 0.04.



Fig. 5.15 presents one example of deformed microstructures of the specimen compressed to the true strain of 0.10 corresponding to the process in Stage III in the stress-strain curve. Global microstructure examination was conducted in a large sample area ( $2 \times 2 \text{ mm}^2$ ). It revealed that after the deformation to the true strain of 0.10, all the  $\beta$  grains are covered with  $\alpha$  phase, especially the  $\beta$  grain interiors, as shown in Fig. 5.15. The  $\beta$  to  $\alpha$  phase transformation happened intensively. It is known that  $\alpha$  phase is harder than  $\beta$  phase. Thus, the massive  $\beta$  to  $\alpha$  phase transformation strengthens the  $\beta$  grains. Hence, clearly, the hardening in Stage III is related to the massive  $\beta$  to  $\alpha$  phase transformation in the whole material.



**Fig. 5.15** BSE micrograph of Ti-7333 alloy after the isothermal compression at 600 °C to a true strain of 0.1.



**Fig. 5.16** BSE micrographs of the Ti-7333 alloy after the isothermal compression at 600 °C to a true strain of 0.35.

When the deformation progressed to the true strain of 0.35, corresponding to Stage IV in the stress-strain curve in Fig. 5.11, a large amount of deformation bands appears in the  $\beta$  grain

interiors, as shown in Fig. 5.16(a), and along the initial  $\beta$  grain boundaries, as shown in Fig. 5.16(b). It is seen that the deformation bands are composed of fragmented and also spheroidized  $\alpha$  phase. Many investigations reported in the literature [137-145] have evidenced that the spheroidization of  $\alpha$  phase in Ti alloys can lead to work softening behavior of the alloy during the deformation. Clearly, the formation of deformation bands was due to the spheroidization of  $\alpha$  phase and then contributed to the softening of the alloy in Stage IV.

## 5.6 Summary

In this Chapter, the deformation processes of a metastable  $\beta$  titanium alloy with a  $\beta$  quenched initial microstructure under a uniaxial isothermal compression at respective 700 °C and 600 °C were thoroughly investigated by correlating the stress-strain behavior with the microstructure evolution in multiscale.

For the 700 °C compression, the deformation behavior can be categorized into three typical stages, e.g., a linear state (Stage I), a discontinuous yielding (Stage II) and a steady-state (Stage III). For Stage I, the  $\beta$  to  $\alpha$  phase transformation happened intensively along the  $\beta$  grain boundaries before and during the deformation. More than 90% of the boundaries are occupied by  $\alpha_{GB}$ . The linear behavior of the alloy started to deviate from the Young's modulus at the late stage, indicating the onset of plastic deformation. The behavior results from the dislocation slip in the  $\beta$  grain boundary regions. For the discontinuous yielding, the drastic drop of the stress is originated from the fragmentation of the  $\alpha_{GB}$  and the further formation of dislocations in a collective avalanche-like way in the  $\beta$  grain boundary regions. For the steady-state stage, the deformation behavior of the  $\beta$  grains is further diversified into two types, i.e., type I having their  $\{110\}_{\beta} \langle \bar{1}\bar{1}1 \rangle_{\beta}$  slip system in the favorable orientation with respect to the external compressive load and type II with their  $\{1\bar{1}\bar{2}\}_{\beta} \langle \bar{1}1\bar{1} \rangle_{\beta}$  system in the favorable orientation. Thus for the type I  $\beta$  grains the deformation progresses through the formation of  $\{110\}_{\beta} \langle \bar{1}\bar{1}1 \rangle_{\beta}$  dislocations counter-balanced by the arrangement of the formed dislocations into slip bands, whereas for the type II  $\beta$  grains the deformation is realized by the intensive formation of intragranular  $\alpha$  precipitates that is characterized by a large shear strain in  $\{1\bar{1}\bar{2}\}_{\beta} \langle \bar{1}1\bar{1} \rangle_{\beta}$  system accompanied by some small lattice distortions. This evidenced that the phase transformation serves as another kind of deformation

mechanism for crystal plasticity.

For the 600 °C compression, the deformation behavior can be categorized into four typical stages, e.g., a linear state (Stage I), a discontinuous yielding (Stage II), an hardening state (Stage III) and a softening state (Stage IV). For Stage I and II, the characteristics of microstructure are similar to that of the 700 °C compression. The  $\alpha_{GB}$  formed in Stage I, and the fragmentation of the  $\alpha_{GB}$  lead to the discontinuous yielding. For Stage III and IV, the massive  $\beta$  to  $\alpha$  phase transformation contribute to the work hardening in Stage III, whereas the formation of deformation bands with the spheroidized  $\alpha$  phase is related to the work softening in Stage IV.

The present work provides new information of orientation dependent deformation mechanisms of metastable  $\beta$  titanium alloys, especially on the contribution of the phase transformation to the overall deformation behavior and offers detailed experimental data that can be useful for the simulation of the mechanical behavior of metastable  $\beta$  titanium alloys.



## Chapter 6 Conclusions and Perspectives

### 6.1 Conclusions

In the present work, a thorough experimental and theoretically crystallographic study on phase transformation behavior and hot deformation behavior has been conducted on Ti-7333 alloy. From the experimental and calculation results of the present work, following main conclusions can be drawn:

#### *Crystallographic features of $\beta$ to $\alpha$ phase transformation and associated Lattice deformation*

The intragranular  $\alpha$  precipitates formed during the stress-free condition at either 700 °C or 600 °C possess a plate shaped morphology with the  $\{11\ 11\ 13\}_{\beta}$  as the broad faces or the habit plane. Such  $\alpha$  plates are denoted major  $\alpha$  plates. They obey the Burgers Orientation Relationship (BOR) with the  $\beta$  matrix. The transformation progresses in a mixed displacive and diffusive manner. The structure transformation is realized by a contraction in the  $\langle 1\bar{1}\bar{2} \rangle_{\beta}$ , an elongation in the  $\langle \bar{1}1\bar{1} \rangle_{\beta}$  and  $\langle 110 \rangle_{\beta}$ , and a shear on the  $\{1\bar{1}\bar{2}\}_{\beta} \langle \bar{1}1\bar{1} \rangle_{\beta}$  slip system. Globally twelve  $\alpha$  variants are formed within each  $\beta$  grain and locally three variants interrelated by a  $60^\circ / \langle 11\bar{2}0 \rangle_{\alpha}$  rotation form a triangular cluster.

#### *Formation mechanisms of two kinds of nano-sized $\alpha$ domains during heat treatment*

The elastic strain generated by the  $\beta$  to  $\alpha$  transformation induces the formation of two kinds of nano-sized  $\alpha$  domains in each major  $\alpha$  plate. This demonstrates that the  $\alpha$  plates are rather polycrystalline than monocrystalline as has traditionally been considered. One kind of domains forms at the interfaces between the major  $\alpha$  plate and the  $\beta$  matrix (interface  $\alpha$ ). Such domains respect the BOR with the  $\beta$  matrix and related to the major  $\alpha$  by a  $60^\circ / \langle 11\bar{2}0 \rangle_{\alpha}$  rotation. The formation of such  $\alpha$  domains can effectively accommodate the shear strain and one component of the normal strain present at the interface between the major  $\alpha$  plate and the  $\beta$  matrix. The geometrical characteristics of the lattice strain of such  $\alpha$  domains allow a

maximum profit from the low CRSS slip systems of the major  $\alpha$  plate and the  $\beta$  to minimize the overall strain. These domains further serve as sympathetic nuclei for the formation of the other major  $\alpha$  plate with the same orientation and contribute to the formation of the triangular structured major  $\alpha$  plate clusters.

The other  $\alpha$  domains (penetrating  $\alpha$ ) are in lamellar shape and organized into parallel bands going through the major  $\alpha$  plate. The broad faces of the bands are roughly normal to one of the large normal strains generated by the major  $\alpha$  plate. These  $\alpha$  domains are related with the major  $\alpha$  by a  $60^\circ/\langle 11\bar{2}0 \rangle_\alpha$  rotation but it does not obey the BOR with the  $\beta$  matrix. The formation of the bands of the penetrating  $\alpha$  domains is to accommodate the larger extension strain from the major  $\alpha$  plate. As these domains also generate large incompatible strains either with the major  $\alpha$  plate or with the  $\beta$  matrix, their growth are largely confined, thus each band is formed by the aligned and equally spaced identical penetrating  $\alpha$  domains. The results of the present work provide new information on the impact of the displacive characters of the  $\beta$  to  $\alpha$  phase transformation on the sub-structure and the microstructure features of the product  $\alpha$  phase. Such information can be incorporated to simulation models for  $\beta$  to  $\alpha$  transformation of Ti alloys.

### ***Variant selection mechanisms of intragranular $\alpha$ precipitates under isothermal deformation***

For the phase transformation and variant selection of intragranular  $\alpha$  under deformation at 700 °C, the interplay between the lattice strain induced by phase transformation and the imposed compressive strain and the applied compressive load was evidenced as the key factor for  $\alpha$  variant selection, and result in a strong  $\alpha$  variant selection for the intragranular precipitates during the isothermal compression. The selected variants can be classified into two groups (group I and group II), according to their precipitation amount.

For the group I  $\alpha$  precipitates, the precipitation amount is large and the precipitates are agglomerated in the  $\beta$  grains with fewer dislocations. Only 2 variants forming ‘cross-shaped’ clusters are selected. The 2 variants respect the BOR and are interrelated by a  $90^\circ$  rotation around the  $\langle 1\ 1.38\ \bar{2}.38\ 0 \rangle_\alpha$  axis. Such variants consume the maximum amount of deformation work by the external compression. This energy criterion can be further

interpreted by the compatibility of the microscopic strain to the macroscopic strain and the shear stress resolved from the external load to the local transformation shear deformation. That is the formation of the selected variants offer the maximum contribution to the imposed compression strain and receive the maximum resolved shear stress on the  $\{1\bar{1}2\}_{\beta}<\bar{1}1\bar{1}>_{\beta}$  shear system for the structure transformation. For the group II  $\alpha$  precipitates, they appear in much smaller numbers and are dispersed in the  $\beta$  grains that are occupied also by large amount of slip bands. The numbers of the variants in group II are not constant, varying from 2 to 4 from one  $\beta$  grain to another. The selection of the variants still respects the energy criterion for the selection of the group I precipitates and reproduce the same strain and stress compatible characters as the group I precipitates but with restriction from the local stress and strain states imposed by the large amount of dislocations.

For the phase transformation and variant selection of the intragranular  $\alpha$  under compression at 600 °C. The interplay between the lattice strain induced by phase transformation and the macroscopic deformation was evidenced as the key factor for  $\alpha$  variant selection. Under such a criterion, 4 BOR variants are formed during the compression. The formation of the selected variants provided compatible strains to the macroscopic deformation.

### ***Correlation between $\beta$ to $\alpha$ phase transformation and hot deformation behavior***

For the 700 °C compression, the deformation behavior of the alloy can be categorized into three typical stages, e.g., a linear state (Stage I), a discontinuous yielding (Stage II) and a steady-state (Stage III). For Stage I, the  $\beta$  to  $\alpha$  phase transformation happened intensively along the  $\beta$  grain boundaries before and during the deformation. More than 90% of the boundaries are occupied by  $\alpha_{GB}$ . The linear behavior of the alloy started to deviate from the Young's modulus at the late stage, indicating the onset of plastic deformation. This behavior results from the dislocation slip in the  $\beta$  grain boundary regions. For the discontinuous yielding, the drastic drop of the stress is originated from the fragmentation of the  $\alpha_{GB}$  and the further formation of dislocations in a collective avalanche-like way in the  $\beta$  grain boundary regions. For the steady-state stage, the deformation behavior of the  $\beta$  grains is further

diversified into two types, i.e., type I having their  $\{110\}_{\beta} \langle \bar{1}\bar{1}1 \rangle_{\beta}$  slip system in the favorable orientation with respect to the external compressive load and type II with their  $\{1\bar{1}\bar{2}\}_{\beta} \langle \bar{1}1\bar{1} \rangle_{\beta}$  system in the favorable orientation. Thus for the type I  $\beta$  grains the deformation progresses through the formation of  $\{110\}_{\beta} \langle \bar{1}\bar{1}1 \rangle_{\beta}$  dislocations counter-balanced by the arrangement of the formed dislocations into slip bands, whereas for the type II  $\beta$  grains the deformation is realized by the intensive formation of intragranular  $\alpha$  precipitates that is characterized by a large shear strain in the  $\{1\bar{1}\bar{2}\}_{\beta} \langle \bar{1}1\bar{1} \rangle_{\beta}$  system accompanied by some small lattice distortions. This evidences that the phase transformation serves as another kind of deformation mechanism for crystal plasticity.

For the 600 °C compression, the deformation behavior can be categorized into four typical stages, e.g., a linear state (Stage I), a discontinuous yielding (Stage II), an hardening state (Stage III) and a softening state (Stage IV). For Stage I and II, the characteristics of the microstructure are similar to that of the 700 °C compression. The  $\alpha_{GB}$  formed in Stage I, and the fragmentation of the  $\alpha_{GB}$  lead to the discontinuous yielding. For Stage III and IV, the massive  $\beta$  to  $\alpha$  phase transformation contribute to the work hardening in Stage III, whereas the formation of deformation bands with the spheroidized  $\alpha$  phase is related to the work softening in Stage IV.

## 6.2 Perspectives

In this PhD work, a thoroughly study was conducted on the  $\beta$  to  $\alpha$  phase transformation behavior and variant selection of  $\alpha$  phase during thermomechanical processing in Ti-7333 alloy. Meanwhile, the correlation between  $\beta$  to  $\alpha$  phase transformation and the hot deformation behavior was characterized. Comprehensive information concerning these fundamental issues was obtained for the metastable  $\beta$  titanium alloy, opening new perspectives on further investigations of this alloy system and can be summarized as follows:

- (1) For the  $\beta$  to  $\alpha$  phase transformation, the present work mainly focused on the formation of intragranular  $\alpha$  precipitates and its variant selection. However, in addition to the intragranular  $\alpha$  precipitates, the formation of the grain boundary  $\alpha$  ( $\alpha_{GB}$ ), and the Widmanstätten  $\alpha$  ( $\alpha_w$ ), under the thermomechanical processing also need to be explored, and their variant selection during the transformation needs to be worked out. This will



allow revealing the complete underlying mechanisms of phase transformation in the metastable  $\beta$  titanium alloys during thermomechanical processing.

- (2) It is known that the  $\alpha_{GB}$  has been formed during the linear deformation stage during the hot deformation. Thus, the effect of the  $\alpha_{GB}$  on slip transfer during the deformation behavior needs to be further investigated and the formation of large amount of  $\beta$  grain boundary dislocations to be revealed. Meanwhile, the spheroidization of  $\alpha$  precipitates happened during the hot deformation. The in-depth mechanisms of the spheroidization still need to be examined.
- (3) The  $\beta$  to  $\alpha$  phase transformation during the isothermal deformation processes has been evidenced. The formation of  $\alpha$  precipitates is found to be selective in different  $\beta$  grains. Hence, the transformation kinetics should be revealed. Moreover, the difference on the transformation kinetics between the transformation during deformation and that during heat treatment needs to be studied for the theoretical purpose and for technical purpose.



## Appendix A

### Specification of 12 BOR variants

**Table A.1** Notification of the 12 BOR variants

No.	Variant	No.	Variant
V1	$(110)_\beta // (0001)_\alpha$	V7	$(011)_\beta // (0001)_\alpha$
	$[\bar{1}\bar{1}\bar{1}]_\beta // [11\bar{2}0]_\alpha$		$[1\bar{1}\bar{1}]_\beta // [11\bar{2}0]_\alpha$
V2	$(110)_\beta // (0001)_\alpha$	V8	$(101)_\beta // (0001)_\alpha$
	$[\bar{1}\bar{1}1]_\beta // [11\bar{2}0]_\alpha$		$[11\bar{1}]_\beta // [11\bar{2}0]_\alpha$
V3	$(\bar{1}10)_\beta // (0001)_\alpha$	V9	$(011)_\beta // (0001)_\alpha$
	$[111]_\beta // [11\bar{2}0]_\alpha$		$[11\bar{1}]_\beta // [11\bar{2}0]_\alpha$
V4	$(\bar{1}10)_\beta // (0001)_\alpha$	V10	$(101)_\beta // (0001)_\alpha$
	$[11\bar{1}]_\beta // [11\bar{2}0]_\alpha$		$[\bar{1}\bar{1}1]_\beta // [11\bar{2}0]_\alpha$
V5	$(0\bar{1}1)_\beta // (0001)_\alpha$	V11	$(\bar{1}01)_\beta // (0001)_\alpha$
	$[111]_\beta // [11\bar{2}0]_\alpha$		$[111]_\beta // [11\bar{2}0]_\alpha$
V6	$(\bar{1}01)_\beta // (0001)_\alpha$	V12	$(01\bar{1})_\beta // (0001)_\alpha$
	$[1\bar{1}\bar{1}]_\beta // [11\bar{2}0]_\alpha$		$[\bar{1}\bar{1}1]_\beta // [11\bar{2}0]_\alpha$



## Appendix B

### Experimental setup of the *in-situ* neutron diffraction measurement to detect the intragranular $\alpha$ precipitation

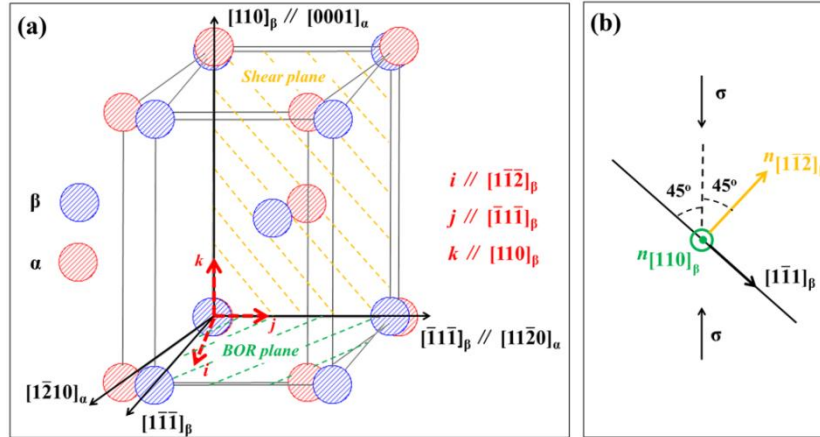


**Fig. A1** (a) Atomic correspondences between the  $\beta$  and the  $\alpha$  phase under the Burgers orientation relationship (BOR), where the transformation shear plane is shaded with the yellow lines and the BOR plane with the green lines; (b) geometrical relation between the BOR plane normal (in green) and the shear plane normal (in yellow) for the selected intragranular  $\alpha$  variant under the compressive load  $\sigma$ . The shear system for its formation is in the ideal orientation to receive highest resolved shear stress from the external load.

The results in Chapter 4 concerning the variant selection of the intragranular  $\alpha$  precipitates during the hot compression at 700 °C indicated that the  $\beta$  to  $\alpha$  phase transformation followed the BOR. Only the intragranular  $\alpha$  variants having the initial  $\{1\bar{1}\bar{2}\}_{\beta} <\bar{1}1\bar{1}>_{\beta}$  shear system of the parent  $\beta$  grain at the favorable orientation with respect to the external load were selected. With the atomic correspondences between the two phases, as shown in Fig. A1(a), the geometrical relation between the shear system for phase transformation ( $\{1\bar{1}\bar{2}\}_{\beta} <\bar{1}1\bar{1}>_{\beta}$  shaded with the yellow lines in the figure) and the BOR system (shaded with the green lines in the figure) can be figured out. The shear plane is perpendicular to the BOR plane, and the two planes share one  $<\bar{1}1\bar{1}>_{\beta}$  direction that serves, on the one hand, as the shear direction and, on the other hand, as the BOR direction. As the  $\alpha$

variant corresponding to the  $\{1\bar{1}2\}_\beta < \bar{1}1\bar{1} \rangle_\beta$  shear system that receives the maximum resolved shear stress from the external load can be selected, the orientation of its BOR plane with respect to the external load can be deduced, as shown in Fig. A1(b). In the ideal case, the load direction lies on the BOR plane. Since the interplanar spacing of  $\{110\}_\beta$  and  $\{0002\}_\alpha$  are  $d_{110}=4.625 \text{ \AA}$  ( $2\theta=43.34^\circ$  when  $\lambda=1.7076 \text{ \AA}$ ) and  $d_{0002}=4.679 \text{ \AA}$  ( $2\theta=42.57^\circ$ ), respectively, the two reflections can be detected simultaneously with the 2D detector (with a window of  $15^\circ$ ) set at  $2\theta=42^\circ$ .

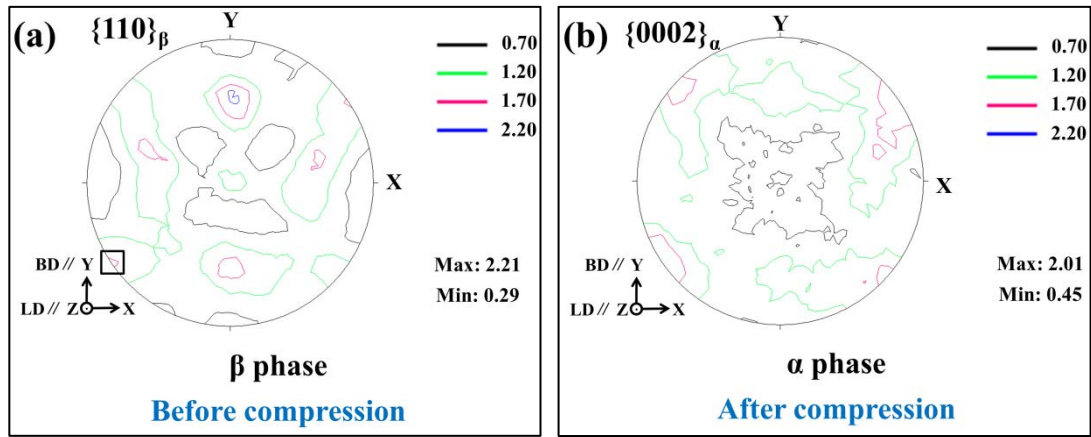


**Fig. A2 (a)**  $\{110\}_\beta$  pole figure measured by neutron diffraction at room temperature before the hot compression; **(b)**  $\{0002\}_\alpha$  pole figure measured after the hot compression. The black frame in **(a)** indicates the  $\{110\}_\beta$  peak used to detect the formation of the intragranular  $\alpha$  precipitates during *in-situ* neutron diffraction measurement.

Under such a geometrical configuration, the  $\{110\}_\beta$  pole figure of the initial  $\beta$  microstructure at the room temperature was measured, as shown in Fig. A2(a). The load is parallel to the Z axis that is located at the center of the pole figure. According to the above deduction, the  $\{110\}_\beta$  planes located at the outer circle of the pole figure could be the BOR planes for the selected intragranular  $\alpha$  precipitates. Thus we set the geometrical configuration of the loading axis, the incident beam and the 2D detector of the *in-situ* neutron diffraction experiment to allow detecting the highest  $\{110\}_\beta$  peak, as highlighted with the black frame in the pole figure in Fig. A2(a). After the specimen was deformed to the true strain of 0.35, we measure the  $\{0002\}_\alpha$  pole figure of the same specimen under the same specimen orientation with respect to the incident beam and the detector. The  $\{0002\}_\alpha$  pole figure is shown in Fig.

A2(b). It is seen that the highest  $\{0002\}_\alpha$  pole density well correlates to the highest  $\{110\}_\beta$  pole density in Fig. A2(a). This result verified the neutron diffraction setup to detect the formation of the intragranular  $\alpha$  precipitates.





## References

- [1]. J.J. Jonas, S.J. Mu, T.A. Samman, G. Gottstein, L. Jiang, E. Martin. The role strain accommodation during the variant selection of primary twins in magnesium. *Acta Materialia*. 2011, 59: 2046-2056
- [2]. S.J. Mu, J.J. Jonas, G. Gottstein. Variant selection of primary, secondary and tertiary twins in a deformed Mg alloy. *Acta Materialia*. 2012, 60: 2043-2053
- [3]. A. Devaraj, V.V. Joshi, A. Srivastava, S. Manandhar, V. Moxson, V.A. Duz, C. Lavender. A low-cost hierarchical nanostructured beta-titanium alloy with high strength. *Nature Communication*. 2016, 7: 11176
- [4]. G. L. ering, J.C. Williams. *Titanium*, Berlin, 2007, Heidelberg: Springer Berlin Heidelberg
- [5]. R.R. Boyer. Attributes, characteristics, and applications of titanium and its alloys. *JOM*. 2010, 62: 21-24
- [6]. R. Shi. Variant selection during alpha precipitation in titanium alloys: A simulation study. The Ohio State University, 2014.
- [7]. Y.F. Zheng , R.E.A. Williams, D. Wang , R. Shi, S. Nag, P. Kami, J.M. Sosa, R. Banerjee, Y. Wang, H.L. Fraser. Role of  $\omega$  phase in the formation of extremely refined intragranular  $\alpha$  precipitates in metastable  $\beta$ -titanium alloys. *Acta Materialia*. 2016, 103: 850-858
- [8]. E.W. Collings. *Materials Properties Handbook. Titanium alloys*, ASM International, Materials Park. 1994, 1–35
- [9]. G. Lutjering, J.C. Williams. *Titanium*. Springer-Verlag. 2003, 1–15.
- [10]. P.D. Frost, W.M. Parris, L.L. Hirsch, J.R. Doig, C.M. Schwartz. Isothermal transformation of titanium-chromium alloys. *Trans. ASM*. 1954, 46: 231–256
- [11]. B.S. Hickman. The Formation of Omega Phase in Titanium and Zirconium Alloys: A Review. *Journal of Materials Science*. 1969, 4: 554-563

- 
- [12]. F. Prima, P. Vermaut, G. Texier, D. Ansel, T. Gloriant. Evidence of  $\alpha$ -nanophase heterogeneous nucleation from  $\omega$  particles in a  $\beta$ -metastable Ti-based alloy by high-resolution electron microscopy. *Scripta Materialia*. 2006, 54: 645–648
- [13]. Y. Ohmori, T. Ogo, K. Nakai, S. Kobayashi. Effects of  $\omega$ -phase precipitation on  $\beta \rightarrow \alpha''$  transformations in a metastable  $\beta$  titanium alloy. *Materials Science and Engineering: A*. 2001, 312: 182–188.
- [14]. P.G. Allen, P.J. Bania, A.J. Hutt, Y. Combres. Beta titanium alloy. *Titanium 95*, Science and Technology. London: The Institute of Materials. 1996: 1680–1687.
- [15]. S.L Nyakana, J.C. Fanning, R.R. Boyer. Quick reference guide for  $\beta$  titanium alloys in the 00s. *Journal of Materials Engineering and Performance*. 2005, 14(6): 799–811.
- [16]. B. Jiang. Effect of Severe Plastic Deformation on Microstructure in Metastable  $\beta$ -Ti Alloys. University of Tsukuba, 2015.
- [17]. An Update on Properties and Applications for Ti-5Al-5Mo-5V-3Cr. Presented at the International Titanium Association. Scottsdale 2005, presented by VSMPO staff
- [18]. G. Tomchik. Overview of Titanium Applications on Advanced Commercial Transports. AeroMat Conference, unpublished research, 15 May 2006.
- [19]. R. Panza-Giosa. The Effect of Heat Treatment on the Microstructure Evolution and Mechanical Properties of Ti-5Al-5V-5Mo-3Cr, and Its Potential Application in Landing Gears. McMaster University, 2009.
- [20]. S. Veeck, D. Lee, R. Boyer, R. Briggs. The castability of Ti-5553 alloy: Its microstructure and properties. *Journal of Advanced Materials*. 2005, 37: 40–45.
- [21]. B. Appolaire, L. Hélicher, E. Aeby-Gautier. Modelling of phase transformation kinetics in Ti alloys-Isothermal treatments. *Acta Materialia*. 2005, 53: 3001–3011.
- [22]. Z. Sun, S. Guo, H. Yang. Nucleation and growth mechanism of  $\alpha$ -lamellae of Ti alloy TA15 cooling from an  $\alpha + \beta$  phase field. *Acta Materialia*. 2013, 61: 2057–2064
- [23]. D.I. Potter. The structure, morphology and orientation relationship of V3N in  $\alpha$ -vanadium. *Journal of the Less Common Metals*. 1973, 31: 299–309
- [24]. J.K. Fan, J.S. Li, H.C. Kou, K. Hua, B. Tang, Y.D. Zhang. Influence of solution treatment on microstructure and mechanical properties of a near  $\beta$  titanium alloy Ti-7333. *Materials & Design*. 2015, 83: 499–507

- [25]. J.K. Fan, J.S. Li, H.C. Kou, K. Hua, B. Tang. The Interrelationship of Fracture Toughness and Microstructure in a New Near  $\beta$  Titanium Alloy Ti-7Mo-3Nb-3Cr-3Al. *Materials Characterization*. 2014, 96: 93–99
- [26]. J.K. Fan, J.S. Li, H.C. Kou, K. Hua, B. Tang, Y.D. Zhang. Microstructure and mechanical property correlation and property optimization of a near  $\beta$  titanium alloy Ti-7333. *Journal of Alloys and Compounds*. 2016, 682: 517–524
- [27]. W.G. Burgers. On the process of transition of the cubic-body-centered modification into the hexagonal-close-packed modification of zirconium. *Physica*. 1934, 1: 561-586.
- [28]. J.W. Cahn, G.M. Kalonji, Symmetry in solid-solid transformation morphologies. In: Pittsburgh PA, Aaronson HI, et al., editors. *Proceedings of an international conference on solid-solid phase transformations*. New York: AIME Press, 1982, p. 3
- [29]. S.M.C. van Bohemen, J. Sietsma, S. van der Zwaag. Experimental observations elucidating the mechanisms of structural bcc-hcp transformations in  $\beta$ -Ti alloys. *Physics Review. B*. 2006, 74: 134114
- [30]. T. Furuhashi, H. Nakamori, T. Maki. Crystallography of a Phase Precipitated on Dislocations and Deformation Twin Boundaries in a  $\beta$  Titanium Alloy. *Material Transactions, JIM*. 1992, 33: 585–595
- [31]. T. Furuhashi, S. Takagi, H. Watanabe, T. Maki. Crystallography of grain boundary  $\alpha$  precipitates in a  $\beta$  titanium alloy. *Metallurgical and Materials Transactions A*. 1996, 27: 1635-1646
- [32]. D. Banerjee, J.C. Williams. Perspectives on titanium science and technology. *Acta Materialia*. 2013, 61: 844
- [33]. S. Nag, R. Banerjee, R. Srinivasan, J. Y. Hwang, M. Harper, H. L. Fraser.  $\omega$ -Assisted nucleation and growth of  $\alpha$  precipitates in the Ti-5Al-5Mo-5V-3Cr-0.5Fe  $\beta$  titanium alloy. *Acta Materialia*. 2009, 57: 2136–2147
- [34]. R. Shi, Y. Wang. Variant selection during  $\alpha$  precipitation in Ti-6Al-4V under the influence of local stress – A simulation study. *Acta Materialia*. 2013, 61: 6006-6024
- [35]. R. Shi, V. Dixit, H.L. Fraser, Y. Wang. Variant selection of grain boundary  $\alpha$  by special prior  $\beta$  grain boundaries in titanium alloys. *Acta Materialia*. 2014, 75: 156-166

- 
- [36]. R. Shi, N. Ma, Y. Wang. Predicting equilibrium shape of precipitates as function of coherency state. *Acta Materialia*. 2012, 60: 4172-4184
- [37]. M. Naoki, N. Takahiro, I. Teruhiko, A. Kei. Reasons for Formation of Triangular  $\alpha$  Precipitates in Ti-15V-3Cr-3Sn-3Al Titanium Alloy. *Materials Transactions*. 2006, 47: 341-347
- [38]. C.M. Liu, X.J. Tian, H.B. Tang, H.M. Wang. Microstructural characterization of laser melting deposited Ti-5Al-5Mo-5V-1Cr-1Fe near  $\beta$  titanium alloy. *Journal of Alloys and Compounds*. 2013, 572: 17-24
- [39]. N. Jones, R. Dashwood, D. Dye, M. Jackson. Thermomechanical processing of Ti-5Al-5Mo-5V-3Cr. *Materials Science and Engineering: A*. 2008, 490: 369-377
- [40]. V. Shevel'kov. Structural conversions in VT22 titanium alloy during aging. *Materials Science and Engineering: A*. 1992, 34: 534-539
- [41]. M. Salib, J. Teixeira, L. Germain, E. Lamielle, N. Gey, E. Aeby-Gautier. Influence of transformation temperature on microtexture formation associated with  $\alpha$  precipitation at  $\beta$  grain boundaries in a  $\beta$  metastable titanium alloy. *Acta Materialia*. 2013, 61: 3758-3768
- [42]. G. Gottstein, L. Shvindlerman. *Grain Boundary Migration in Metals: thermodynamics, kinetics, applications*, second ed., Boca Raton, 2009, Taylor & Francis Group
- [43]. T. Furuhashi, S. Takagi, H. Watanabe, T. Maki. Crystallography of grain boundary  $\alpha$  precipitates in a  $\beta$  titanium alloy. *Metallurgical and Materials Transactions A*. 1996, 27: 1635-1646
- [44]. M. Salib, J. Teixeira, L. Germain, E. Lamielle, N. Gey, E. Aeby-Gautier. Influence of transformation temperature on microtexture formation associated with  $\alpha$  precipitation at  $\beta$  grain boundaries in a  $\beta$  metastable titanium alloy. *Acta Materialia*. 2013, 61: 3758-3768
- [45]. C. Cayron. Importance of the transformation in the variant selection mechanisms of thermomechanically processed titanium alloys. *Scripta Materialia*. 2008, 59: 570-573
- [46]. D. Bhattacharyya, G.B. Viswanathan, H.L. Fraser. Crystallographic and morphological relationships between  $\beta$  phase and the Widmanstätten and allotriomorphic  $\alpha$  phase at special  $\beta$  grain boundaries in an  $\alpha/\beta$  titanium alloy. *Acta Materialia*. 2007, 55: 6765-6778

- [47]. E. Lee, R. Banerjee, S. Kar, D. Bhattacharyya, H.L. Fraser. Selection of  $\alpha$  variants during microstructural evolution in  $\alpha/\beta$  titanium alloy. *Philosophical Magazine*. 2007, 87: 3615-3627
- [48]. R. Shi, V. Dixit, H.L. Fraser, Y. Wang. Variant selection of grain boundary  $\alpha$  by special prior  $\beta$  grain boundaries in titanium alloys. *Acta Materialia*. 2014, 75: 156-166
- [49]. R. Shi, V. Dixit, G.B. Viswanathan, H.L. Fraser, Y. Wang. Experimental assessment of variant selection rules for grain boundary  $\alpha$  in titanium alloys. *Acta Materialia*. 2016, 102: 197-211
- [50]. N. Vanderesse, E. Maire, M. Darrieulat, F. Montheillet, M. Moreaudc, D. Jeulin. Three-dimensional microtomographic study of Widmanstätten microstructures in an alpha/beta titanium alloy. *Scripta Materialia*. 2008, 58: 512-515
- [51]. D. Qiu, R. Shi, D. Zhang, W. Lua, Y. Wang. Variant selection by dislocations during a precipitation in  $\alpha/\beta$  titanium alloys. *Acta Materialia*. 2015, 88: 218-231
- [52]. C.P. Luo, G.C. Weatherly. The invariant line and precipitation in a Ni-45 wt% Cr alloy. *Acta Metallurgica*. 1987, 35: 1963-1972
- [53]. T. Furuhashi, T. Maki. Variant selection in heterogeneous nucleation on defects in diffusional phase transformation and precipitation, *Materials Science and Engineering: A*. 2001, 312: 145-154
- [54]. S.C. Wang, M. Aindow, M.J. Starink. Effect of self-accommodation on  $\alpha/\alpha$  boundary populations in pure titanium. *Acta Materialia*. 2013, 51: 2485-2503
- [55]. K. Otsuka, X. Ren. Physical metallurgy of Ti-Ni-based shape memory alloys. *Progress in Materials Science*. 2005, 50: 511-678
- [56]. D. He, J.C. Zhu, S. Zaefferer, D. Raabe, Y. Liu, Z.L. Lai, X.W. Yang. Influences of deformation strain, strain rate and cooling rate on the Burgers orientation relationship and variants morphology during phase transformation in a near titanium alloy. *Materials Science and Engineering: A*. 2012, 549: 20-29
- [57]. T. Karthikeyan, A. Dasgupta, R. Khatirkar, S. Saroja, I. Samajdar, M. Vijayalakshmi. Effect of cooling rate on transformation texture and variant selection during  $\beta \rightarrow \alpha$  transformation in Ti-5Ta-1.8Nb alloy. *Materials Science and Engineering: A*. 2010, 528: 549-558

- 
- [58]. G.A. Sargent, K.T. Kinsel, A.L. Pilchak, A.A. Salem, S.L. Semiatin. Variant selection during cooling after beta annealing of Ti-6Al-4V ingot material. *Metallurgical and Materials Transactions A*. 2012, 43: 3570-3585
- [59]. G.C. Obasi, S. Biroasca, D.G. Leo Prakash, J. Quinta da Fonseca, M. Preuss. The influence of rolling temperature on texture evolution and variant selection during phase transformation in Ti-6Al-4V. *Acta Materialia*. 2012, 60: 6013-6024
- [60]. Z.S. Zhu, J.L. Gu, N.P. Chen. Variant selection in phase transformation of cold rolled titanium sheet. *Scripta Materialia*. 1996, 34: 1281-1286
- [61]. Y. Xu, J. Zhang, Y. Bai, M.A. Meyers. Shear localization in dynamic deformation: microstructural evolution. *Metallurgical and Materials Transactions A*. 2008, 39: 811–843
- [62]. T.R. Bieler, S.L. Semiatin. The origins of heterogeneous deformation during primary hot working of Ti-6Al-4V. *International Journal of Plasticity*. 2002, 18(9): 1165–1189
- [63]. H. Tobe, H.Y. Kim, T. Inamura, H. Hosoda, S. Miyazaki. Origin of {332} twinning in metastable  $\beta$ -Ti alloys. *Acta Materialia*. 2014, 64: 345–355
- [64]. P. Eyckens, H. Mulder, J. Gawad, H. Vegter, D. Roose, T. Boogaard, A.V. Bael, P.V. Houtte. The prediction of differential hardening behaviour of steels by multi-scale crystal plasticity modelling. *International Journal of Plasticity*. 2015, 73: 119-141
- [65]. N. Fujita, N. Ishikawa, F. Roters, C.C. Tasan, D. Raabe. Experimental–numerical study on strain and stress partitioning in bainitic steels with martensite–austenite constituents. *International Journal of Plasticity*. 2018, 104: 39-53
- [66]. A.S. Khan, J. Liu. A deformation mechanism based crystal plasticity model of ultrafine-grained/nanocrystalline FCC polycrystals. *International Journal of Plasticity*. 2016, 86: 56-69
- [67]. L.A.I. Kestens, H. Pirgazi. Texture formation in metal alloys with cubic crystal structures. *Materials Science Technology*. 2016, 32: 1303-1315
- [68]. M.S. Pham, M. Iadicola, A. Creuziger, L. Hu, A.D. Rollett. Thermally-activated constitutive model including dislocation interactions, aging and recovery for strain path dependence of solid solution strengthened alloys: Application to AA5754-O. *International Journal of Plasticity*. 2015, 75: 226-243

- [69]. C.C. Tasan, J.P. Hoefnagels, M. Diehl, D. Yan, F. Roters, D. Raabe. Strain localization and damage in dual phase steels investigated by coupled in-situ deformation experiments and crystal plasticity simulations. *International Journal of Plasticity*. 2014, 63: 198-210
- [70]. A.S. Khan, Y.S. Suh, R. Kazmi. Quasi-static and dynamic loading responses and constitutive modeling of titanium alloys. *International Journal of Plasticity*. 2004, 20: 2233-2248
- [71]. A.S. Khan, R. Kazmi, B. Farrokh, M. Zupan. Effect of oxygen content and microstructure on the thermo-mechanical response of three Ti–6Al–4V alloys: Experiments and modeling over a wide range of strain-rates and temperatures. *International Journal of Plasticity*. 2007, 23: 1105-1125
- [72]. J. Liu, A.S. Khan, L. Takacs, C.S. Meredith. Mechanical behavior of ultrafine-grained/nanocrystalline titanium synthesized by mechanical milling plus consolidation: Experiments, modeling and simulation. *International Journal of Plasticity*. 2015, 64: 151-163
- [73]. S. Mandal, B.T. Gockel, S. Balachandran, D. Banerjee, A.D. Rollett. Simulation of plastic deformation in Ti-5553 alloy using a self-consistent viscoplastic model. *International Journal of Plasticity*. 2017, 94: 57-73
- [74]. C.S. Meredith, A.S. Khan. Texture evolution and anisotropy in the thermo-mechanical response of UFG Ti processed via equal channel angular pressing. *International Journal of Plasticity*. 2012, 30: 202-217
- [75]. J.J. Sidor, K. Decroos, R.H. Petrov, L.A.I. Kestens. Evolution of recrystallization textures in particle containing Al alloys after various rolling reductions: experimental study and modeling. *International Journal of Plasticity*. 2015, 66: 119-137
- [76]. Z.C. Sun, H.L. Wu, J. Cao, Z.K. Yin. Modeling of continuous dynamic recrystallization of Al-Zn-Cu-Mg alloy during hot deformation based on the internal-state-variable (ISV) method. *International Journal of Plasticity*. 2018, 106: 73-87
- [77]. J. Wang, Z. Moumni, W. Zhang. A thermomechanically coupled finite-strain constitutive model for cyclic pseudoelasticity of polycrystalline shape memory alloys. *International Journal of Plasticity*. 2017, 97: 194-221

- 
- [78]. Y. Xiao, P. Zeng, L. Lei. Micromechanical modeling on thermomechanical coupling of cyclically deformed superelastic NiTi shape memory alloy. *International Journal of Plasticity*. 2018, 107: 164-188
- [79]. T. Furuhashi, B. Poorganji, H. Abe, T. Maki. Dynamic recovery and recrystallization in titanium alloys by hot deformation. *JOM*. 2007, 59: 64-67
- [80]. A. Rollett, G.S. Rohrer, J. Humphreys. Recrystallization and related annealing phenomena. 2017, third ed. Elsevier
- [81]. A.K. Kanjarla, P.V. Houtte, L. Delannay. Assessment of plastic heterogeneity in grain interaction models using crystal plasticity finite element method. *International Journal of Plasticity*. 2010, 26: 1220-1233
- [82]. H. Matsumoto, M. Kitamura, Y. Li, Y. Koizumi, A. Chiba. Hot forging characteristic of Ti-5Al-5V-5Mo-3Cr alloy with single metastable  $\beta$  microstructure. *Materials Science and Engineering: A*. 2014, 611: 337-344
- [83]. F. Warchomicka, M. Stockinger, H.P. Degischer. Quantitative analysis of the microstructure of near  $\beta$  titanium alloy during compression tests. *Journal of Materials Processing Technology* 2006, 177: 473-477
- [84]. C. M. Sellars, W. J. Tegart. On the mechanism of hot deformation. *Acta Metallurgica*. 1966, 14: 1136-1138
- [85]. F.J. Humphreys, M. Hatherly. Recrystallization and Related Annealing Phenomena. London: Elsevier Science Ltd, 2004, 11-35
- [86]. D.G. Cram, H.S. Zurob, Y.J. M. Brechet, C.R. Hutchinson. Modelling discontinuous dynamic recrystallization using a physically based model for nucleation. *Acta Materialia*. 2009, 57: 5218-5228
- [87]. S. Gourdet, F. Montheillet. A model of continuous dynamic recrystallization. *Acta Materialia*. 2003, 51: 2685-2699
- [88]. S. Gourdet, F. Montheillet. An experimental study of the recrystallization mechanism during hot deformation of aluminium. *Materials Science and Engineering: A*. 2000, 283: 274-288



- [89]. J.K. Fan, H.C. Kou, M.J. Lai, B. Tang, H. Chang, J.S. Li. Hot Deformation Mechanism and Microstructure Evolution of a New Near  $\beta$  Titanium Alloy. *Materials Science and Engineering: A*. 2013, 584: 121–132
- [90]. R. Prakash Kolli and Arun Bevaraj. A Review of Metastable Beta Titanium Alloys, *Metals*, 2018, 8: 506
- [91]. Philippart, H.J. Rack. High temperature dynamic yielding in metastable Ti–6.8Mo–4.5F–1.5Al. *Materials Science and Engineering: A*. 1998, 243: 196-200
- [92]. R. Srinivasan. Yield points during the high temperature deformation of Ti-15V-3Al-3Cr-3Sn alloy. *Scripta Metallurgica et Materialia* 1992, 27: 925-930
- [93]. L. Jing, R. Fu, Y. Wang, L. Qiu, B. Yan. Discontinuous yielding behavior and microstructure evolution during hot deformation of TC11 alloy. *Materials Science and Engineering: A*. 2017, 704: 434-439
- [94]. J.J. Jonas, C. Aranas, A. Fall, M. Jahazi. Transformation softening in three titanium alloys. *Materials & Design*. 2017, 113, 305–310
- [95]. J. Koike, Y. Shimoyama, I. Ohnuma, T. Okamura, R. Kainuma, K. Ishida, K. Maruyama. Stress-induced phase transformation during superplastic deformation in two-phase Ti–Al–Fe alloy, *Acta Materialia*. 2000, 48: 2059–2069
- [96]. M. Jackson, N.G. Jones, D. Dye, R.J. Dashwood. Effect of initial microstructure on plastic flow behaviour during isothermal forging of Ti–10V–2Fe–3Al. *Materials Science and Engineering: A*. 2009, 501: 248–254
- [97]. A. Carman, L.C. Zhang, O.M. Ivasishin, D.G. Savvakina, M.V. Matviychuk, E. V. Pereloma. Role of alloying elements in microstructure evolution and alloying elements behaviour during sintering of a near- $\beta$  titanium alloy. *Materials Science and Engineering A*. 2011, 528: 1686–1693
- [98]. M. Jackson, R.J. Dashwood, L. Christodoulou. The microstructural evolution of near beta alloy Ti–10V–2Fe–3Al during subtransus forging. *Metallurgical and Materials Transactions A*. 2005, 36: 1317–1327
- [99]. N.G. Jones, R.J. Dashwood, D. Dye, M. Jackson. Thermomechanical processing of Ti–5Al–5Mo–5V–3Cr. *Materials Science and Engineering: A*. 2008, 490: 369-377

- 
- [100]. N.G. Jones, R.J. Dashwood, D. Dye, M. Jackson. The flow behavior and microstructural evolution of Ti-5Al-5Mo-5V-3Cr during subtransus isothermal forging. *Metallurgical and Materials Transactions A*. 2009, 40: 1944-1954
- [101]. W.G. Johnston, J.J. Gilman. Dislocation velocities, dislocation densities, and plastic flow in lithium fluoride crystals. *Journal of Applied Physics*. 1959, 30: 129-144
- [102]. M.S. Pham, M. Iadicola, A. Creuziger, L. Hu, A.D. Rollett. Thermally-activated constitutive model including dislocation interactions, aging and recovery for strain path dependence of solid solution strengthened alloys: Application to AA5754-O. *International Journal of Plasticity*. 2015, 75: 226-243
- [103]. A.D. Rollett, G.S. Rohrer, R.M. Suter. Understanding materials microstructure and behavior at the mesoscale. *MRS Bulletin*. 2015, 40: 951-960
- [104]. T. Ozturk, A.D. Rollett. Effect of microstructure on the elasto-viscoplastic deformation of dual phase titanium structures. *Computational Mechanics*. 2018, 61: 55-70
- [105]. C. Poletti, L. Germain, F. Warchomicka, M. Dikovits, S. Mitsche. Unified description of the softening behavior of beta-metastable and alpha+ beta titanium alloys during hot deformation. *Materials Science and Engineering: A*. 2016, 651: 280-290
- [106]. I. Weiss, S.L. Semiatin. Thermomechanical processing of beta titanium alloys—an overview. *Materials Science and Engineering: A* 1998, 243: 46-65
- [107]. C. Randau, U. Garbe, H.-G. Brokmeier. StressTextureCalculator: a software tool to extract texture, strain and microstructure information from area-detector measurements, *Journal of Applied Crystallography*. 2011, 44: 641-646
- [108]. Beausir, B., Fundenberger, J.J., 2017. Analysis Tools for Electron and X-ray diffraction, ATEX software. <http://www.atex-software.eu>
- [109]. A. Morawiec, J.J. Fundenberger, E. Bouzy, J.S. Lecomte. EP — a program for determination of crystallite orientations from TEM Kikuchi and CBED diffraction patterns, *Journal of Applied Crystallography*. 2002, 35: 287-287
- [110]. H.J. Bunge, C. Esling, J. Muller. The role of the inversion centre in texture analysis. *Journal of Applied Crystallography*. 1980, 13: 544-554

- [111]. H.J. Bunge, C. Esling, J. Muller. The influence of crystal and sample symmetries on the orientation distribution function of the crystallites in polycrystalline materials, *Acta Crystallographica Section A*. 1981, 37: 889-899
- [112]. A.G. Khachaturyan. Theory of structural transformations in solids, John Wiley, New York, 1983
- [113]. Pearson's Handbook Desk Edition, Edited by P. Villars, ASM International, 1997
- [114]. S.K. Kara, A. Ghosha, N. Fulzelea, A. Bhattacharjee. Quantitative microstructural characterization of a near beta Ti alloy Ti-5553 under different processing conditions. *Materials Characterization*. 2013, 81: 37-48.
- [115]. A. Dehghan-Manshadi, R.J. Dippenaar. Development of  $\alpha$ -phase morphologies during low temperature isothermal heat treatment of a Ti-5Al-5Mo-5V-3Cr alloy. *Materials Science and Engineering: A*. 2011, 528: 1833-1839
- [116]. N. Gey, M. Humbert, M.J. Philippe, Y. Combres. Investigation of the  $\alpha$ - and  $\beta$ - texture evolution of hot rolled Ti-64 products. *Materials Science and Engineering: A*. 1996, 219: 80-88
- [117]. T. Inamura, M. Ii, M. Tahara, H. Hosoda. Formation process of the incompatible martensite microstructure in a beta-titanium shape memory alloy. *Acta Materialia*. 2017, 124: 351-359
- [118]. S. Balachandran, A. Kashiwar, A. Choudhury, D. Banerjee, R. Shi, Y. Wang. On variant distribution and coarsening behavior of the  $\alpha$  phase in a metastable  $\beta$  titanium alloy. *Acta Materialia*. 2016, 106: 374-387
- [119]. Y.D. Zhang, S.Y. Wang, C. Esling, J. Lecomte, C. Schuman, X. Zhao, L. Zuo. A method to identify dislocations in a known crystal structure by transmission electron microscopy. *Journal of Applied Crystallography*. 2011, 44: 1164-1168
- [120]. Y.M. Jin, G.J. Weng. A direct method for the crystallography of martensitic transformation and its application to TiNi and AuCd. *Acta Materialia*. 2002, 50: 2967-2987
- [121]. K.E.K. Amouzou, T. Richeton, A. Roth, M.A. Lebyodkin, T.A. Lebedkina. Micromechanical modeling of hardening mechanisms in commercially pure  $\alpha$ -titanium in tensile condition, *International Journal of Plasticity*. 2016, 80: 222-240

- 
- [122]. B. Barkia, V. Doquet, J.P. Couzinié, I. Guillot, E. Héripré. In situ monitoring of the deformation mechanisms in titanium with different oxygen contents. *Materials Science and Engineering: A*. 2015, 636: 91-102
- [123]. M.P. Echlin, J. C. Stinville, V. M. Miller, W. C. Lenthe, T. M. Pollock. Incipient slip and long range plastic strain localization in microtextured Ti-6Al-4V titanium. *Acta Materialia*. 2016, 114: 164-175
- [124]. A. Fitzner, D.G.L. Prakash, J.Q. Fonseca, M. Thomas, S.Y Zhang, J. Kelleher, P. Manuel, M. Preuss. The effect of aluminium on twinning in binary alpha-titanium. *Acta Materialia*. 2016, 103: 341-351
- [125]. M.J. Lai, T. Li, D. Raabe.  $\omega$  phase acts as a switch between dislocation channeling and joint twinning- and transformation-induced plasticity in a metastable  $\beta$  titanium alloy. *Acta Materialia*. 2018, 151: 67-77
- [126]. J. Zhang, C.C. Tasan, M.J. Lai, A.C. Dippel, D. Raabe. Complexion-mediated martensitic phase transformation in Titanium. *Nature Communication*. 2017, 8: 14210
- [127]. Y.F. Zheng , R.E.A. Williams, G.B. Viswanathan , W.A.T. Clark, H.L. Fraser. Determination of the structure of  $\alpha$ - $\beta$  interfaces in metastable  $\beta$ -Ti alloys, *Acta Materialia*. 2018, 150: 25-39
- [128]. T. Li, D. Kent, G. Sha, L.T. Stephenson, A.V. Ceguerra, S.P. Ringer, M.S. Dargusch, J.M. Cairney. New insights into the phase transformation to isothermal  $\omega$  and  $\omega$ -assisted  $\alpha$  in near  $\beta$ -Ti alloys. *Acta Materialia*. 2016, 106: 353-366
- [129]. J.R. Patel, M. Cohen. Criterion for the action of applied stress in the martensitic transformation. *Acta Metallurgica*. 1953, 1: 531-538
- [130]. D. De Knijf, T. Nguyen-Minh, R. Petrov, L.A.I. Kestens, J.J. Jonas. Orientation dependence of the martensite transformation in a quenched and partitioned steel subjected to uniaxial tension, *Journal of Applied Crystallography*. 2014, 47: 1261-1266
- [131]. S. Joseph, I. Bantounas, T.C. Lindley, D. Dye. Slip transfer and deformation structures resulting from the low cycle fatigue of near-alpha titanium alloy Ti-6242Si. *International Journal of Plasticity*. 2018, 100: 90-103

- [132]. Z. Zheng, S. Waheed, D.S. Balint, F.P.E. Dunne. Slip transfer across phase boundaries in dual phase titanium alloys and the effect on strain rate sensitivity. *International Journal of Plasticity*. 2018, 104: 23-38
- [133]. A. Rollett, G.S. Rohrer, J. Humphreys. Recrystallization and related annealing phenomena. third ed. Elsevier, 2017
- [134]. A. Morawiec. Orientations and Rotations. Berlin, Springer, 2003
- [135]. D. Gloaguen, G. Oum, V. Legrand, J. Fajoui, S. Branchu. Experimental and theoretical studies of intergranular strain in an alpha titanium alloy during plastic deformation. *Acta Materialia*. 2013, 61: 5779-5790
- [136]. R. Groger, V. Vitek. Stress dependence of the Peierls barrier of  $1/2\langle 111 \rangle$  screw dislocations in bcc metals. *Acta Materialia*. 2013, 61: 6362-6371
- [137]. N. Stefansson, S.L. Semiatin, D. Eylon. The kinetics of static globularization of Ti-6Al-4V. *Metallurgical and Materials Transactions A*. 2002, 33: 3527-3534
- [138]. G. Sharma, R.V. Ramanujan, G.P. Tiwari. Instability mechanisms in lamellar microstructures. *Acta Materialia*. 2000, 48: 875-889
- [139]. S.L. Semiatin, N. Stefansson, R.D. Doherty. Prediction of the kinetics of static globularization of Ti-6Al-4V. *Metallurgical and Materials Transactions A*, 2005, 36: 1372-1376
- [140]. S.L. Semiatin, D.U. Furrer. Modeling of microstructure evolution during the thermomechanical processing of titanium alloys. *ASM Handbook*, vol. 22. Fundamentals of Modeling for Metals Processing. Materials Park, OH: ASM International; 2009
- [141]. R.M. Miller, T.R. Bieler, S.L. Semiatin. Flow softening during hot working of Ti-6Al-4V with a lamellar colony microstructure. *Scripta Materialia*. 1999, 40: 1387-1393
- [142]. S. Suri, G.B. Viswanathan, T. Neeraj, D.H. Hou, M.J. Mills. Room temperature deformation and mechanisms of slip transmission in oriented single-colony crystals of an  $\alpha / \beta$  titanium alloy. *Acta Materialia*. 1999, 47: 1019-1034
- [143]. S. Mironov, M. Murzinova, S. Zharebtsov, G.A. Salishchev, S.L. Semiatin. Microstructure evolution during warm working of Ti-6Al-4V with a colony- $\alpha$  microstructure. *Acta Materialia*. 2009, 57: 2470-2481

- [144]. S.L. Semiatin, F. Montheillet, G. Shen, J.J. Jonas. Self-consistent modeling of the flow behavior of wrought alpha/beta titanium alloys under isothermal and nonisothermal hot-working conditions. *Metallurgical and Materials Transactions A*. 2002, 33: 2719-2727
- [145]. G.A. Sargent, A.P. Zane, P.N. Fagin, A.K. Ghosh, S.L. Semiatin. Low-temperature coarsening and plastic flow behavior of an alpha/beta titanium billet material with an ultrafine microstructure. *Metallurgical and Materials Transactions A*, 2008, 39: 2949

## Publication list

### I: Publications in international journals

- [1]. **Ke Hua**, Yudong Zhang, Weimin Gan, Hongchao Kou, Benoit Beausir, Jinshan Li, Claude Esling, Hot deformation behavior originated from dislocation activity and  $\beta$  to  $\alpha$  phase transformation in a metastable  $\beta$  titanium alloy. *International journal of Plasticity*, 2019, *In press*.
- [2]. **Ke Hua**, Yudong Zhang, Weimin Gan, Hongchao Kou, Jinshan Li, Claude Esling, Correlation between imposed deformation and transformation lattice strain on  $\alpha$  variant selection in a metastable  $\beta$ -Ti alloy under isothermal compression. *Acta Materialia*, 2018, 161: 150-160.
- [3]. **Ke Hua**, Yudong Zhang, Hongchao Kou, Jinshan Li, Weimin Gan, Jean-Jacques Fundenberger, Claude Esling, Composite structure of  $\alpha$  phase in metastable  $\beta$  Ti alloys induced by lattice strain during  $\beta$  to  $\alpha$  phase transformation. *Acta Materialia*, 2017, 132: 307-326.
- [4]. **Ke Hua**, Jinshan Li, Hongchao Kou, Jiangkun Fan, Miao Sun, Bin Tang, Phase precipitation behavior during isothermal deformation in  $\beta$ -quenched near beta titanium alloy Ti-7333. *Journal of Alloys & Compounds*, 2016, 671: 381-388.
- [5]. **Ke Hua**, Xiangyi Xue, Hongchao Kou, Jiangkun Fan, Bin Tang, Jinshan Li, Characterization of hot deformation microstructure of a near beta titanium alloy Ti-5553. *Journal of Alloys & Compounds*, 2014, 615: 531-537.

### II: Contributions to International Conferences

- [1]. **Ke Hua**, Yudong Zhang, Hongchao Kou, Jinshan Li, Weimin Gan, Jean-Jacques Fundenberger, Claude Esling, “Formation of microtexture induced by  $\beta$  to  $\alpha$  transformation in a metastable  $\beta$  Ti alloy”. 18th International Conference on Textures of Materials, November 5-10, 2017, St. George, Utah, USA, **Invited lecture**.

- [2]. **Ke Hua**, Yudong Zhang, Weimin Gan, Hongchao Kou, Jinshan Li, Claude Esling, “Deformation-induced  $\alpha$  variant selection during  $\beta$  to  $\alpha$  phase transformation in a metastable  $\beta$ -Ti alloy”. ESOMAT 2018: 11th European Symposium on Martensitic Transformations, August 27-31, 2018, Metz, Lorraine, France, **Poster**.
- [3]. **Ke Hua**, Yudong Zhang, Weimin Gan, Hongchao Kou, Benoit Beausir, Jinshan Li, Claude Esling, “Plastic deformation by dislocation slip and  $\beta$  to  $\alpha$  transformation in a metastable  $\beta$  titanium alloy under uniaxial isothermal compression”. Plasticity 2019: International Conference on Plasticity, Damage & Fracture, January 3-9, 2019, Panama City, Panama, **Oral**.



## **Acknowledgements**

I can't believe this day has finally come. The present work is accomplished at the Laboratoire d'Étude des Microstructures et de Mécanique des Matériaux (LEM3), Université de Lorraine, Metz, France, and the State Key Laboratory of solidification processing, Northwestern Polytechnical University, Xi'an, China. I have the honor to work at the two laboratories and I would like to give my heartfelt thank to the two institutions for hosting my study and to the staff in the two laboratories for their kind help.

I gratefully acknowledge the China Scholarship Council (CSC) for providing a PhD scholarship to support my study in France. This work was supported by the Major State Research Development Program of China under Grant Nos. 2016YFB0701303 and 2016YFB0701305, the Program de Recherche Conjoint CNRS-NSFC under the Grant No. PRC1475, and the National Natural Science Foundation of China under Grant Nos. 51371143 and 51711530151. Parts of the present work is based upon experiments performed at the STRESS-SPEC instrument operated by HZG and FRM II at the Heinz Maier-Leibnitz Zentrum (MLZ), Garching, Germany. I gratefully acknowledge all these institutions for their financial support.

I would like to sincerely thank the reviewers and the jury members of this dissertation for taking time out of their busy schedules to achieve my dissertation defense, and special gratitude to Professor Anthony ROLLETT, Professor Benoit APPOLAIRE, Professor Rui YANG, Professor Yongqing ZHAO, Professor Elisabeth GAUTIER and Professor Claude Esling for their evaluation of my dissertation and for the constructive suggestions and comments.

Then I would like to express my deepest and sincere gratitude to my advisors, Dr. HDR. Yudong Zhang, Université de Lorraine, in France, Prof. Jinshan Li, in China, Dr. HDR. Weimin Gan, at MLZ, in Germany, and Prof. Hongchao Kou, in China. They not only provide the guidance and support to my PhD work but also the constant and selfless help in my daily life. Thanks for their incredible patience and constant supports that allow me to survive after a long incubation time in my learning curve in this field.

I am also grateful to all the staffs and students in the two laboratories and my friends

who shared their experiences with me and offered help to my study, especially to Guang YANG, Xiajiang HOU, Liang CHENG, Yinben HAN, Haile YAN, Cai CHEN, Yajun ZHAO, Jiangkun FAN, Naifu ZOU, Shun XU, Chunyang ZHANG, Ruifeng DONG, Bin ZHU, Hailong SHI, Xiaorui LIU, Chunqing LIN, Xiaomeng LIU, Meishuai LIU, Jing WEN, Fengming QIANG and Qian WANG. Special thanks to my young friend Pengru ZHAO for her endless help in my daily life.

A special gratitude and love go to my family for their endless support. I deeply appreciate my parent's incredible patience and constant support throughout my Ph.D. study. I will never truly be able to express my sincere appreciation to the both of you. Without the great help from my parents during their stay with me, I would have not been able to start my PhD work. Last but not least, I would like to express my deep love and gratitude to my lovely girlfriend, Ms. Yu LEI, who has always been loving, helping, encouraging and supporting me in my life, especially during the most difficult time of PhD work time.